

Turkish Journal of
**Analytical
Chemistry**

Volume 7
Issue 1
January 2025

<https://dergipark.org.tr/tr/pub/turkjac>

Turkish Journal of
**Analytical
Chemistry**
TurkJAC

Volume 7
Issue 1
January 2025

Publication Type: Peer-reviewed scientific journal
Publication Date: January 31, 2025
Publication Language: English
Published three times a year (January, May, September)

Owner

Prof. Miraç Ocak

Karadeniz Technical University, Faculty of Sciences, Department of Chemistry

Executive Editor

Prof. Ümmühan Ocak

Karadeniz Technical University, Faculty of Sciences, Department of Chemistry

Co-Editor

Ender Çekirge

Karadeniz Technical University, Institute of Forensic Sciences

Layout Editor

Ender Çekirge

Karadeniz Technical University, Institute of Forensic Sciences

Editorial Secretary

Ender Çekirge

Karadeniz Technical University, Institute of Forensic Sciences

Language Editors

Nurhayat Özbek

Karadeniz Technical University, Faculty of Sciences, Department of Chemistry

Prof. Miraç Ocak

Karadeniz Technical University, Faculty of Sciences, Department of Chemistry

Aslıhan Yılmaz Çamoğlu

Karadeniz Technical University, Faculty of Sciences, Department of Chemistry

Copyeditor

Nurhayat Özbek

Karadeniz Technical University, Faculty of Sciences, Department of Chemistry

Aslıhan Yılmaz Çamoğlu

Karadeniz Technical University, Faculty of Sciences, Department of Chemistry

Prof. Miraç Ocak

Karadeniz Technical University, Faculty of Sciences, Department of Chemistry

Proofreader

Nurhayat Özbek

Karadeniz Technical University, Faculty of Sciences, Department of Chemistry

Aslıhan Yılmaz Çamoğlu

Karadeniz Technical University, Faculty of Sciences, Department of Chemistry

Editors

Prof. Ümmühan Ocak

Karadeniz Technical University, Faculty of Sciences, Department of Chemistry

Prof. Miraç Ocak

Karadeniz Technical University, Faculty of Sciences, Department of Chemistry

Prof. Ali Gündoğdu

Karadeniz Technical University, Maçka Vocational School, Department of Pharmacy Services

Section Editors

Prof. Ali Gündoğdu

Karadeniz Technical University, Maçka Vocational School, Department of Pharmacy Services

Editor Board

Prof. Selehattin Yılmaz

Çanakkale Onsekiz Mart University, Faculty of Science and Literature, Department of Chemistry

Prof. Ali Gündoğdu

Karadeniz Technical University, Maçka Vocational School, Department of Pharmacy Services

Prof. Hakan Alp

Karadeniz Technical University, Faculty of Sciences, Department of Chemistry

Prof. Volkan Numan Bulut

Karadeniz Technical University, Maçka Vocational School, Department of Chemistry and Chemical Processing Technologies

Prof. Celal Duran

Karadeniz Technical University, Faculty of Sciences, Department of Chemistry

Asst. Prof. Aysel Başoğlu

Gümüşhane University, Faculty of Health Sciences, Department of Occupational Health and Safety

Prof. Ayşegül İyidoğan

Gaziantep University, Faculty of Science and Literature, Department of Chemistry

Prof. Sevgi Kolaylı

Karadeniz Technical University, Faculty of Sciences, Department of Chemistry

Prof. Hüseyin Serencam

Trabzon University, College of Applied Sciences, Department of Gastronomy and culinary arts

Assoc. Prof. Fatma Ağin

Karadeniz Technical University, Faculty of Pharmacy, Department of Basic Pharmaceutical Sciences

Prof. Duygu Özdeş

Gümüşhane University, Gümüşhane Vocational School, Department of Chemistry and Chemical Processing Technologies

Dr. Mustafa Z. Özel

University of York, Department of Chemistry

Prof. Małgorzata Wiśniewska

University of Maria Curie- Sklodowska, Faculty of Chemistry, Institute of Chemical Sciences, Department of Radiochemistry and Environmental Chemistry

Prof. Dilek Kul

Karadeniz Technical University, Faculty of Pharmacy, Department of Basic Pharmaceutical Sciences

Prof. Sławomira Skrzypek

University of Lodz, Faculty of Chemistry, Department of Inorganic and Analytical Chemistry

Prof. Fatih İslamoğlu	Recep Tayyip Erdoğan University, Faculty of Science and Literature, Department of Chemistry
Asst. Prof. Zekeriyya Bahadır	Giresun University, Faculty of Science and Literature, Department of Chemistry
Asst. Prof. Yasemin Çağlar	Giresun University, Faculty of Engineering, Department of Genetic and Bioengineering
Prof. Agnieszka Nosal-Wiercińska	University of Maria Curie- Sklodowska, Faculty of Chemistry, Institute of Chemical Sciences, Department of Analytical Chemistry
Assoc. Prof. Dr. Halit Arslan	Gazi University, Faculty of Science, Department of Chemistry
Assoc. Prof. Cemalettin Baltacı	Gümüşhane University, Faculty of Engineering and Natural Sciences, Department of Food Engineering
Asst. Prof. Zafer Ocak	Kafkas University, Education Faculty, Mathematics and Science Education
Prof. Mustafa İmamoğlu	Sakarya Univer.sity, Faculty of Science and Literature, Department of Chemistry
Assoc. Prof. Esra Bağda	Sivas Cumhuriyet University, Faculty of Pharmacy, Department of Basic Pharmaceutical Sciences, Analytical Chemistry Division
Assoc. Prof. Hüseyin Altundağ	Sakarya University, Faculty of Science and Literature, Department of Chemistry
Asst. Prof. Mehmet Başoğlu	Gümüşhane University, Faculty of Engineering and Natural Sciences, Department of Energy Systems Engineering

Publishing Board

Prof. Latif Elçi	Pamukkale University, Faculty of Science and Literature, Department of Chemistry
Prof. Münevver Sökmen	Konya Food and Agriculture University, Faculty of Engineering and Architecture, Department of Bioengineering
Prof. Atalay Sökmen	Konya Food and Agriculture University, Faculty of Engineering and Architecture, Department of Bioengineering
Prof. Kamil Kaygusuz	Karadeniz Technical University, Faculty of Sciences, Department of Chemistry
Prof. Yaşar Gök	Pamukkale University, Faculty of Science and Literature, Department of Chemistry
Prof. Ayşegül Gölcü	İstanbul Technical University, Faculty of Science and Literature, Department of Chemistry
Prof. Mustafa Tüzen	Gaziosmanpaşa University, Faculty of Science and Literature, Department of Chemistry
Prof. Mustafa Soylak	Erciyes University, Faculty of Sciences, Department of Chemistry
Prof. Fikret Karadeniz	Kafkas University, Faculty of Science and Literature, Department of Chemistry

Prof. Mehmet Yaman	Fırat University, Faculty of Sciences, Department of Chemistry
Prof. Halit Kantekin	Karadeniz Technical University, Faculty of Sciences, Department of Chemistry
Prof. Esin Canel	Ankara University, Faculty of Sciences, Department of Chemistry
Prof. Dilek Ak	Anadolu University, Faculty of Pharmacy, Department of Basic Pharmaceutical Sciences
Prof. Mustafa Küçükislamoğlu	Sakarya University, Faculty of Science and Literature, Department of Chemistry
Prof. Salih Zeki Yıldız	Sakarya University, Faculty of Science and Literature, Department of Chemistry
Prof. Recai İnam	Gazi University, Faculty of Sciences, Department of Chemistry
Prof. Dr. Durişehvar Ünal	İstanbul University, Faculty of Pharmacy, Department of Basic Pharmaceutical Sciences
Prof. Mehmet Tüfekçi	Avrasya University, Faculty of Science and Literature, Department of Biochemistry
Prof. Hüseyin Kara	Selçuk University, Faculty of Sciences, Department of Chemistry
Prof. Sezgin Bakirdere	Yıldız Technical University, Faculty of Science and Literature, Department of Chemistry
Prof. Hasan Basri Şentürk	Karadeniz Technical University, Faculty of Sciences, Department of Chemistry
Prof. Yusuf Atalay	Sakarya University, Faculty of Science and Literature, Department of Physics
Prof. Salih Zeki Yıldız	Sakarya University, Faculty of Science and Literature, Department of Chemistry

Authorship, Originality, and Plagiarism: The authors accept that the work is completely original and that the works of others have been appropriately cited or quoted in the text with the necessary permissions. The authors should avoid plagiarism. It is recommended that they check the article using appropriate software such as Ithenticate and CrossCheck. The responsibility for this matter rests entirely with the authors. All authors will be notified when the manuscript is submitted. If a change of author is needed, the reason for the change should be indicated. Once the manuscript is accepted, no author changes can be made.

Aims and Scope

“Turkish Journal of Analytical Chemistry” publishes original full-text research articles and reviews covering a variety of topics in analytical chemistry. Original research articles may be improved versions of known analytical methods. However, studies involving new and innovative methods are preferred. Topics covered include:

- Analytical materials
- Atomic methods
- Biochemical methods
- Chromatographic methods
- Electrochemical methods
- Environmental analysis
- Food analysis
- Forensic analysis
- Optical methods
- Pharmaceutical analysis
- Plant analysis
- Theoretical calculations
- Nanostructures for analytical purposes
- Chemometric methods
- Energy

ETHICAL GUIDELINES

TurkJAC follows ethical tasks and responsibilities are defined by the Committee on Publication Ethics (COPE) in publication procedure. Based on this guide, the rules regarding publication ethics are presented in the following sections.

Ethical Approval

Ethics committee approval must be obtained for studies on clinical and experimental regarding human and animals that require an ethical committee decision, this approval must be stated in the article and documented in the submission. In such articles, the statement that research and publication ethics are complied with should include. Information about the approval such as committee name, date, and number should be included in the method section and also on the first/last page of the article.

Editors

1. In the preliminary evaluation of a submission, the editor of the journal evaluates the article's suitability for the purpose and scope of the journal, whether it is similar to other articles in the literature, and whether it meets the expectations regarding the language of writing. When it meets the mentioned criteria, the scientific evaluation process is started by assigning a section editor if necessary.
2. A peer-reviewed publication policy is employed in all original studies, taking into full account of possible problems due to related or conflicting interests.

3. Section editors work on the articles with a specific subject and their suggestion is effective in the journal editor's decision about acceptance or rejection of the article.
4. No section editor contacts anyone except the authors, reviewers, and the journal editor about articles in the continued evaluation process.
5. In the journal editor's decision to accept or reject an article, in the addition of section editor's suggestion in consequence of scientific reviewing, the importance of the article, clarity and originality are decisive. The final decision, in this case, belongs to the journal editor.

Authors

1. The authors should actively contribute to the design and execution of the work. Authorship should not be given to a person who does not have at least one specific task in the study.
2. Normally all authors are responsible for the content of the article. However, in interdisciplinary studies with many authors, the part that each author is responsible for should be explained in the cover letter.
3. Before the start of the study, it would be better to determine the authors, contributors, and who will be acknowledged in order to avoid conflict in academic credits.
4. The corresponding author is one of the authors of the article submitted to the journal for publication. All communications will be conducted with this person until the publication of the article. The copyright form will be signed by the corresponding author on all the authors' behalf.
5. It is unacceptable to submit an article that has already been published entirely or partly in other publication media. In such situation, the responsibility lies with all authors. It is also unacceptable that the same article has been sent to TurkJAC and another journal simultaneously for publication. Authors should pay attention to this situation in terms of publication ethics.
6. Plagiarism from others' publications or their own publications and slicing of the same study is not acceptable.
7. All authors agree that the data presented in the article are real and original. In case of an error in the data presented, the authors have to be involved in the withdraw and correction process.
8. All authors must contribute to the peer-reviewed procedure.

Reviewers

1. Peer reviewers worked voluntarily are external experts assigned by editors to improve the submitted article.
2. It is extremely important that the referee performs the review on time so that the process does not prolong. Therefore, when the invitation is agreed upon, the reviewer is expected to do this on time. Also, the reviewer agrees that there are no conflicts of interest regarding the research, the authors, and/or the research funders.
3. Reviewers are expected not to share the articles reviewed with other people. The review process should be done securely.
4. Reviewers are scored according to criteria such as responding to the invitations, whether their evaluations are comprehensive and acting in accordance with deadlines, and the article submissions that they can make to TurkJAC are handled with priority.

Turkish Journal of Analytical Chemistry

2025

Volume: 7

Issue: 1

Contents

Research Articles

- Investigation of antioxidant and anticholinesterase activity of *Hypericum Perforatum* L. extracts 1–8

Demet Dincel*, Yasin Dari, Cagla Kizilarslan Hancer, Nur B. Onal, Murat Kartal, Gulacti Topcu

- Sensory and physicochemical characteristics of mulberry leathers enriched with sesame, almond, sunflower seeds, coconut, and peanut 9–21

Burak Güler, Cemalettin Baltacı*, Murat Küçük, Huri İlyasoğlu, Turgut Şahinöz, Omer Karpuz, Fırat Yılmaz, Kağan Kılınç

- Highly efficient hexavalent chromium removal using *nano*-Fe₃O₄/pomegranate peel biochar/alginate composite as an advanced biosorbent** 22–32

Şerife Parlayıcı, Erol Pehlivan*

- Catalytic co-pyrolysis of PET/PP plastics and olive pomace biomass with marble sludge catalyst** 33–45

Esra Yel*, Merve Kalem, Gamze Goktepe, Afra Kurt, Gulnare Ahmetli, Vildan Onen

- Determination of heavy metals and pesticide residue in soil, plant and water using QuEChERS method and design of experiment along Asa-River Tributary 46–54

S. W. Olokoba*

- Characterisation of a new mesoporous active nanocarbon obtained by hazelnut shell charcoal 55–60

Hakan Akgün*, Birsen Şengül Oksal, Adile Bektaş, Hakan Bektaş

Reviews

- Theoretical and applied potential of artificial intelligence and machine learning in analysing molecular data 61–70

Fatih Mehmet Avcu*

*Author of correspondence:

** [The paper was presented at the 6th International Environmental Chemistry Congress, EnviroChem 05-08 November 2024, Trabzon Türkiye.](#)



Investigation of antioxidant and anticholinesterase activity of *Hypericum Perforatum* L. extracts

Demet Dincel^{1*} , Yasin Darı^{1,2} , Cagla Kizilarslan Hancer³ , Nur B. Onal¹ , Murat Kartal⁴ , Gulacti Topcu⁴ 

¹ Bezmialem Vakıf University, Faculty of Pharmacy, Department of Analytical Chemistry, 34093, İstanbul, Türkiye

² Graduate School of Anadolu University, Department of Analytical Chemistry, 26470, Eskişehir, Türkiye

³ Bezmialem Vakıf University, Faculty of Pharmacy, Department of Pharmaceutical Botany, 34093, İstanbul, Türkiye

⁴ Bezmialem Vakıf University, Faculty of Pharmacy, Department of Pharmacognosy, 34093, İstanbul, Türkiye

Abstract

Hypericum perforatum L. is widely known for its therapeutic properties, including wound healing, antispasmodic effects, and anxiety treatment. This study was examined the total phenolic and flavonoid content, antioxidant capacity, and anticholinesterase activity of aqueous, ethanolic, and water-ethanol extracts from the plant's aerial parts and also green chemistry and sustainability were also investigated. Extraction was performed under reflux at 60°C. The anticholinesterase effect of *Hypericum perforatum* L., which is known to be used in the treatment of neurological diseases such as coxalgia, paralysis, spastic paralysis, menopausal neurosis, spinal convulsion etc., was investigated *in vitro*. Three different extracts were prepared as 100% ethanol, 50% ethanol-50% water and 100% water. The antioxidant activity of the prepared extracts was examined using Folin-Ciocalteu in terms of total phenolic-flavonoid content and then the anticholinesterase activity of extracts was investigated by Ellman method. LC-HR-MS identified Rhamnocitrin as the most abundant compound in the water-ethanol extract, while Quercitrin and Hederagenin were descent in the ethanol extract. The ethanol extract demonstrated the highest total flavonoid content and enzyme inhibition rates, especially for AChE (65%) and BChE (75%). In contrast, the water extract had the highest phenolic content but lower enzyme inhibition, especially for BChE (16%). Greenness metrics analysis demonstrated superior recyclability for the aqueous extract, earning it the highest score in sustainability. In general, the ethanol extract exhibited the most potent biological activity, while the aqueous extract excelled in green chemistry principles. These findings support the potential of *H. perforatum* extracts for further development in natural product research.

Keywords: Chlorine dioxide, catalysts, oxidation agent, aromatic aldehydes, aromatic acids

1. Introduction

Hypericum perforatum L. (commonly known as St. John's Wort) is a species in the genus *Hypericum* and family Hypericaceae, which includes 400 species worldwide [1]. *H. perforatum* is a plant native to Europe, North Africa, and Western Asia; however, due to its cultivation as a medicinal or ornamental plant, it is now prevalent in temperate regions such as Australia, India, New Zealand, South Africa, and South America [2]. *H. perforatum*, which grows abundantly and wild throughout most of Türkiye, is known by various names in our country, including "Sarı Kantaron, Binbir Delik Otu, Yara Otu, Kanotu, Mayasıl otu, Kuzukıran" [3]. In Türkiye, there are 119 taxa, 49 of which are endemic [4]. Consumption of *H. perforatum* derived products has risen sharply, making it one of the most widely used medicinal plants worldwide [5]. Its medicinal uses

include treating skin wounds, eczema, burns, digestive issues, and psychological disorders [6]. The plant's aboveground parts, branches, leaves, flowers, fruits, and seeds are used internally as an appetite, stimulant, sedative, antispasmodic, and deworming agent. It is also used to treat diarrhea, stomach ulcers, abdominal pain, urinary tract infections, prostate issues, colds, and coughs, and as an expectorant. Externally, it is reported to be used for treating wounds, burns, oral infections, and mouth sores [7]. The aboveground parts of *Hypericum perforatum* possess antidepressant properties due to hypericin; sedative, anti-inflammatory, and analgesic effects due to biflavonoids and hyperforin; and diuretic and astringent actions attributed to flavonoids and tannins. Its volatile oil has antiphlogistic properties. Internally, it is used for treating moderate depression,

Citation: D. Dincel, Y. Darı, C.K. Hancer, N.B. Onal, M. Kartal, G. Topcu, Investigation of antioxidant and anticholinesterase activity of *Hypericum Perforatum* L. extracts, Turk J Anal Chem, 7(1), 2025, 1–8.

***Author of correspondence:** ddincel@bezmialem.edu.tr

Tel: +90 (264) 295 61 36

Fax: +90 0 (264) 295 59 50

Received: October 13, 2024

Accepted: December 18, 2024

doi <https://doi.org/10.51435/turkjac.1565559>

anxiety, and nervous disorders, particularly menopause-related anxiety and stress relief. Externally, extracts prepared with herbal oils are applied in the treatment of wounds, burns, and minor cuts [8].

In the aerial parts of the plant, there are 0.05-0.3% naphthodianthrone derivatives (hypericin, pseudohypericin, isohypericin), 2.5% flavonoids (hyperoside, rutin, quercitrin, isoquercitrin, quercetin, kaempferol), about 0.26% biflavonoids (biapigenin), 2-4.5% phloroglucinols (hyperforin, adhyperforin), 0.05-0.3% volatile oils (*n*-alkanes, monoterpenes), 6.5-15% catechin and condensed tannins (catechin, epicatechin, leucocyanidin), phenolic acids (caffeic, chlorogenic, ferulic), β -sitosterol, xanthones (1,3,6,7-tetrahydroxyxanthone), phenylpropanoids, and vitamins A and C [9].

Numerous studies have highlighted the therapeutic potential of *H. perforatum* due to its diverse biological activities. Research has shown that extracts of *H. perforatum* possess significant antioxidant properties, which can decrease oxidative stress and reduce cellular damage [10]. Furthermore, the anticholinesterase activity of *H. perforatum* has been extensively documented, indicating its potential in treating neurodegenerative diseases such as Alzheimer's. A study by [11] revealed that specific extracts inhibited acetylcholinesterase activity, thereby enhancing cholinergic neurotransmission. Additionally, *H. perforatum* exhibits antimicrobial properties, as evidenced by [12], who reported its effectiveness against various pathogens, including bacteria and fungi. Furthermore, this plant is renowned for its wide range of biological activities, including antitumor [13], cytotoxic [14], anticancer [15], antiproliferative [16], anti-inflammatory [17], leishmanicidal activity [18], antibacterial [19], neuroprotective activity [20], antifungal [21] features. These findings collectively underscore the significance of *H. perforatum* in traditional and modern medicine, emphasizing its role as a natural source of bioactive compounds with multiple health benefits.

In this study, we introduced a novel extraction method for *H. perforatum*, emphasizing its significance as the first documented approach in the literature. Our method involved water bath extraction at 60°C using three different solvents: ethanol, water, and a (1:1) mixture of ethanol and water. This innovative approach allowed for a comprehensive assessment of the extracts, as we performed LC-HR/MS (Liquid Chromatography-High Resolution Mass Spectrometry) analysis to quantify phenolic content. Additionally, we evaluated the total phenolic and total flavonoid content, along with the anticholinesterase activity in these extracts. While previous studies have typically utilized methanol, ethyl

acetate, or water extraction via maceration and focused primarily on antioxidant activities [12] or anticholinesterase effects [11], our research uniquely combines temperature-controlled extraction with varied solvent ratios. This not only enhances the extraction efficiency but also presents a more holistic view of the antioxidant and anticholinesterase activities of *H. perforatum*. The importance of green chemistry is increasing day by day. Based on this, we also worked on green chemistry and sustainability for extraction methods via AGREE: Analytical Greenness Calculator software. There are 12 metrics related to "green chemistry principles". Based on minimize waste, analyst safety, energy consumption, renewable material etc., it gives a score between 0 to 1. We used AGREE for calculating different type of solvents in this extraction techniques. It gave a chance to compare these three different solvents in this extraction technique.

2. Experimental

2.1. Chemicals and reagents

The chemicals used in the experiment and their sources of supply are listed below:

Quercetin (Merck, Germany), pirocatechol (Merck, Germany), DTNB (5,5-dithiobis-(2-nitrobenzoic acid)) (Merck, Germany), acetylcholinesterase (Merck, Germany), butyrylcholinesterase (Merck, Germany), chloroform (Merck, Germany), dichlorometane (Merck, Germany), methanol (Merck, Germany), ethanol (Merck, Germany), aluminum nitrate (Merck, Germany), potassium acetate (Merck, Germany), galantamine hydrobromide (Sigma Aldrich, Germany), acetylthiocholine iodide (Sigma Aldrich, Germany), Folin-Ciocalteu reagent (Merck, Applichem, Germany), butyrylthiocholine iodide (Merck, Fluka, Germany), sodium carbonate (Merck, Germany), ammonium acetate (Merck, Germany), sodium hydrogen phosphate (Merck, Germany), sodium dihydrogen phosphate (Merck, Germany)

2.2. Instrumentations and analytical conditions

The Thermo LC system consisted of a Thermo Orbitrap Q-Exactive HRMS equipped with electrospray ion (ESI) source were used for the analysis (Thermo, USA). Data acquisition were performed on TRACE FINDER software. The chromatographic separations was performed on C18 (3 μ m*150mm*3.00 mm; Fortis) analytical column. The mobile phases were prepared including %0.1 formic acid water (A) and methanol (B). The flow rate for the analysis was determined as 0.35 mL/min and the elution gradient given in the Table 1 was used.

Table 1. Gradient elution

Gradient Time (min)	Flow rate (mL/min)	% B (mobile phase)
0.00	0.35	50
1.00	0.35	50
3.00	0.35	100
6.00	0.35	100
7.00	0.35	50
10.00	0.35	50

The compounds of each extract were ionized with the help of ESI in positive and negative mode. MS parameters were set as; sheath gas flow rate 45 L/min, auxiliary gas flow rate 10 L/min, spray voltage 3.8 kV, capillary temperature 320 °C, and auxiliary gas heater temperature 320 °C [22,23].

2.3. Plant material

H. perforatum was collected from Irvindi-Balıkesir in June 2020 and identified by Cagla Kızılarıslan Hancer. It was stored in the herbarium of the Faculty of Pharmacy of Istanbul University (ISTE no: 117.295).

2.4. Extraction method

The herba of *H. perforatum* L. of 1 kg of dried plant was turned into powder in a blender. It was divided into three equal parts, each weighing approximately 250 g. Three separates extracts were prepared: ethanol, water, and water:ethanol (50:50; v/v) using water bath extraction at 60°C.

2.4.1. Preparation of ethanol extracts (HE):

250 g of plant was placed in a volumetric flask. 500 mL of ethanol was added. Extracted under reflux into volumetric flasks for two hours (Fig. 1). After that, it was cooled to room temperature and filtered by filter paper. The remaining ethanol was evaporated by rotary evaporator. Plant extract was stored -80°C until the analysis.

2.4.2. Preparation of water extracts (HS):

Approximately 245 g of plant was placed in volumetric flask and 600 mL of water was added. Extracted under reflux for three hours. It was cooled to room temperature and filtered via filter paper. Then, the extract was divided into four equal parts again and 700 mL of water was added. After waiting in the water bath for two hours, it was removed from the water by aid of rotary evaporator. Plant extracts were stored -80°C until the analysis.

2.4.3. Preparation of water:ethanol extracts (HSE):

250 g of plants weighed and 600 mL of mixture of ethanol:water (50:50; v/v) was added. The extract was kept under reflux for two hours and allowed to cool. When it reached room temperature, it was filtered with the help of filter paper. The remaining solvent was removed by rotary evaporator. It was stored -80°C until the analysis.



Figure 1. Water bath extraction at 60°C

2.5. Investigation of total phenolic content

The Folin-Ciocalteu method, which is commonly used for the determination of total phenolic compounds, is based on the absorbance measurement according to the color intensity formed by the Folin-Ciocalteu reagent, which gives its name to the method. Pyrocatechol (o-Benzenediol) was used as the standard phenolic compound. As a result of the analysis, a high absorbance value is an indicator of a high amount of phenolic substance [24]. The total phenolic content of the all extracts was determined using the Folin-Ciocalteu reagent as equivalent to pyrocatechol [25]. Pyrocatechol stock solution was prepared at a concentration of 100 ppm. 0,1,2,3,4,5,6,7, and 8 µL of the stock solution were taken, respectively, and their volumes were completed to 184 µL with distilled water. Solutions were prepared from samples taken from aqueous, aqueous:ethanol (50:50; v/v) and ethanolic extracts obtained from the *Hypericum perforatum* L. at a concentration of 1000 ppm. 4 µL of sample solutions including 1 mg of extract were taken and completed to 184 µL with distilled water. 4 µL of FCR reagent was added to the pyrocatechol solutions and samples, and after waiting for 3 min, 12 µL of 2% Na₂CO₃ solution was added. The mixture was left at room temperature for 2 hours and the absorbance values of the samples were measured at 760 nm. Total phenolic contents of the extracts were determined using the following equation obtained from the calibration curve of standard pyrocatechol (Eq 1.). All the samples were measured triplicates.

$$\text{Absorbance} = 0.0286 (\mu\text{g}) - 0.0733 \quad (1)$$

$$(R^2 = 0.9953)$$

2.6. Investigation of total flavonoid content

Flavonoids are phenolic compounds with a diphenylpropane structure, which consist of two phenyl

rings combined with a propane chain. Quercetin was used as the standard flavonoid compound.

Total flavonoid contents of the obtained extracts were determined as quercetin equivalents by the aluminum nitrate method [26]. Stock solution of quercetin was prepared at a concentration of 100 ppm. 0,1,2,3,4,5,6,7, and 8 μ L were taken from the stock solution and the volumes of each were completed to 192 μ L with 80% ethanol by volume. 4 μ L of 1 M potassium acetate was added and waiting for 1 min. Then, 4 μ L of 10% aluminum nitrate was added. After incubation for 40 minutes, absorbance were measured at 415 nm. Solutions were prepared from samples taken from all extracts of *Hypericum perforatum* L. at a concentration of 1000 ppm. The absorbance of 1000 ppm solutions taken from each extract were measured at 415 nm. Total flavonoid contents of the extracts were determined using the following equation obtained from the calibration curve of standard quercetin (Eq 2.). All the samples were measured triplicates.

$$\text{Absorbance} = 0.0394 (\mu\text{g}) - 0.0471 \quad (2)$$

$$(R^2 = 0.9959)$$

2.7. Activity of anti-cholinesterase

The Ellman method, also known as a spectrophotometric method, is a method used to measure the inhibitory activities of acetylcholinesterase and butyrylcholinesterase enzymes for the determination of anticholinesterase activity [27]. The principle of this method is based on the *in vitro* hydrolysis of acetylcholine by acetylcholinesterase or butyrylcholinesterase to be followed [28]. This method, a colorimetric method in which acetylcholine is cleaved to thiocholine by AChE and then reacts with 5,5'-dithiobis-(2-nitrobenzoic acid) (DTNB) to give the yellow 5-thio-2-nitrobenzoate anion, was performed in 96-well microplates.

Ellman Method

Acetylcholinesterase obtained from electric fish and butyrylcholinesterase obtained from horse serum were used as enzymes, and acetylcholine iodide and butyrylcholine iodide were used as substrates in Ellman method. DTNB, which is yellow in color, was used to measure the inhibitory activity of acetylcholinesterase and butyrylcholinesterase enzymes. 130 μ L of phosphate buffer with pH:8 was added to each well of 96-well microplates, 10 μ L of the solutions of extracts prepared at a concentration of 4000 ppm in ethanol, and 20 μ L of BChE solution was added to the AChE and other samples in microplates. It was incubated at 25°C for 10 minutes. Then, 20 μ L of DTNB solution and 20 μ L of acetylcholine iodide and/or butyrylcholine iodide as substrate were added. The 5-thio-2-nitrobenzoic acid

anion, which was formed as a result of the reaction of thiocholine with DTNB, which was released by the enzymatic hydrolysis of acetylcholine iodide and butyrylcholine iodide on the other microplate samples, respectively, was examined spectrophotometrically at 412 nm. Ethanol was used as a control and galantamine was used as standard. AChE and BChE activity (% inhibition) was calculated using the following equation (Eq.3). All the samples were measured triplicates.

$$\% \text{ Inhibition} = \frac{(\text{Control} - \text{Sample})}{\text{Control}} \times 100 \quad (3)$$

2.8. Assessment of the greenness

With technological developments, new studies carried out in the chemical and pharmaceutical sectors, reducing the scale, and thus minimizing the damage to the environment has become an important criterion. In recent years, researchers have been working to prevent environmental pollution and develop eco-friendly analytical methods. The newly developed 'eco-friendly' analytical methods aim to keep the amount of solvent and other chemicals consumed at a minimum level to minimize the irritating, toxic, corrosive and pollution effects of them. In addition, reducing the energy consume in analyses is possible by reducing the number of process steps for analysis. One of the points that the 'green chemistry' principle attaches importance to is automation. As the method of working with the automation system increases, the analyst's safety will increase, and his/her effort will decrease. In summary, green chemistry principles prioritize the required automation system, using recyclable materials, minimization of polluting solvents, other chemicals and waste, reduction of energy consumption, and analyst safety.

There are some analytical green calculation (greenness) programs prepared by considering the principles of green chemistry. Wojnowski et al. developed the software AGREE: Analytical Greenness Calculator to assess the environmental and occupational hazards associated with a given analytical procedure based on 12 principles [29]. The score obtained from these metrics is converted into a graph showing extent to which each of the 12 principles is complied with this program. The score between 0 to 1 obtained from each principle visually represents the extent to which the green chemistry principle is complied with in which steps with the colors green, yellow and red [30].

2.9. Statistical calculations

The activity results are demonstrated as the mean \pm standard deviation from three independent tests. The

results were found to be within the 95% confidence interval relied on the Student's t-test. Measurement curves were plotted between absorbance and concentration, and the corresponding regression equations were determined. Linear regression analysis, based on the least squares method, was carried out by evaluating the slope, intercept, and correlation coefficients.

3. Results and discussion

3.1. Results of total phenolic and total flavonoid quantifications in extracts

The total phenolic content of the all extracts were determined by taking pyrocatechol as the standard (Fig. 2).

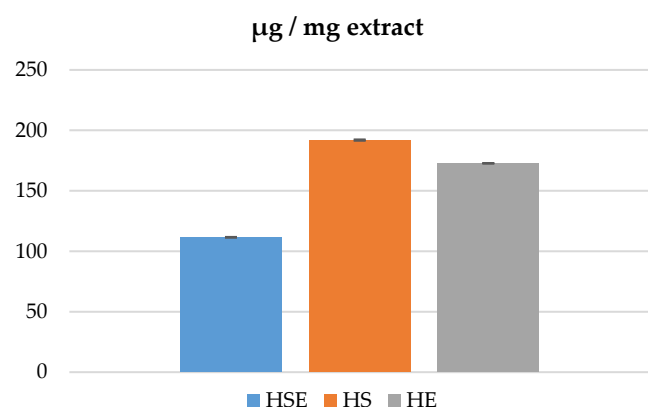


Figure 2. Total phenolic contents of extract of the water:ethanol (HSE), aqueous (HS), and ethanol (HE)

The total phenolic content of the all extracts were determined by taking quercetine as the standard (Fig. 3).

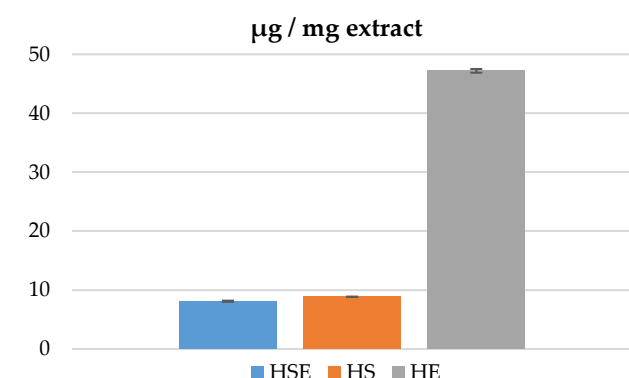


Figure 3. Total flavonoid contents of extract of the water:ethanol (HSE), aqueous (HS), and ethanol (HE)

Based on the results, the water extract was the highest total phenolic content, followed by the ethanol extract, while the water-ethanol extract was the lowest phenolic content. With regards to total flavonoid content, the ethanol extract was the richest, followed by the water extract, with the water-ethanol extract showing the lowest flavonoid level. In general, the ethanol extract

was found to be rich in both phenolic and flavonoid content.

3.2. Results of anti-cholinesterase activity

Anticholinesterase activities of all extracts were determined by inhibition of acetylcholinesterase (AChE) and butyrylcholinesterase (BChE) enzymes. Galantamine was used as a standard. The results are shown in Fig. 4.

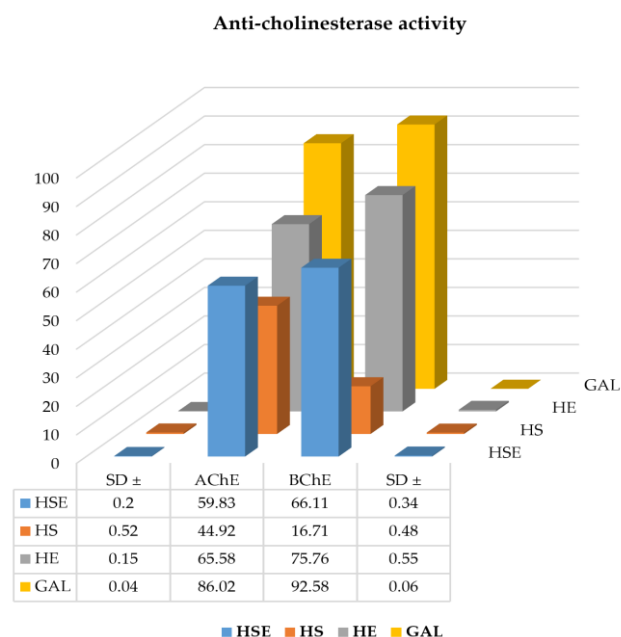


Figure 4. Inhibition of AChE and BChE enzymes by extracts of the water:ethanol (HSE), aqueous (HS), and ethanol (HE), and its standard deviation values (SD)

When evaluating anticholinesterase activity, the ethanol extract showed the highest inhibition rate at 65% for AChE enzyme inhibition, followed by the water-ethanol extract with 59% inhibition. The aqueous extract demonstrated an enzyme inhibition rate of approximately 44%. For BChE enzyme inhibition, the ethanol extract again led with a 75% inhibition rate, while the water-ethanol extract exhibited 66% inhibition. The lowest inhibition rate, at 16%, was sighted in the aqueous extract. Generally, the ethanol extract presented a high inhibition rate for both enzymes.

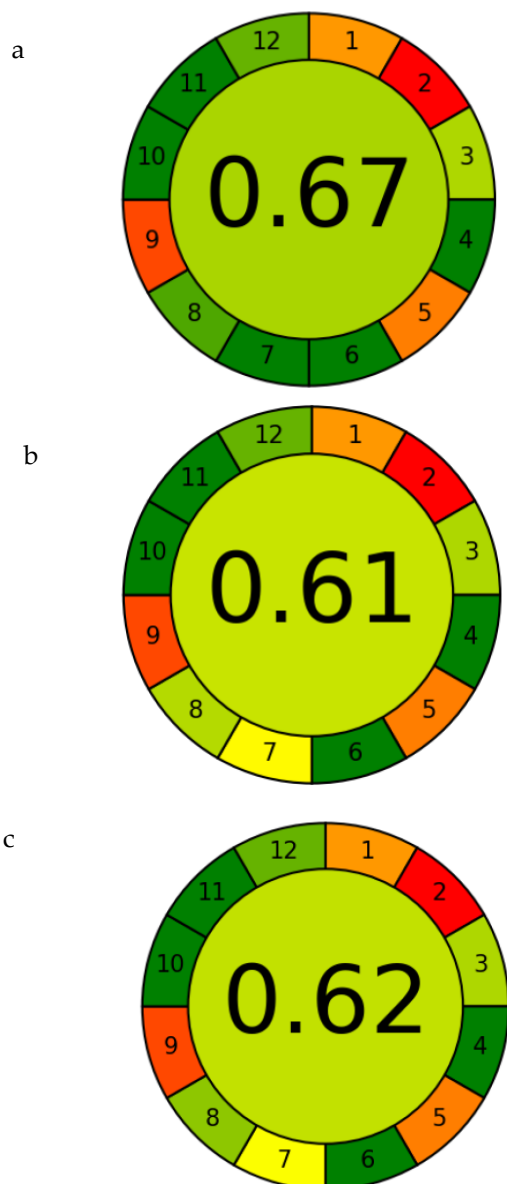
3.3. Results of LC-HR/MS

Calibration equation, R^2 value, relative uncertainty ratio, linear range, LOD-LOQ values, relative standard deviation and recovery of 12 phenolic compounds in all extracts are shown. (Table 2). According to LC-HR/MS analysis of 3 different extracts, we obtained 12 major phenolic compounds (Table 3).

In the LC-HR-MS analysis, the water-ethanol extract demonstrated the highest concentration of Rhamnocitrin at 0.343 µg/mL, followed by Naringenin (0.169 µg/mL), and Kaempferol (0.123 µg/mL).

Table 2. All compounds were determined of all extracts by LC-HR/MS

COMPOUNDS	Relative Uncertainty (%)	Molecular Formula	m/z	Ionization	Lineer Range (µg/mL)	Lineer Regration Equation	LOD/ LOQ	R ²	Recovery	RSD (%)
Apigenin 7-glucoside	3.59	C ₂₁ H ₂₀ O ₁₀	431.0984	Neg	0.3-7	y=0.0246x+0.00306	0.01/0.03	0.9962	96.07	4.61
Ellagic acid	4.20	C ₁₄ H ₆ O ₈	300.9990	Neg	0.05-10	y=0.0085x-0.000612	0.3/1.0	0.9994	101.49	3.90
Quercitrin	3.78	C ₂₁ H ₂₀ O ₁₁	447.0933	Neg	0.05-10	y=0.0179x-0.0003331	0.01/0.03	0.9990	97.00	4.76
Nepetin	2.19	C ₁₆ H ₁₂ O ₇	315.0510	Neg	0.05-10	y=0.0853x+0.00269	0.01/0.03	0.9992	97.76	3.70
Isosakuranetine	3.98	C ₁₆ H ₁₄ O ₅	285.0769	Neg	0.05-10	y=0.0235x+0.000561	0.01/0.03	0.9992	96.56	3.70
Nepetin-7-glucoside	3.07	C ₂₂ H ₂₂ O ₁₂	479.1184	Pos	0.05-10	y=0.00629x-0.0001951	0.01/0.03	0.9997	102.18	3.51
Rhamnocitrin	3.16	C ₁₆ H ₁₂ O ₆	301.0707	Pos	0.05-10	y=0.03122x-0.002136	0.01/0.03	0.9995	103.58	3.27
Hederagenin	1.80	C ₃₀ H ₄₈ O ₄	473.3625	Pos	0.5-10	y=0.00131x+0.00146	0.1/0.3	0.9948	97.49	1.84
Naringenin	4.20	C ₁₅ H ₁₂ O ₅	271.0612	Neg	0.1-10	y=0.0281x+0.00182	0.01/0.03	0.9995	86.65	4.20
Luteolin	3.42	C ₁₅ H ₁₀ O ₆	285.0405	Neg	0.1-10	y=0.117x+0.00848	0.01/0.03	0.9981	96.98	3.42
Hispidulin	3.41	C ₁₆ H ₁₂ O ₆	301.0707	Pos	0.05-10	y=0.02614x+0.0003114	0.01/0.03	0.9993	98.36	3.41
Kaempferol	3.56	C ₁₅ H ₁₀ O ₆	285.0405	Neg	0.5-7	y=0.0827x+0.00953	0.01/0.03	0.9958	90.25	3.58

**Figure 5.** Greenness scores of all extracts by AGREE:Analytical Greenes Calculator software (a: HS, b:HSE, c:HE)

In the ethanol extract, Quercitrin was the most abundant compound at 0.333 µg/mL, followed by Hederagenin (0.183 µg/mL). The water extract included the highest levels of Quercitrin (0.302 µg/mL), whereas

Nepetin (0.002 µg/mL) and Nepetin-7-glucoside (0.06 µg/mL) were found in the lowest amounts. Similarly, Nepetin was also the compound with the lowest concentration in the water-ethanol extract, with a value of 0.003 µg/mL.

3.4. Results of greenness

The results of greenness metrics were presented as below (Fig. 5). The software was evaluated on 12 principles. The weight of score of each principles is not different. The results were obtained for all extracts between 0.61 to 0.67, in terms of examined acceptable green metrics. The highest score (0.67) obtained from aqueous extract. The results were calculated from 11 metrics were same for the each extract, however, only the score of one criteria (criteria 7) was different. This criteria rely on the consumption and recycle of analytical waste. According to this, the extraction methods require large volume of solvent. In this technique, we used large amount of water, water:ethanol, and ethanol, respectively. Accordingly, compare to other solvents, water is more recyclable. Therefore, greenness score of aqueous extract is better than ethanolic and water:ethanolic extracts.

Table 3. 12 phenolic compounds determined in the all extracts by LC-HR/MS

COMPOUNDS	HE (µg/mL)	HS (µg/mL)	HSE (µg/mL)
Apigenin 7-glucoside	0.097	0.083	—
Ellagic Acid	—	0.073	—
Quercitrin	0.333	0.302	—
Naringenin	0.074	0.072	0.169
Nepetin	—	0.002	0.003
Hispidulin	—	0.013	0.054
Luteolin	0.065	—	—
Isosakuranetin	0.069	0.072	0.121
Nepetin-7-glucoside	—	0.06	—
Rhamnocitrin	—	—	0.343
Hederagenin	0.183	0.092	—
Kaempferol	—	—	0.123

Conclusion

In this study, the total phenolic-flavonoid capacities and the total phenolic content of three different extracts from *Hypericum perforatum* L. were investigated using LC-HR/MS, and their anticholinesterase activity was analyzed. Additionally, the sustainability of the extraction process was evaluated through green chemistry analysis of the solvents and extraction methods, using the AGREE: Analytical Greenness Calculator program.

The plant is widely used in Europe to treat anxiety and is also known for its various effects, including wound healing and antispasmodic properties. *H. perforatum* oil is commonly used for wound healing. Its tea has been shown to aid in the treatment of anxiety disorders. The plant is also existing in capsule form and has recently gained attention in the cosmetic industry due to its antioxidant effects. The naphthodianthrone derivatives, flavonoids, biflavonoids, and phloroglucinols it includes are potent chemical compounds with strong antioxidant properties. The aerial parts of *H. perforatum* L. were extracted using 100% water, a 50% ethanol-50% water mixture and 100% ethanol under reflux in a water bath at 60°C. The antioxidant properties and total phenolic-flavonoid content of the resulting extracts were examined using the Folin-Ciocalteu method, while their anticholinesterase activity was analyzed using the Ellman method. LC-HR-MS analysis disclosed that the water-ethanol extract contained the highest concentration of Rhamnocitrin, while the ethanol extract was rich in Quercitrin and Hederagenin. The water extract also indicated high Quercitrin levels, but Nepetin and Nepetin-7-glucoside were present in the lowest amounts across all extracts. The ethanol extract showed the highest levels of total flavonoid content and strong inhibition rates for both AChE (65%) and BChE (75%) enzymes. In spite of the water extract had the highest total phenolic content, its enzyme inhibition rates were lower, especially for BChE (16%). The water-ethanol extract demonstrated moderate phenolic and flavonoid content and intermediate enzyme inhibition. Overall, the ethanol extract exhibited the most potent activity across the assays. The greenness metrics analysis revealed that the aqueous extract achieved the highest score due to its superior recyclability compared to ethanol and water-ethanol extracts. Although most metrics were consistent across extracts, the aqueous extract's better performance in waste consumption and solvent recyclability resulted in a higher overall greenness score.

In conclusion, the results align well, showing that the ethanol extract exhibits strong antioxidant capacity and anticholinesterase activity. Continued chemical and

biological studies on *Hypericum* species will be valuable for the discovery of natural bioactive compounds, contributing to the scientific field.









References

- [1] D. Mabberley, The Plant Book, 1987, Cambridge, Cambridge Univ. Press, New York.
- [2] K. Zouhar, *Hypericum perforatum*, 2004, USA, US Department of Agriculture, Forest Service, Rocky Mountain Research.
- [3] I. Süntar, E. Keleş, H. Akkol, Z. Koca, B. Arslan, A. Yeşilada, A novel wound healing ointment: a formulation of *Hypericum perforatum* oil and sage and oregano essential oils based on traditional Turkish knowledge, *J Ethnopharmacol*, 134(1), 2011, 89–96.
- [4] S. Aslan, [http-1](http://www.bizimbitkiler.org.tr), 2012, Available from: <http://www.bizimbitkiler.org.tr>.
- [5] R.B. Wills, K. Bone, M. Morgan, Herbal products: active constituents, modes of action and quality control, *Nutr Res Rev*, 13(1), 2000, 47–77.
- [6] V. Butterweck, Mechanism of action of St John's wort in depression: what is known?, *CNS Drugs*, 17, 2003, 539–562.
- [7] T. Baytop, Türkiye'de Bitkiler ile Tedavi: Geçmişte ve Bugün, 1999, İstanbul, Nobel Tıp Kitabevleri.
- [8] B. Çubukçu, G. Sarıyar, A.H. Meriçli, N. Sütülpınar, A. Mat, F. Meriçli, *Fitoterapi Yardımcı Ders Kitabı*, 2002, İstanbul, İ.Ü. Basım ve Yayınevi.
- [9] L.Ö. Demirezer, T. Ersöz, İ. Saraçoğlu, B. Şener, *Tedavide Kullanılan Bitkiler FFD Monografıları*, 2007, İstanbul, Nobel Tıp Kitabevleri.
- [10] N. Öztürk, M. Tunçel, İ. Potoğlu-Erkara, Phenolic compounds and antioxidant activities of some *Hypericum* species: A comparative study with *H. perforatum*, *Pharm Biol*, 47(2), 2009, 120–127.
- [11] E. Ersoy, E. Koca, H. Akkol, Z. Koca, B. Arslan, A. Yeşilada, Evaluation of in vitro biological activities of three *Hypericum* species (*H. calycinum*, *H. confertum*, and *H. perforatum*) from Turkey, *S Afr J Bot*, 130, 2020, 141–147.
- [12] V. Gul, et al., Comparative analysis of biochemical content, antimicrobial and antioxidant activities of *Hypericum perforatum* L. species grown in Türkiye, *Pak J Bot*, 55(4), 2023, 1277–1285.
- [13] M. Menegazzi, P. Masiello, M. Novelli, Anti-tumor activity of *Hypericum perforatum* L. and hyperforin through modulation of inflammatory signaling, ROS generation and proton dynamics, *Antioxidants*, 10(1), 2020, 18.
- [14] A. Martinho, et al., Effects of *Hypericum perforatum* hydroalcoholic extract, hypericin, and hyperforin on cytotoxicity and CYP3A4 mRNA expression in hepatic cell lines: A comparative study, *Med Chem Res*, 25, 2016, 2999–3010.
- [15] E. Eroglu, S.N. Girgin, A unique phenolic extraction method from olive oil macerate of *Hypericum perforatum* using DMSO: Assessment of in vitro anticancer activity, LC-MS/MS profile, total phenolic content and antioxidant capacity, *S Afr J Bot*, 139, 2021, 6–11.
- [16] E. Vuko, et al., Chemical composition and new biological activities of essential oil and hydrosol of *Hypericum perforatum* L. ssp. *veronense* (Schrank) H. Lindb., *Plants*, 10(5), 2021, 1014.
- [17] G. Zdunić, et al., Evaluation of *Hypericum perforatum* oil extracts for an antiinflammatory and gastroprotective activity in rats, *Phytother Res*, 23(11), 2009, 1559–1564.
- [18] A.P. Dagnino, et al., Leishmanicidal activity of lipophilic extracts of some *Hypericum* species, *Phytomedicine*, 22(1), 2015, 71–76.
- [19] G. Okmen, N. Balpınar, The biological activities of *Hypericum perforatum* L., *Afr J Tradit Complement Altern Med*, 14(1), 2017, 213–218.

- [20] A.I. Oliveira, et al., Neuroprotective activity of *Hypericum perforatum* and its major components, *Front Plant Sci*, 7, 2016, 1004.
- [21] F. Conforti, et al., Comparative chemical composition and variability of biological activity of methanolic extracts from *Hypericum perforatum* L., *Nat Prod Res*, 19(3), 2005, 295–303.
- [22] H. Kızıldaş, et al., LC-HRMS profiling and antidiabetic, anticholinergic, and antioxidant activities of aerial parts of kinkor (*Ferulago stellata*), *Molecules*, 26(9), 2021, 2469.
- [23] Z. Bingöl, et al., Antidiabetic, anticholinergic and antioxidant activities of aerial parts of shaggy bindweed (*Convolvulus betonicifolia* Miller subsp.)—profiling of phenolic compounds by LC-HRMS, *Heliyon*, 7(5), 2021, e06986.
- [24] S. Eruçar, Bazı bitkisel çayların fenolik madde profili ve antioksidan aktivitelerinin incelenmesi, 2006, Fen Bilimleri Enstitüsü.
- [25] K. Slinkard, V.L. Singleton, Total phenol analysis: automation and comparison with manual methods, *Am J Enol Vitic*, 28(1), 1977, 49–55.
- [26] M.a.I.N. Moreno, M.I. Isla, A.R. Sampietro, M.A. Vattuone, Comparison of the free radical-scavenging activity of propolis from several regions of Argentina, *J Ethnopharmacol*, 71(1-2), 2000, 109–114.
- [27] G.L. Ellman, K. Diane Courtney, V. Andres, R.M. Featherstone, A new and rapid colorimetric determination of acetylcholinesterase activity, *Biochem Pharmacol*, 7(2), 1961, 88–95.
- [28] A. Komersova, K. Komers, A. Čegan, New findings about Ellman's method to determine cholinesterase activity, *Z Naturforsch C*, 62(1-2), 2007, 150–154.
- [29] W. Wojnowski, M. Tobiszewski, F. Pena-Pereira, E. Psillakis, AGREEprep—analytical greenness metric for sample preparation, *TrAC Trends Anal Chem*, 149, 2022, 116553.
- [30] F. Pena-Pereira, W. Wojnowski, M. Tobiszewski, AGREE—Analytical GREENness metric approach and software, *Anal Chem*, 92(14), 2020, 10076–10082.



Sensory and physicochemical characteristics of mulberry leathers enriched with sesame, almond, sunflower seeds, coconut, and peanut

Burak Güler¹ , Cemalettin Baltacı^{1*} , Murat Küçük² , Huri İlyasoğlu³ , Turgut Şahinöz⁴ , Omer Karpuz⁵ , Fırat Yılmaz¹ , Kağan Kılınç⁵ 

¹Gümüşhane University, Faculty of Engineering and Life Sciences, Department of Food Engineering, 29100, Gümüşhane, Türkiye

²Karadeniz Technical University, Faculty of Science, Department of Chemistry, 61080, Trabzon, Türkiye

³Gümüşhane University, Faculty of Health Sciences, Department of Nutrition and Dietetics, 29100, Gümüşhane, Türkiye

⁴Ordu University, Faculty of Health Sciences, Department of Healthcare Management, Ordu, 52200, Türkiye

⁵Gümüşhane University, Faculty of Engineering and Life Sciences, Department of Genetics and Bioengineering, 29100, Gümüşhane, Türkiye

Abstract

This study aimed to investigate the utilization of sesame, sunflower seed, almond, peanut, and coconut as condiments for the enrichment of mulberry leather, known locally as mulberry pestil. The investigation involved a comprehensive analysis encompassing proximate composition, mineral content, color, physicochemical, and sensory properties. The studied parameters of enriched samples were compared with those of the plain sample. Employing multivariate statistical techniques enabled the differentiation of the enriched leather samples. Consequently, the leather samples were categorized into three groups by the principal component analysis according to their physicochemical and chemical attributes. Strong positive correlations were observed among the studied parameters, as indicated by Spearman's rank correlation coefficients. The physicochemical and chemical properties of enriched samples exhibited substantial variability. The enriched products had abundant calcium, potassium, magnesium, iron, and zinc levels. ML samples, particularly those enriched with ingredients like sesame (1815.19 mg/100g) and coconut (1815.19 mg/100g), are distinguished by their high mineral content. These samples are rich in essential minerals such as calcium (1515.01–1815.19 mg/100g), magnesium (738.53–997.37 mg/100g), and potassium (2121.29–2774.07 mg/100g). The novelty of this study lies in the exploration of diverse condiments to enhance the nutritional profile of mulberry leather, offering a unique approach to fortifying this traditional product. These findings revealed that incorporating these condiments enhanced the nutritional values of leather samples, especially in terms of minerals. 100 g of the enriched mulberry leathers had 68.0–70.7 g of carbohydrate, 4.6–5.7 g of protein, 3.6–5.9 g of fat, and 336–359 kcal of energy value. The enriched products might be proposed to provide nutrients and energy in emergencies, especially for adolescents and people affected by disasters.

Keywords: Almond, coconut, mulberry leather, peanut, sesame, sunflower seeds

1. Introduction

Consumers' demand for healthy foods has increased the interest of the food industry and scientists in developing functional food products. Many food products have been reformulated for fortification with compounds providing health benefits such as vitamins, minerals, and bioactive compounds [1]. Fruit leather is a nutritionally dense product made from fruit juices or fruit pulps that has the potential for fortification. Apple, banana, grape, kiwi, mango, mulberry, and pineapple, and other fruits are used in the production of fruit leathers [2–6].

Fruit leathers, also called fruit sheets, strips, or roll-ups, are enjoyed as snacks or desserts worldwide [7]. In Türkiye, a traditional variety known as pestil is

produced as a regional fruit snack. Mulberry is one of the fruits used in pestil (fruit leather) production and has potential beneficial properties such as anti-cholesterol, anti-diabetic, and antioxidant effects because of its bioactive compounds [8]. Various regions of Türkiye are known for producing pestil, a traditional dried fruit product, with Kayseri, Tokat, and Amasya being particularly renowned for their contributions. Each region adds its own unique flavors and methods to the craft. However, Gumushane is distinguished as the center of mulberry leather (ML) production. Gumushane pestil stands out for its use of locally grown mulberries, which provide a distinctive texture and flavor. The region's cool climate and fertile soil enhance the richness

Citation: B. Güler, C. Baltacı, M. Küçük, H. İlyasoğlu, T. Şahinöz, O. Karpuz, F. Yılmaz, K. Kılınç, Sensory and physicochemical characteristics of mulberry leathers enriched with sesame, almond, sunflower seeds, coconut, and peanut, Turk J Anal Chem, 7(1), 2025, 9–21.

***Author of correspondence:** cbaltaci11@gmail.com

Tel: +90 (456) 233 17 93

Fax: N/A

Received: June 24, 2024

Accepted: August 22, 2024

 <https://doi.org/10.51435/turkjac.1594643>

of these mulberries, while the traditional production process results in a thicker, more intensely flavored pestil. Known for its natural sweetness and chewy consistency, Gumushane's pestil is a culinary delight and a symbol of the region's agricultural heritage and craftsmanship. The ingredients of Gumushane pestil are mulberry molasses, honey, milk, wheat flour, and sugar, and condiments such as hazelnuts and walnuts can be used to produce pestil. Gumushane pestil is notable for its unique sensory and physicochemical characteristics, as described in the previous studies [9,10]. It exhibits a distinctively softer and more lustrous texture than other fruit leathers.

The higher nutritional content (mainly carbohydrates) of fruit leather makes it a good energy source. The consumption of fruit leather can contribute to meeting energy requirements, especially for adolescents and communities affected by diseases. Moreover, it helps increase solid fruit intake [11].

This study introduces innovation by utilizing various ingredients such as almonds, sesame, coconut, sunflower seeds, and peanuts as condiments for ML production. This initiative seeks to address a research gap, as previous studies haven't explored the potential of the enrichment of fruit leathers with sesame, almond, sunflower seeds, peanuts, and coconut, especially regarding minerals. This study focuses on a comprehensive investigation of the proximate composition, mineral content, physicochemical properties, color, and sensory characteristics of these enriched fruit leathers.

Enriching ML with condiments like sesame, sunflower seed, almond, peanut, and coconut offers an innovative way to enhance its nutritional value. Locally known as mulberry pestil, ML is a nutrient-dense dried fruit product widely consumed in Türkiye. While previous studies have focused on basic pestil composition or the impact of single ingredients, this study expands on that by examining the effects of multiple condiments on ML's physicochemical, mineral, and sensory properties. Unlike studies that focus on individual ingredients, this work uses multivariate statistical techniques to categorize and differentiate enriched ML samples, providing deeper insights into their physicochemical and chemical attributes.

2. Materials and methods

2.1. Materials

The ingredients used in this study, including mulberry molasses, honey, sugar, wheat flour, coconut, almond, peanut, sesame, and sunflower seeds, were sourced from a local market in Gumushane. The combination of these ingredients, particularly mulberry molasses, coconut, almonds, sunflower seeds, sesame, and peanuts, significantly enhances both the nutritional value and

sensory characteristics of MLs. Almonds contribute healthy fats and protein, while sunflower seeds provide antioxidants and essential vitamins. Sesame seeds are rich in calcium and iron, and peanuts are a valuable source of protein and healthy fats. Together, these ingredients work synergistically, enriching the MLs with a diverse range of nutrients, resulting in a more nutritious and flavorful product.

2.2. Chemicals and equipment

The chemicals and solvents used in this study, all analytical or HPLC grade, were procured from Merck (Darmstadt, Germany), ensuring high purity for precise measurements and reliable results. Solvents such as HMF standard (99%), methanol, NaOH, and HNO₃, all analytical or HPLC grade, were used in various stages for the extraction of compounds, preparation of solutions, and analytical measurements. The names of the instruments used for the analyses are provided in the relevant methods.

2.3. Preparation of mulberry leathers

The procedure began by heating a quantity of water (16.20 kg) until it reached its boiling point. Afterwards, a blend of liquid sugar (5.5 kg, with 75% dry matter), honey (4.2 kg), and molasses (0.8 kg) was introduced into the boiling water while being constantly stirred for 20 minutes. The milk (1.3 L) and a tiny amount of water were vigorously mixed with the flour (2.7 kg) in a different bowl. A fraction of this blend was incorporated into the flour following a comprehensive mixing process. When the flour blend was added to the boiling fluid, it developed "herle." The hand refractometer measured the Brix value of the herle as 30%. Once the temperature of the herle reached its boiling point, the heat was subsequently decreased and sustained for 15 minutes. After cooking, the herle was cooled to around 60–65 °C. The herle mixture and drying of the MLs can be seen in Fig. 1A and Fig. 1B.

Concurrently, the exhibition cloth was prepared. The assortment of condiments, including sesame, almond, sunflower seed, peanut, and coconut, weighing 0.9 kg, was added individually to the herle. The herle was uniformly applied onto the surface of the cloth using a spreader, resulting in a consistent and thin layer. Subsequently, the herle was subjected to a drying process at a temperature of 60 °C using airflow for an estimated period of 10 hours. To make it easier to remove the dried fruit leather from the fabric, the back of the cloth was moistened with water. Following a short 40–50 second period, the ML was separated from the cloth and allowed to complete a 2-hour drying procedure. Each type of condiment yielded around 10 kg of fruit leather. The fruit leathers were packaged under room conditions and await further examination. The appearance of the MLs enriched with condiments is shown at Fig. 1C.



Figure 1. A) Herle mixture B) Drying of MLs C) MLs enriched with condiments

2.4. Physicochemical and chemical analyses

The measurement of titration acidity was conducted by utilizing a pH meter by the titration process outlined in the reference method of the Turkish Standard Institute (TS 1125 ISO 750) [12]. The sample was uniformly mixed and weighed (10 g) in a container. A volume of 75 mL of distilled water was added and mixed using a magnetic stirrer. The mixture was titrated using a 0.1 N sodium hydroxide solution for 60 seconds until the pH level reached 8.3. The results of the samples were given in % (m/m) as anhydrous citric acid (ACA). The pH measurement was performed according to the specifications stated in TS 1728 [13].

The color evaluation was conducted by a Minolta Chromameter (CR-400, Konica Minolta Sensing, Inc., Japan), as described in the study by Quek et al. [14]. The color index consists of three parameters: L^* for darkness/whiteness, a^* for greenness/redness, and b^* for blue/yellow. 5 g of sample was placed into the sample container. The device provided direct readings of L^* , a^* , and b^* values. The total color difference was calculated using the formula below

$$\Delta E^*(\text{the total color difference}) = \sqrt{(\Delta L^2 + \Delta a^2 + \Delta b^2)} \quad (1)$$

The total solids content was assessed via the standard method of the TS [15]. A sample of 10 g was weighed in a 100 mL beaker with an accuracy of 0.01 g. Following dissolving, the mixture was put into 200 mL flasks and then filled with water until reaching the designated line. The mixture was subsequently filtered using specialized strainer paper. The solution was measured at a temperature of 20 °C using a refractometer (SOIF WYA-2S digital desktop Abbe refractometer, Soif Optical Instruments, China). The residual substance on the filter paper was desiccated and measured until it attained a constant weight in a drying oven set at 130°C.

100 g of the samples were measured to find the amount of condiment. The condiments were meticulously partitioned using utensils such as knives and scissors. Later, a balance was used to measure each component of the condiment [16]. The thickness of the

ML samples was measured with a digital caliper (Robocombo, 0-150 mm).

The moisture contents were tested following the TS standard procedure [17]. A sample weighing 5 g was placed in aluminum cups, which were then heated to a temperature of 103 °C until the weight of the sample remained constant (Apin, Lab Drying Equipment, SH-FDO54, Jaeho Lee Samheung Energy Co. Ltd., South Korea). The results were expressed in g/100 g.

A protein analyzer instrument (Gerhardt, Bonn, Germany) based on the Kjeldahl principle was utilized to determine the crude protein content of the samples, explicitly applying the TS method [18]. The crude protein content was calculated using a factor of 6.25.

The fat content was assessed by applying the TS reference technique [19]. The fat content obtained from the sample milled in the blender was transferred into a 5 g Soxhlet cartridge, which was then sealed with hydrophilic cotton. The collection flask was heated to a constant weight of 103 °C and then weighed as tare. The material was extracted using a Gerhardt classic Soxhlet device (Gerhardt, Bonn, Germany) for 6 hours. The residual solvent in the collection flask was removed entirely. It was placed in an oven set at 103° C, and the amount of crude fat was determined by weighing it to a preset level.

Crude fiber analysis was conducted according to the TS 6932 standard [20]. A sample of 1 g was measured using a 250-milliliter beaker. A volume of 100 mL of a solution containing 1.25% sulfuric acid was added and subjected to heat. Once it reached the boiling point, it was further boiled for 30 minutes. Then, 10 mL of a KOH solution with a concentration of 28% was added, and the mixture continued to heat for 30 minutes. The heated sample was filtered using a preheated glass filter. The item was rinsed with boiling pure water two more times. Ultimately, it was cleansed using acetone. The residues of the glass filter were desiccated in an oven and an automatic drying cabinet at 130°C for an hour. After cooling in the desiccator, the dried substance was weighed. The glass filter weighed beforehand was inserted into the incinerator and subjected to combustion for 30 minutes at a temperature ranging from 550 to

600°C (MF-12, Nuve, Ankara, Türkiye). Following the cooling in the desiccator, the remaining substance was weighed.

The TS reference technique determined the ash content [21,22]. 2.5 g of samples were weighed and placed in a porcelain crucible. The samples were then burned at 550 °C until their weight remained constant (MF-12, Nuve, Ankara, Türkiye). The resultant ash was subjected to analysis of insoluble ash in HCl. The porcelain crucible was filled with 25.0 mL of 10% HCl and then immersed in boiling water for up to 60 minutes. Once it had cooled down, it was passed through the ashless strainer paper. The complete removal of HCl was achieved by rinsing with pure hot water. A volume of 0.1 N AgNO₃ solution was introduced into a tube to verify this. The washing process persisted until the absence of any white sediment. The non-dissolvable residue in hydrochloric acid was examined using an alternative technique of TS [21]. The filter paper was placed inside the porcelain crucible and dried. Following exposure to the flame, the ash was transferred to the muffle furnace (MF-12, Nuve, Ankara, Türkiye) at a constant temperature of 525±10 °C. The substance was cooled down and put into a desiccator. Once the weighing temperature was attained, it was weighed.

The samples incinerated in the microwave digestion unit were analyzed for minerals using the ICP-MS device, following the reference protocol [23]. Once the ash samples were dissolved in a solution of 10% nitric acid, they were precisely adjusted to a volume of 50 mL using ultrapure water. The metal ions in the solutions were determined using the ICP-MS equipment (7700, Agilent Technologies, Santa Clara, CA, USA). Before conducting measurements using ICP-MS, the instrument was calibrated using mixed standard solutions containing the metal ions under study [23]. The performance parameters of the ICP-MS method for metal analysis are provided in Table 1. The LOD and LOQ were calculated based on 20 blank samples, with the formulas as follows:

$$LOD \text{ (Limit of Detection)} = Blank + 3 \times Sd \quad (2)$$

$$LOQ \text{ (Limit of Quantification)} = Blank + 10 \times Sd \quad (3)$$

The quantification of total sugar, glucose, fructose, and sucrose was done with the methodologies described by Yuksel et al. [10]. 5 g of the samples were dissolved in 40 milliliters of distilled water at room temperature. A volume of 25 mL of methanol was added to the mixture, which was then transferred to a volumetric flask. The solution underwent filtration using a membrane filter and was transferred to the vials. HPLC-RID analysis conditions were as follows:

Flow rate: 1.3 mL/min.

Moving phase: Acetonitrile / water (80:20) volumetric

Column temperature: 30 °C ± 1 °C

Injection volume : 10 µl

Device : HPLC-RID (Thermo Finnigan HPLC)

Peaks were identified in both the standards and samples, and the areas of these peaks were quantified. A linear calibration graph was constructed to display peak areas measured in micrograms per milliliter. The data collection and calculating method determined glucose, fructose, and sucrose percentages.

The hydroxymethylfurfural (HMF) quantification was conducted using the method of Baltaci and Aksit [24]. 5 g of the sample was placed into a 50 mL container. Then, 25 mL of pure water was added to dissolve the material. To prevent the degradation of HMF, 0.5 mL of Carrez I and 0.5 mL of Carrez II were added. The sample, which was prepared using a funnel, was filtered. The solution was transferred into vials, filtered via a 0.45-micron filter, and injected into the prepared HPLC system (Thermo Finnigan HPLC, Thermo Electron, San Jose, CA). The calibration curve was prepared using standards of HMF at concentrations of 1.0, 2.0, 4.0, 8.0, and 12.0 mg/L. The performance parameters of the HPLC method for HMF analysis are as follows: The linear range is 1.0–12 µg/g, with a calibration curve equation of $y=7036x-0.30$ and an R^2 value of 0.999. The limit of detection (LOD) is 0.01 µg/g, and the Limit of Quantification (LOQ) is 0.03 µg/g. Precision is demonstrated by a relative standard deviation for repeatability (RSD_r) of 1.58%, which is below the Horwitz value, and for reproducibility (RSD_R), it is 2.56%, also below the Horwitz value. The recovery rates for HMF analysis are 98.83% at 25 µg/g, 97.18% at 50 µg/g, and 99.39% at 75 µg/g.

2.5. Sensory analysis

The analysts were comprised of 10 individuals who were well-educated (students of the Department of Food Engineering). The panel was evenly divided between 5 males and 5 females, ages 18 to 24, and all members were nonsmokers. An evaluation assessment of fruit leather was completed, examining its color, taste, smell, and appearance. The sensory scores, ranging from 1 to 4, were derived from the analysis [16].

2.6. Statistical analysis

Agglomerative hierarchical clustering (AHC), preference mapping (PREMAP), and principal component analysis (PCA) were executed by employing the Microsoft Excel program with the assistance of XLSTAT (Addinsoft (2024), XLSTAT statistical and data analysis solution, New York, USA, <https://www.xlstat.com>).

Table 1. Performance parameters of the method in ICP-MS for metals analysis

No	Mineral	Calibration curve	R2	RSD%		Linearity ($\mu\text{g/mL}$)	LOD/LOQ ($\mu\text{g/mL}$)	Recover (%)	
				RSDr	RSDR			Intra-day	Inter-day
1	Na	$y = -9066924.3x + 244348.2$	0.998	0.52	0.71	0.5-25	0.03/0.09	100.11	100.83
2	Mg	$y = -2307216.6x + 16968.9$	0.995	1.03	1.06	0.3-9	0.05/0.15	99.63	100.16
3	Al	$y = 12250x + 12162.9$	0.971	0.94	2.08	0.5-10	0.7/2.22	99.68	100.68
4	Ca	$y = 338057x + 27399.8$	0.999	0.82	1.61	5-80	0.7/0.21	100.10	99.47
5	K	$y = 2679658x + 300146.5$	0.998	0.75	1.23	5-100	0.02/0.07	99.69	100.41
6	Cr	$y = 19224.9x + 2095.1$	0.957	0.77	1.44	0.01-0.10	0.20/0.60	99.72	100.55
7	Mn	$y = 13370.8x + 3787.2$	0.999	1.09	2.15	0.01-0.25	0.005/0.015	100.24	100.45
8	Fe	$y = 16734.0x + 99314$	0.997	1.21	1.82	0.1-5	0.12/0.40	99.63	100.77
9	Co	$y = 27170.7x + 380.0$	0.995	1.51	2.16	0.01-1.0	0.02/0.08	100.00	99.67
10	Ni	$y = 6903.2x + 3978.1$	0.996	0.58	2.09	0.01-0.5	0.02/0.06	100.02	99.88
11	Cu	$y = 18008.0x + 7625.2$	0.999	1.17	2.41	0.1-0.4	0.02/0.06	99.70	99.51
12	Zn	$y = 4102.8x + 134853.9$	0.999	0.64	1.31	0.01-30	0.06/0.22	99.81	100.79
13	As	$y = 2608.0x + 52.3$	0.999	1.49	2.21	0.001-0.02	0.002/0.006	99.83	99.97
14	Pd	$y = 15301x + 6444.2$	0.999	0.98	1.23	0.2-10	0.01/0.03	100.32	100.68
15	Ag	$y = -47157.7x + 7158.4$	0.999	0.61	1.48	0.02-0.16	0.01/0.03	100.13	100.12
16	Cd	$y = 11116x + 779.4$	0.999	0.77	1.93	0.01-5.0	0.02/0.06	99.22	99.98
17	Sn	$y = 272.1x + 149.9$	0.999	1.23	1.12	0.01-0.5	0.02/0.06	100.15	100.42
18	Ba	$y = 13516.8x + 6324.7$	0.998	1.08	1.19	0.05-0.5	0.01/0.03	100.06	100.72
19	Hg	$y = 85457.1x + 2040.2$	0.998	0.83	1.11	0.1-5	0.03/0.09	100.09	99.67
20	Pb	$y = 53700.4x + 42830.9$	0.999	1.08	1.19	1-50	0.7/2.20	99.23	100.45
21	P	$y = 101446.1x + 4877.1$	0.996	0.82	1.11	0.1-5	0.2/0.6	98.12	99.77

3. Results and Discussion

3.1. Physicochemical properties

Table 2 presents the findings about physicochemical parameters. Significant differences in the physicochemical parameters were observed among the samples ($p < 0.05$).

One of the significant physical properties is the thickness of fruit leather, which plays a dual role as an edible film. The thicknesses of MLs ranged from 1.31 mm to 2.21 mm. According to Yıldız [9], the MLs exhibited a thickness value ranging from 0.80 mm to 1.25 mm. Yıldız and Boyracı [25] determined the thickness of pestil samples, varying from 0.92 mm to 1.12 mm. Compared with the previous studies, the ML with the condiments displayed notably greater thickness values.

Addressing acidity and pH, the MLs exhibited acidity values of 0.12% and 0.19%, with pH values of 6.05 and 6.13, respectively. The plan ML had a lower acidity value than the ML with condiments. The acidity of fruit leather mainly depends on the fruit pulp or juice used in the production. Yıldız [9] reported the ML acidity values of 0.14% and 0.15%. In another study, Karaoğlu et al. [26] determined the acidity and pH values of MLs, ranging from 0.40% to 0.73% and 5.67 to 5.81, respectively. According to Tontul and Topuz [27], the pomegranate leathers exhibited pH values varying from 3.61 to 3.68.

3.2. Color properties

The color attributes of the leather samples displayed significant differences with a confidence level of 95% ($P < 0.05$) (Table 3). The color analyses were elucidated using PCA at a rate of 99.18% (Fig. 2). The color differences (ΔE^*ab) were found to be more significant

based on the PCA loadings and scores. The MLs enriched with coconut and sunflower seeds showed a lighter hue. Conversely, the plain ML had a more intense hue. Different condiments in the fruit leather formulations greatly impacted the values of L^* , a^* , b^* , and ΔE^*ab . The variations in the MLs' color values could arise from using different condiments during production. The color of fruit leather products can be modified through baking and drying methods employed during manufacturing. Suna and Özkan-Karabacak [28] determined the L^* , a^* , and b^* values of the ML samples dried with differing methods, ranging from 28.57 to 35.42, from 4.44 to 8.15, and from 11.15 to 19.06, respectively. According to an investigation on the effects of sugars and cooking time on the color properties of ML, the L^* , a^* , and b^* values varied from 31.64 to 35.86, from 5.33 to 9.41, and from 0.63 to 8.55, respectively [29]. Except for the plain fruit leather samples, the ΔE^*ab analysis revealed statistically noticeable variations among the samples ($P < 0.05$), as demonstrated in Table 3.

3.3. Proximate composition

The proximate composition of the ML samples is presented in Table 2. The moisture content of the ML samples ranged from 15.49% to 19.43%. Moisture content is a pivotal characteristic of fruit leather and should be kept lower to ensure extended product storage without deterioration. The moisture content of fruit leather varies depending on formulation and drying process. The moisture content of apricot, grape, and MLs procured from the local market was determined to range from 11.8% to 18.3% [30]. An investigation of the development of kiwi leather using different hydrocolloids showed

Table 2. Physicochemical and chemical properties of MLs

Sample	Plain ML	Almond-added ML	Peanut-added ML	Sunflower seed-added ML	Sesame-added ML	Coconut-added ML
Thickness (mm)/diameter	1.31±0.10 ^c	2.15±0.10 ^a	2.21±0.05 ^a	2.21±0.07 ^a	1.63±0.13 ^b	1.58±0.09 ^b
Condiment (g/100 g)	0.01±0.01 ^b	10.69±0.06 ^a	10.72±0.17 ^a	10.73±0.17 ^a	10.77±0.12 ^a	10.77±0.21 ^a
Total solids (g/100 g)	84.48±0.07 ^a	82.71±0.17 ^b	82.66±0.28 ^b	82.12±0.50 ^b	79.69±0.33 ^c	79.49±0.48 ^c
Moisture (g/100 g)	15.49±0.01 ^d	16.79±0.01 ^c	16.87±0.01 ^c	17.12±0.02 ^b	19.43±0.03 ^a	19.39±0.02 ^a
Acidity (ACAEq.) (g/100 g)	0.12±0.01 ^c	0.19±0.01 ^a	0.16±0.01 ^b	0.16±0.01 ^b	0.18±0.01 ^a	0.19±0.01 ^a
pH	6.13±0.04 ^a	6.05±0.03 ^b	6.07±0.02 ^b	6.07±0.02 ^b	6.07±0.02 ^b	6.11±0.02 ^a
HMF (mg/kg)	3.45±0.14 ^a	3.08±0.08 ^b	3.17±0.07 ^b	3.21±0.06 ^b	1.75±0.10 ^c	1.69±0.10 ^c
Protein (g/100 g)	6.75±0.15 ^a	5.70±0.07 ^b	5.57±0.11 ^b	5.70±0.06 ^b	4.70±0.12 ^c	4.63±0.15 ^c
Total ash (g/100 g)	0.44±0.02 ^c	0.65±0.03 ^{ab}	0.66±0.03 ^b	0.67±0.02 ^b	0.77±0.03 ^a	0.77±0.02 ^a
10% HCl Insoluble ash (g/100 g)	0.14±0.02 ^c	0.14±0.01 ^c	0.14±0.01 ^c	0.15±0.01 ^{bc}	0.18±0.01 ^a	0.17±0.02 ^{ab}
Total sugar (g/100 g)	39.01±0.01 ^a	39.28±0.01 ^a	39.28±0.02 ^a	39.28±0.02 ^a	39.47±0.03 ^a	39.47±0.51 ^a
Glucose (g/100 g)	10.35±0.10 ^c	10.67±0.02 ^b	10.78±0.10 ^{ab}	10.91±0.06 ^a	10.78±0.11 ^{ab}	10.70±0.12 ^b
Fructose (g/100 g)	10.31±0.04 ^d	10.54±0.07 ^c	10.63±0.06 ^{bc}	10.75±0.10 ^{ab}	10.86±0.12 ^a	10.88±0.01 ^a
Sucrose (g/100 g)	18.65±0.04 ^a	18.27±0.12 ^b	18.41±0.08 ^b	18.30±0.06 ^b	18.40±0.07 ^b	18.38±0.14 ^b
Cellulose (g/100 g)	0.36±0.03 ^e	0.75±0.03 ^d	0.84±0.03 ^c	0.75±0.03 ^b	1.32±0.03 ^b	1.44±0.02 ^a
Total fat (g/100)	0.23±0.02 ^e	5.45±0.06 ^b	5.90±0.09 ^a	5.84±0.04 ^{ab}	5.76±0.13 ^d	3.63±0.08 ^d
Total mineral (g/100 g)	0.46±0.05 ^c	0.67±0.04 ^{ab}	0.61±0.01 ^b	0.70±0.05 ^a	0.65±0.04 ^{ab}	0.70±0.03 ^a
Carbohydrate (g/100 g)	76.62±0.14 ^a	70.66±0.07 ^b	70.16±0.12 ^c	69.93±0.15 ^c	68.03±0.30 ^d	70.14±0.12 ^c
Energy (kcal/100 g)	336.67±0.12 ^d	356.7±0.41 ^b	358.57±0.39 ^a	357.27±0.10 ^b	346.68±0.48 ^c	336.04±0.35 ^e

Note: Results are presented as means ± standard deviations. Different letters (a-e) in the same lines are significantly ($P < 0.05$) different.

that the moisture content of the leather samples varied from 17.45% to 22.00% [2]. Our study's results fell within the range of 79.49–84.48% concerning the total solids content of the ML samples. These values were comparable with the values reported by Çağındı & Otleş [30] and Bayram [31] for apricot, grape, and MLs.

The primary macronutrient in the ML samples was carbohydrate, ranging from 68.03 to 76.62 g/100 g. The protein and fat contents of the MLs varied from 4.63 to 6.75 g/100 g and 0.23 to 5.90 g/100 g, respectively. Legal regulations do not stipulate a specific limit for the macronutrients. As shown in Table 4, there are significant correlations between the quantity of condiments and the macronutrients ($p < 0.05$). A significant negative correlation for both carbohydrate ($r = -0.95$) and protein ($r = -0.78$) and a significant positive correlation for fat ($r = 0.92$) were observed. The plain ML contained the highest contents of carbohydrates (76.62 g/100g) and protein (6.75 g/100g), while the peanut-added ML had the highest fat content (5.90 g/100g). The levels of macronutrients in fruit leather depend on the fruit and other ingredients used in the production.

According to Yıldız [9], the plain ML had protein (4.34%) and fat (0.98%). In another study, the carbohydrate, protein, and fat contents of apricot, grape, and MLs were reported to range from 73.7% to 82.4%, from 3% to 6%, and from 0.2% to 3.4%, respectively [30]. Sarma et al. [1] determined that the banana leather contained carbohydrates (56.04%), protein (6.23), and fat (0.18%).

The energy value of the MLs ranged from 336.04 to 358.57 kcal/100 g (Table 2). The plain ML had the lowest energy value, whereas the peanut-added ML exhibited the highest. A 100-gram portion of MLs accounts for approximately 17% of an adult's daily reference intake (RI) based on a 2000-calorie diet. Due to their higher carbohydrate contents and energy values, the MLs can serve as wholesome supplementary meals, snack options, and rapid energy sources. Moreover, they can be alternative options for the high-energy foods needed in short-term nutrition emergency services in case of disasters.

Table 3. Color measurement of MLs

Sample	L*	a*	b*	ΔE^*ab
Plain ML	41.33±1.23 ^d	12.58±1.06 ^a	21.44±1.13 ^a	0.00f
Sesame-added ML	43.49±0.53 ^c	9.63±0.14 ^b	18.95±0.84 ^b	3.81±0.33 ^e
Almond-added ML	43.67±0.89 ^c	7.18±0.05 ^d	13.89±0.29 ^d	8.96±0.33 ^c
Coconut-added ML	47.63±0.59 ^a	6.03±0.13 ^e	12.09±0.26 ^e	12.41±0.38 ^a
Peanut-added ML	43.32±1.19 ^c	7.81±0.22 ^c	15.97±0.31 ^c	7.98 ±0.33 ^d
Sunflower seed-added ML	45.93±0.26 ^b	6.80±0.34 ^d	11.68±0.75 ^e	11.62±0.16 ^b

The data are shown as the mean of three determinations, accompanied by the associated ± standard deviation. A variety of letters (a-f) in the same column indicate significant differences, attaining statistical significance at the 95% level ($P < 0.05$). In this context, the symbol "L*" represents the degree of darkness or lightness, where a value of 0 corresponds to black and a value of 100 corresponds to white. Similarly, the symbol "a*" represents the absence of greenness (-a) and the presence of redness (+a), while the symbol "b*" indicates the absence of blueness (-b) and the presence of yellowness (+b).

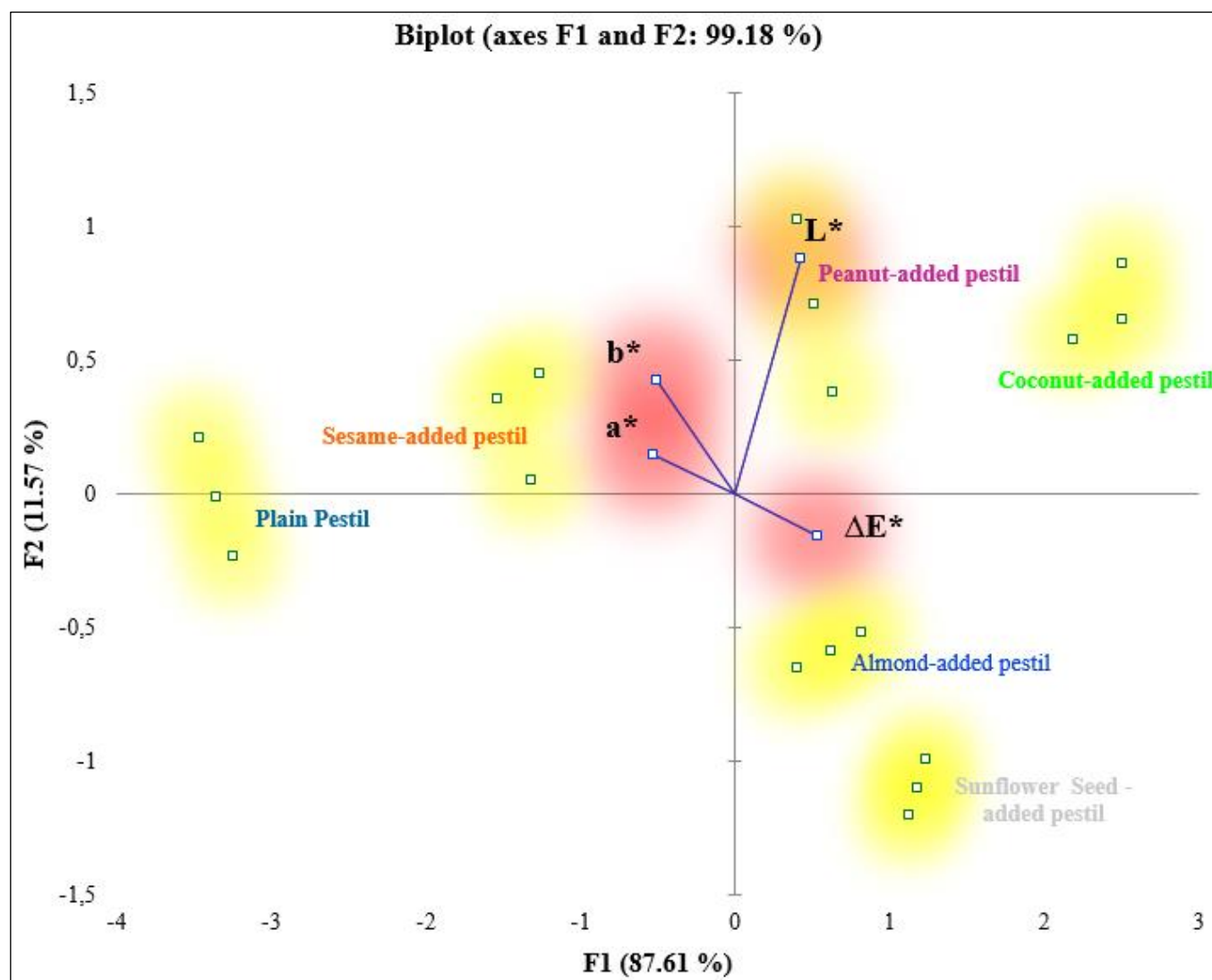


Figure 2. PCA analysis of the color properties of the MLs with different condiments

The MLs showed no significant differences in total sugar content ($p > 0.05$). The total sugar content of ML was not explicitly specified in the TS 12677 [16] ML standard. The total sugar (39.00-39.50%), glucose (10.30-10.90%), and fructose (10.30-10.90%) levels of the ML samples were found to be lower than results of the previous studies. Bayram [31] reported that the MLs contained total sugar levels ranging from 47.60% to 59.20%, glucose levels from 11.00% to 15.80%, and fructose levels from 7.10% to 9.20%. Yildiz [9] determined that MLs had sugar content ranging from 51.30% to 62.50%. The lower values in our study could be attributed to the differences in the types and levels of sugars and honey used in the formulation of MLs.

There is no prescribed cellulose limit for fruit leather within any legal regulations. As indicated in Table 4, there is a noticeable positive correlation between cellulose and condiment content ($r = 0.67$). Among the ML samples, sesame and coconut exhibit elevated cellulose content. Bayram [31] examined the MLs with condiments such as hazelnut and walnut, revealing

varying cellulose ratios of 2.0% to 2.20%. These values were higher than those found in our study, which might be attributed to the choice of ingredients.

The ash content of the MLs ranged from 0.44% to 0.77%. As shown in Table 3, strong positive correlations indicate that when one variable increases, the other tends to increase as well. For example, protein and total ash ($r = 0.97$) and glucose and fructose ($r = 0.88$) both show a simultaneous increase, suggesting that these components are closely related and tend to vary together. On the other hand, strong negative correlations indicate an inverse relationship, where an increase in one variable leads to a decrease in another. For instance, acidity and protein ($r = -0.95$) and moisture and protein ($r = -0.97$) demonstrate such relationships, implying that higher acidity or moisture content may result in lower protein levels. These correlations provide valuable insights into how various chemical and physicochemical properties of the samples interact, helping to better understand the underlying dynamics between these factors.

Table 4. Correlation matrix for the physicochemical and chemical parameters of products

Variables	Thickness	Amount of Condiment	Total Solids	Moisture	Acidity ben	pH	HMF	Protein	Total Ash	% 10 HCl Insoluble	Total Sugar	Glucose	Fructose	Sucrose	Cellulose	Total Fat	Carbohydrate	Energy	Total Mineral
Thickness	1.00	0.66	0.07	-0.16	0.35	-0.78	0.33	-0.07	0.27	-0.38	0.15	0.65	0.18	-0.62	-0.08	0.79	-0.50	0.93	0.50
Amount of Condiment		1.00	-0.68	0.62	0.86	-0.67	-0.45	-0.78	0.88	0.25	0.84	0.83	0.77	-0.78	0.67	0.92	-0.95	0.56	0.86
Total Solids			1.00	-0.98	-0.73	0.10	0.92	0.95	-0.92	-0.72	-0.96	-0.49	-0.89	0.38	-0.97	-0.46	0.79	0.17	-0.65
Moisture				1.00	0.71	-0.09	-0.97	-0.96	0.89	0.75	0.95	0.44	0.87	-0.32	0.98	0.39	-0.74	-0.25	0.60
Acidity (ACA eq.)					1.00	-0.52	-0.62	-0.80	0.85	0.39	0.85	0.62	0.71	-0.74	0.75	0.69	-0.82	0.25	0.81
pH						1.00	-0.04	0.28	-0.43	0.23	-0.34	-0.64	-0.24	0.64	-0.12	-0.79	0.61	-0.78	-0.50
HMF							1.00	0.89	-0.78	-0.78	-0.86	-0.25	-0.78	0.16	-0.95	-0.20	0.59	0.43	-0.46
Protein								1.00	-0.95	-0.62	-0.98	-0.55	-0.88	0.47	-0.97	-0.57	0.84	0.04	-0.69
Total Ash									1.00	0.53	0.97	0.68	0.91	-0.62	0.91	0.71	-0.92	0.15	0.77
% 10 HCl Insol. Ash										1.00	0.62	0.13	0.64	0.01	0.70	0.10	-0.42	-0.39	0.29
Total Sugar											1.00	0.63	0.91	-0.54	0.96	0.65	-0.90	0.05	0.76
Glucose												1.00	0.67	-0.77	0.46	0.85	-0.82	0.60	0.78
Fructose													1.00	-0.43	0.88	0.60	-0.84	0.05	0.72
Sucrose														1.00	-0.35	-0.74	0.68	-0.56	-0.75
Cellulose															1.00	0.43	-0.76	-0.20	0.62
Total Fat																1.00	-0.91	0.79	0.71
Carbohydrate																	1.00	-0.46	-0.79
Energy																		1.00	0.35
Total Mineral																			1.00

Note: Values in bold are different from 0 with a significance level $\alpha=0.05$. Significant correlations are displayed in bold. Correlation coefficients vary -1 and 1. The closer is to 1 or -1, stronger is the link between two variables. **Negative** values indicate negative correlation, and **positive** values indicate positive correlation. Values close **zero** reflect the absence of correlation.

The ML samples incorporating coconut and sesame yielded higher values than the others, whereas the plain leather exhibited a lower value. Bayram [31] reported that the ash content was 0.35%-0.40% and 0.45%-0.75% for the plain ML and the ML with hazelnut and walnut, respectively. According to a study using different flours in the production of ML, the ash contents of ML samples ranged from 0.66 g/100 g to 1.71 g/100 g [10].

3.4. Mineral content

Minerals collaborate synergistically with vitamins in our bodies, optimizing the effective utilization of these vitamins and other essential nutrients. A comprehensive evaluation of 21 minerals was undertaken in the ML samples, and these results are provided in Table 6. All condiment-added MLs displayed significant sodium, potassium, calcium, phosphorus, magnesium, manganese, iron, and zinc abundances. Additionally, other elements, including copper and nickel, were detected. Notably, metals such as arsenic (As), lead (Pb), cadmium (Cd), and mercury (Hg) were detected below the limit of quantification (LOQ) by the maximum residue limits regulated by Turkish Food Codex regulations on contaminants. A study highlighted the elevated presence of potassium, calcium, and zinc in apricot fruit leather, whereas mulberry fruit leather exhibited a higher amount of magnesium [30].

As indicated in Table 4, there is a strong positive correlation between the amounts of condiments and

total mineral content ($r = 0.86$). Minerals like calcium, phosphorus, magnesium, manganese, and zinc were more pronounced in MLs enriched with condiments than the plain ones, indicating that incorporating condiments enhanced the nutritional values of MLs. The peanut-added ML had the lowest sodium. A reduction in the sodium intake and an increase in the potassium intake are recommended for a healthy diet. The peanut-added sample might have superiority over other MLs since the incorporation of peanuts decreased sodium and potassium content.

3.5. HMF levels

HMF is an indicator of heat treatment in foods and is regulated by standards. For example, mulberry fruit leather's maximum allowable HMF content is 50 mg/kg [16]. In our examination, which spanned six MLs, the HMF concentrations ranged from 1.69 mg/kg to 3.45 mg/kg, with plain ML containing the highest levels and coconut-added ML having the lowest. HMF content is extensively used to indicate Maillard reactions and browning in several foods, including honey and molasses [32]. The gel structure known as "herle," the initial phase of fruit leather production, is formed by boiling a blend of fruit pulp or juice, flour, sugar, honey, and water for approximately two hours. The process conditions for boiling treatment in the production of herle can impact the HMF content. A study comparing HMF formation resulting from maintaining herle at

Table 5. The loadings and the scores of the first five rotated principal components

The Loadings	F1	F2	F3	F4	F5
Thickness (mm)	0.352	0.894	0.111	0.041	-0.043
Amount of condiment (g/100 g)	0.927	0.341	0.006	-0.011	-0.014
Total solids (g/100 g)	-0.887	0.428	-0.023	-0.010	0.063
Moisture (g/100 g)	0.860	-0.499	0.014	-0.047	-0.045
Acidity (ACA eq.) (g/100 g)	0.888	0.074	-0.306	-0.112	0.219
pH	-0.489	-0.721	-0.008	0.375	-0.072
HMF (mg/kg)	-0.738	0.651	0.027	0.125	0.004
Protein (g/100 g)	-0.934	0.290	0.016	0.129	0.074
Total Ash (g/100 g)	0.978	-0.093	-0.007	-0.075	-0.066
% 10 HCl insol. ash (g/100 g)	0.525	-0.653	0.270	0.201	0.418
Total sugar (g/100 g)	0.973	-0.211	-0.002	-0.071	-0.025
Glucose (g/100 g)	0.767	0.456	0.058	0.288	-0.155
Fructose (g/100 g)	0.907	-0.207	0.184	0.173	-0.128
Sucrose (g/100 g)	-0.676	-0.505	0.427	-0.142	-0.103
Cellulose (g/100 g)	0.879	-0.448	-0.016	-0.081	-0.091
Total fat (g/100)	0.782	0.570	0.211	-0.045	0.051
Carbohydrate (g/100 g)	-0.961	-0.185	-0.170	0.039	-0.020
Energy (kcal/100 g)	0.252	0.930	0.220	-0.014	0.088
Total mineral (g/100 g)	0.845	0.215	-0.237	0.275	0.000
The Scores	F1	F2	F3	F4	F5
Plain pestil	-7.179	-1.686	0.892	0.014	0.014
Almond-added pestil	0.159	2.247	-0.869	-0.526	0.571
Peanut-added pestil	-0.060	2.009	0.698	-0.326	-0.390
Sunflower seed-added pestil	0.792	2.085	0.227	1.051	-0.145
Sesame-added pestil	3.347	-1.700	0.667	-0.460	0.263
Coconut-added pestil	2.941	-2.955	-0.703	0.247	-0.313

temperatures of 60, 70, 80, 90, 100, and 110 °C for 2, 4, and 6 hours demonstrated a substantial increase in HMF

with a higher temperature and longer duration. It is recommended that the temperature not exceed 90 °C during fruit leather production [33]. Moreover, studies suggest that drying can significantly influence HMF formation [27,31]. Previously reported HMF concentrations were 27.94 mg/kg for plain ML, 21.42 mg/kg for hazelnut-added ML, and 18.15 mg/kg for walnut-added ML [9]. Yildiz and Boyraci [25] indicated that hazelnut- and walnut-added pestil contained HMF levels of 17.26 mg/kg and 15.24 mg/kg, respectively. In another study, the HMF content of MLs ranged from 1.42 mg/kg to 6.60 mg/kg [10].

3.6. Sensorial properties

The evaluation of sensory attributes plays a crucial part in determining the overall quality of food. Evaluating and discussing traditional foods' taste and general quality with consumers is essential [34]. The sensory analysis results for six samples of MLs were analyzed using several analytical techniques, including PCA, AHC, and PREMAP (Fig. 3A and Fig. 3B). The AHC analysis led to the classifying of sensory outcomes into seven separate groups (Fig. 3B). The PREMAP technique efficiently gathered 81% of the sensory analysis data by utilizing PCA and AHC analyses. The fourth group displayed the highest level of approval in the sensory evaluations. This group primarily consisted of fruit leather samples enriched with coconut, sesame, and almond. This group, located in the red zone on the PREMAP, received the highest ratings regarding

appearance, taste, and smell. Their preference ratings ranged from 80% to 100%. The fifth group, consisting mainly of fruit leather enriched with sunflower seeds and peanuts, received the second-highest scores for color, taste, and smell. The preference scores for this group varied between 60% and 80%. The preference ranges for plain, sesame, and almond fruit leathers were 20% to 40% in the third and sixth categories. The panelists provided scores similar to those of the first, second, and seventh groups, suggesting a slight preference for the fruit leather samples. Their preference scores varied between 0% and 20%. The PREMAP examination calculated the scores for coconut, sesame, almond, sunflower seed, peanut, and plain fruit leather. The preference map indicated that most panelists, ranging from 60% to 80%, favored color, taste, and smell. On the other hand, a minority of 20% to 40% of the panelists leaned towards appearance (Fig. 3A).

3.7. Principal Component Analysis (PCA)

The score plot (Fig. 4) visually represents the positioning of ML samples within a multivariate space defined by the first two principal components (PCs). The scores are distributed across four quadrants, highlighting distinct separations between the samples based on the specific physical and chemical attributes examined. Notably, the plot clearly differentiates between the plain and enriched MLs, with three distinct groups emerging. The red cluster represents the plain pestil, while the blue cluster includes peanut-added pestil, sunflower seed-added pestil, and almond-added pestil. The yellow cluster consists of sesame-added pestil and coconut-

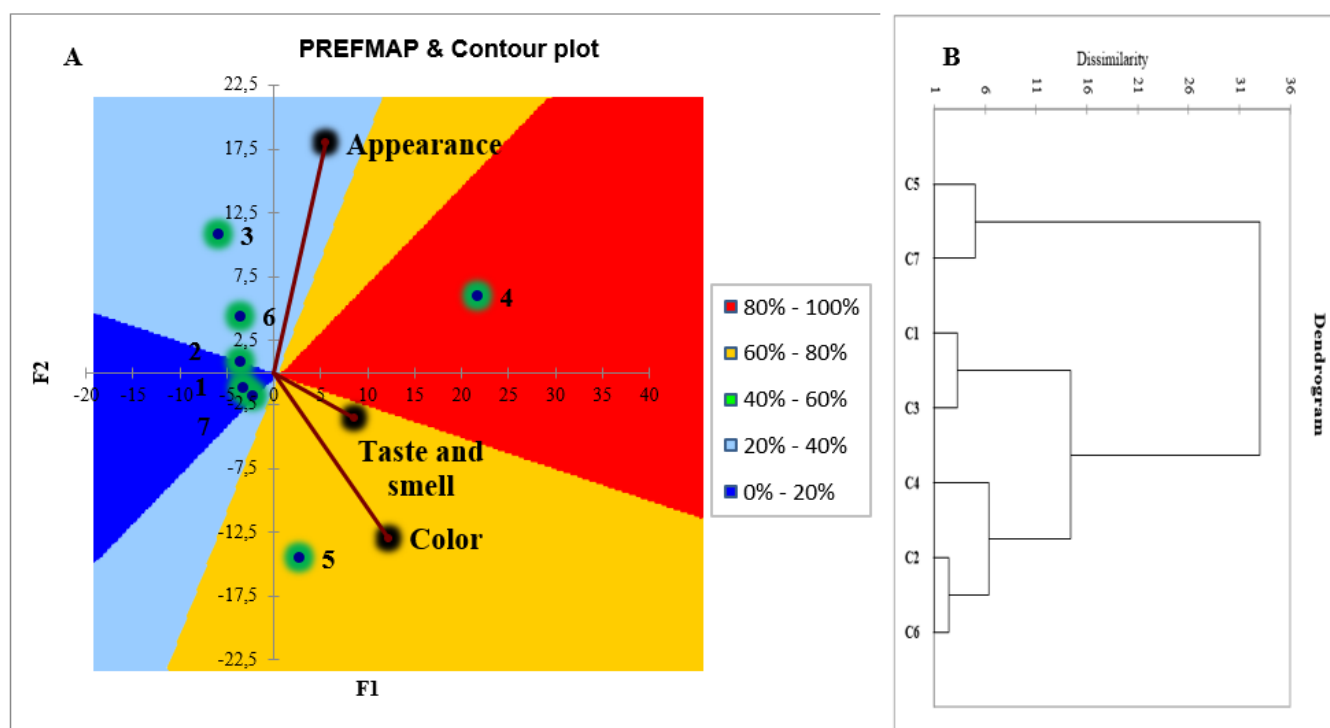


Figure 3. A) Preference mapping (PREMAP) B) Agglomerative hierarchical clustering (AHC) values of panelists

added pestil. Together, the first two principal components (F1 and F2) explain 89.06% of the variance in the data. The score plot (Fig. 4) and the data in Table 4 strongly support each other.

The ML samples may be classified into three categories according to the physicochemical and chemical analysis results. The first category comprises plain fruit leather, while sesame and coconut fruit leathers comprise the second category. The third category includes sunflower seeds, almonds, and peanuts. Within the first group, the plain ML sample in

the bottom left segment of the plot exhibits the highest levels of sucrose, carbohydrates, pH, protein, total solids, and HMF content while displaying lower levels in other analytical components. Using the PC1-PC2 plane to compare groups shows that the second group (almond, peanut, and sunflower seed-added MLs) has higher energy, total fat, glucose, and thickness. The third ML group (coconut and sesame-added) showcases elevated levels of cellulose, total ash, total sugar, moisture, insoluble ash in HCl, acidity, and fructose based on the PC1-PC2 axis.

Table 6. Mineral analysis results of plain and condiment added MLs

	Plain ML	Almond-added ML	Sunflower Seed-added ML	Peanut-added ML	Sesame-added ML	Coconut-added ML
Na	700.79±15.37 ^b	630.12 ±13.68 ^{bc}	686.37±18.96 ^b	467.82±11.73 ^c	886.9±12.64 ^a	952.34±13.18 ^a
Mg	415.01±16.05 ^c	700.58±17.24 ^b	997.37±19.92 ^a	606.82±10.73 ^{bc}	738.53±15.16 ^{ab}	773.69±16.41 ^{ab}
Al	58.15±3.99 ^a	52.09±9.09 ^{ab}	22.41±1.36 ^{bc}	38.67 ±8.03 ^{abc}	42.98±5.63 ^{abc}	16.70±1.41 ^c
Ca	888.04±4.97 ^c	1277.95±12.32 ^b	1350.17±12.25 ^b	1425.16±25.65 ^b	1515.01±12.82 ^{ab}	1815.19±10.24 ^a
K	2127.72±14.97 ^b	2745.34±11.31 ^a	2774.07±15.78 ^a	2378.32±16.19 ^{ab}	2121.29±17.09 ^b	2526.59±16.61 ^{ab}
Cr	1.75±0.43 ^b	4.58±1.84 ^a	2.18±0.73 ^b	2.03±1.11 ^b	2.04±0.13 ^b	1.50±0.27 ^b
Mn	54.15±3.88 ^c	74.19±4.46 ^{ab}	90.81±7.99 ^a	75.75±13.61 ^{ab}	82.58±1.23 ^{ab}	69.68±10.46 ^{bc}
Fe	195.84±22.53 ^a	304.53±52.23 ^a	283.27±14.62 ^a	273.97±129.88 ^a	349.45±175.44 ^a	258.82±6.23 ^a
Co	0.24±0.03 ^b	0.28±0.02 ^b	0.33±0.04 ^b	0.27±0.04 ^b	0.53±0.07 ^a	0.61±0.12 ^a
Ni	55.05±2.64 ^a	23.00±3.21 ^b	21.34±2.92 ^b	15.60±4.26 ^b	18.49±2.38 ^b	29.28±4.97 ^b
Cu	11.77±0.33 ^c	20.15±4.42 ^{bc}	50.61±8.41 ^a	18.14±1.65 ^{bc}	29.52±3.75 ^b	33.10±6.97 ^b
Zn	284.17±11.82 ^b	534.39±15.35 ^a	390.93±15.71 ^{ab}	395.16±12.31 ^{ab}	350.23±14.01 ^b	276.94±9.79 ^b
As	<LOQ	<LOQ	<LOQ	<LOQ	<LOQ	<LOQ
Pd	<LOQ	<LOQ	<LOQ	<LOQ	<LOQ	<LOQ
Ag	1.16±0.08 ^b	1.33±0.03 ^b	1.14±0.06 ^b	1.60±0.17 ^a	1.13±0.14 ^b	1.10±0.05 ^b
Cd	<LOQ	<LOQ	<LOQ	<LOQ	<LOQ	<LOQ
Sn	0.16±0.02 ^a	0.17±0.02 ^a	0.14±0.01 ^a	0.14±0.03 ^a	0.13±0.01 ^a	0.14±0.01 ^a
Ba	15.63±3.56 ^b	34.18±6.59 ^a	15.33±3.82 ^b	19.81±1.81 ^b	12.13±2.04 ^b	14.12±0.18 ^b
Hg	<LOQ	<LOQ	<LOQ	<LOQ	<LOQ	<LOQ
Pb	<LOQ	<LOQ	<LOQ	<LOQ	<LOQ	<LOQ
P	250.78±4.97 ^e	295.54±6.05 ^d	351.48±11.19 ^a	327.05±11.17 ^b	320.50±11.11 ^c	320.52±12.30 ^c

Results are presented as means ± standard deviations. Results of minerals were expressed as mg/kg. Different letters (a-f) in the same lines are significantly different (p<0.05). LOQ=0.01 mg/kg

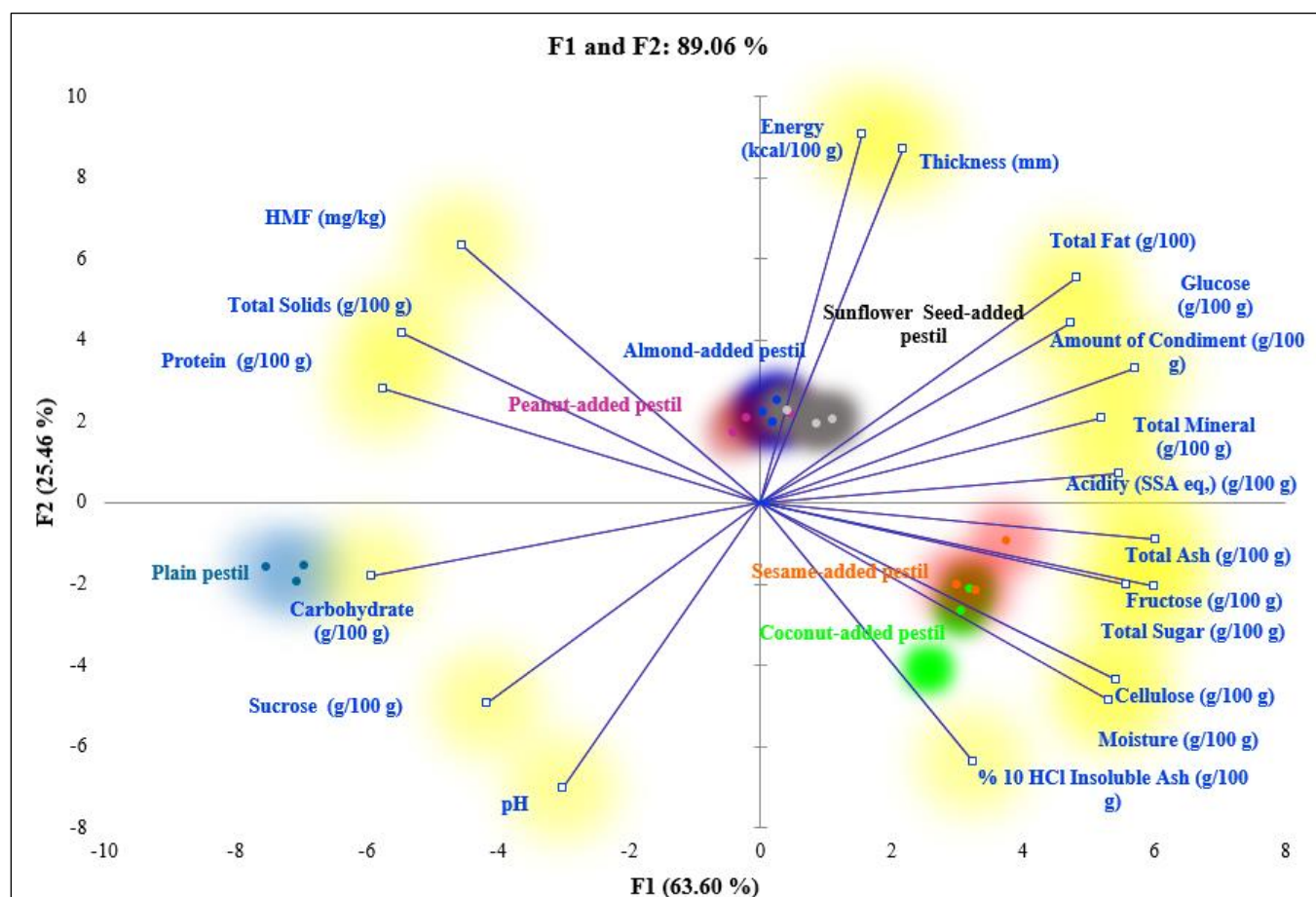


Figure 4. PCA analysis of physicochemical and chemical properties of the MLs. PC1 explains 63.60%, versus PC2 explains 25.46%

Fig. 4 illustrates positive correlations between variables situated close to each other and negative correlations between variables 180° apart. Furthermore, variables positioned 90° apart exhibit no significant correlation, suggesting their independence from each other [35]. The correlation matrix in Table 4 supports this correlation pattern.

In Fig. 4, 16 principal components, excluding carbohydrates, sucrose, and pH, correlate positively with at least one of the two principal components (Table 4). Table 5 depicts the rotated loadings and communality for each element. Factor F1 (total mineral, total fat, cellulose, total sugar, glucose, fructose, total ash), both sesame-added pestil and coconut-added pestil exhibit high positive scores in F1, which indicates that these pestils are characterized by higher levels of total minerals, total fat, cellulose, total sugar, glucose, fructose, and total ash. The loadings table confirms this, as these components have strong positive loadings under F1, suggesting that F1 captures a group of nutrients that are more abundant in these pestils. In contrast, plain pestil has a highly negative score in F1, indicating that it contains lower levels of these components.

Factor F2 (amount of condiment, acidity, pH), almond-added pestil and peanut-added pestil show high positive scores in F2, which reflects their higher

content of condiments and a specific pH range. This suggests that these pestils are richer in flavor-enhancing ingredients, influencing both their taste and acidity. The loadings table supports this, as amount of condiment and pH are positively correlated with F2. Therefore, pestils with higher F2 scores have more condiments and a more distinct pH level. On the other hand, sesame-added pestil and coconut-added pestil, with more negative scores in F2, likely contain fewer condiments compared to the other pestil types.

Factor F3 (protein, sucrose, HMF), almond-added pestil has a notably negative score in F3, which is associated with lower levels of protein and sucrose. This suggests that almond-added pestil contains less of these nutrients compared to other pestils. In contrast, peanut-added pestil and sunflower seed-added pestil show moderate positive scores in F3, indicating that they have higher levels of protein and sucrose.

Factor F4 (moisture, pH), sunflower seed-added pestil stands out with the highest positive score in F4, suggesting it has higher moisture levels and a particular pH that distinguishes it from the other pestil types. Peanut-added pestil and sesame-added pestil show more moderate scores in F4, implying they have a more balanced combination of moisture content and pH.

Factor F5 (Acidity, % 10 HCl insol. ash), while factor F5 appears to have a less significant influence overall, it

still reveals some interesting characteristics. For example, almond-added pestil has a relatively higher score in F5, suggesting it has a slightly different acidity or mineral content compared to the other pestils, which may influence its overall flavor and composition.

4. Conclusion

This study has revealed the feasibility of crafting MLs incorporated with alternative condiments. The ML samples generated three groups according to the physicochemical and chemical attributes. Strong correlations among the studied parameters were observed through multivariate statistical methods. The enriched MLs could serve as good sources of vital nutrients and energy. Significantly, the MLs developed also boast a notable mineral composition. The enriched MLs can contribute to the daily intake of required nutrients and energy as snacks or meals. The peanut-added ML may offer superiority over samples because of its lower sodium content. Sensory assessments have underscored the market potential of certain ML types if they are produced on an industrial scale. Consequently, this study has yielded products endowed with fresh taste and aromatic attributes. Based on our findings, the possibility of commercially producing ML types featuring flavors like sesame, coconut, and peanut is a viable prospect.

Based on the findings of this study, we recommend the commercial production and marketing of enriched ML products, especially those incorporating flavors like sesame, coconut, and peanut. These products not only show great promise in terms of their nutritional value and mineral composition, but they also have sensory attributes that are appealing to consumers. The development of MLs with added ingredients offers a significant potential to meet dietary needs, providing essential nutrients and energy in a convenient form, and making them suitable as snacks or meals. In conclusion, the sensory appeal, and enriched nutrient profile position these MLs as a promising product for commercial production. With the right marketing strategies focusing on their health benefits, convenience, and unique flavors, these products could successfully enter the market and meet growing consumer demand for nutritious, convenient snack and meal alternatives.

Funding

Supported by The GUBAP (Gümüşhane University Scientific Research Project Unit), Gümüşhane, Türkiye (Project No. GUBAP 16.A0110.02.01).

Data availability

The data that support the findings of this study are available from the corresponding author upon reasonable request.

Declarations

Conflict of Interest: The authors have declared no conflict of interest.

References

- [1] O. Sarma, M. Kundlia, H. Chutia, C.L. Mahanta, Processing of encapsulated flaxseed oil-rich banana-based (Dwarf cavendish) functional fruit leather, *J Food Process Eng*, 46, 2023, 14282.
- [2] M. Barman, A.B. Das, L.S. Badwaik, Effect of xanthan gum, guar gum, and pectin on physicochemical, color, textural, sensory, and drying characteristics of kiwi fruit leather, *J Food Process Preserv*, 45, 2021, e15478.
- [3] P. Sharma, M. Ramchiary, D. Samyor, A.B. Das, Study on the phytochemical properties of pineapple fruit leather processed by extrusion cooking, *LWT*, 72, 2016, 534–543.
- [4] A. Das, B.N. Bora, H. Chutia, C.L. Mahanta, Processing of minerals and anthocyanins-rich mixed-fruit leather from banana (*Musa acuminata*) and sohiong (*Prunus nepalensis*), *J Food Process Preserv*, 45, 2021, e15718.
- [5] L.M. Diamante, S. Li, Q. Xu, J. Busch, Effects of Apple Juice Concentrate, Blackcurrant Concentrate and Pectin Levels on Selected Qualities of Apple-Blackcurrant Fruit Leather, *Foods*, 2, 2013, 430–443.
- [6] A. Maskan, S. Kaya, M. Maskan, Hot air and sun drying of grape leather (pestil), *J Food Eng*, 54, 2002, 81–88.
- [7] R. da Silva Simão, J. Moraes, B. Carciofi, J. Laurindo, Recent Advances in the Production of Fruit Leathers, *Food Eng Rev*, 12, 2020, 68–82.
- [8] H. Zhang, Z.F. Ma, X. Luo, X. Li, Effects of Mulberry Fruit (*Morus alba* L.) Consumption on Health Outcomes: A Mini-Review, *Antioxidants*, 7, 2018, 69.
- [9] O. Yildiz, Physico-chemical and sensory properties of mulberry products: Gümüşhane pestil and köme, *Turk J Agric For*, 37, 2013, 762–771.
- [10] F. Yuksel, B. Yavuz, C. Baltaci, Some physicochemical, color, bioactive and sensory properties of a pestil enriched with wheat, corn and potato flours: An optimization study based on simplex lattice mixture design, *Int J Gastron Food Sci*, 28, 2022, 100513.
- [11] T. Mphaphuli, V.E. Manhivi, R. Slabbert, Y. Sultanbawa, D. Sivakumar, Enrichment of Mango Fruit Leathers with Natal Plum (*Carissa macrocarpa*) Improves Their Phytochemical Content and Antioxidant Properties, *Foods*, 9, 2020, 431.
- [12] TSI 1125, Fruit and vegetable products- Determination of titratable acidity with a potentiometric reference method, Turkish Standard Institute, ISO 750, 2002.
- [13] TSI 1728, Fruit and vegetable products-Determination of pH, Turkish Standard Institute, ISO 1842 (2001).
- [14] S.Y. Quek, N.K. Chok, P. Swedlund, The physicochemical properties of spray-dried watermelon powders, *Chem Eng Process*, 46, 2007, 386–392.
- [15] TSI 9131, Cezeriye (Turkish Special Carrot Sweet), Turkish Standard Institute, 1991.
- [16] TSI 12677, Spread dried mulberry, Turkish Standard Institute, 2000.
- [17] TSI 1562, Tea-determination of moisture content, Turkish Standard Institute, 1990.

- [18] TSI 1620, Macaroni, Turkish Standard Institute, 2016.
- [19] TSI 6180, Starches, native or modified, Determination of total fat content, Turkish Standard Institute, EN ISO 3947, 1997.
- [20] TSI 6932, Agricultural Food Products-Determination of Crude Fibre Content-General Method, Turkish Standard Institute, 1989.
- [21] TSI 1566, Tea- Determination of acid-insoluble ash, Turk Stand Institute, ISO 1577, 2001.
- [22] TSI 2131, Spices and condiment- Determination of total ash, Turkish Standard Institute, ISO 928, 2001.
- [23] NMKL 161, Determination by atomic absorption spectrophotometry after wet digestion in a microwave oven, NordVal International c/o Institute of Marine Research P.O. box 1870 Nordnes 5817 Bergen, Norway, 1998.
- [24] C. Baltacı, Z. Akşit, Validation of HPLC Method for the Determination of 5-hydroxymethylfurfural in Pestil, Köme, Jam, Marmalade and Pekmez, Hittite J Sci Eng, 3, 2016, 91–97.
- [25] O. Yildiz, G. Boyraci, Production and Some Quality Parameters of Sugar Beet Sweets (Pestil and Köme), Sugar Tech, 22, 2020, 842–852.
- [26] M. Karaoğlu, Y. Bedir, H. Boz, Effect of whole grain flours on the overall quality characteristics of mulberry pestil, Qual Assur Saf Crops Foods, 12, 2020, 67–75.
- [27] I. Tontul, A. Topuz, Effects of different drying methods on the physicochemical properties of pomegranate leather (pestil), LWT, 80, 2017, 294–303.
- [28] S. Suna, A. Özkan-Karabacak, Investigation of drying kinetics and physicochemical properties of mulberry leather (pestil) dried with different methods, J Food Process Preserv, 43, 2019, e14051.
- [29] H. Boz, M.M. Karaoğlu, G. Kaban, The effects of cooking time and sugar on total phenols, hydroxymethylfurfural and acrylamide content of mulberry leather (pestil), Qual Assur Saf Crops Foods, 8, 2015, 493–500.
- [30] O. Cagindi, S. Otles, Comparison of some properties on the different types of pestil: a traditional product in Türkiye, Int J Food Sci Technol, 40, 2005, 897–901.
- [31] H. Ulusal Bayram, Determine production methods and quality parameters of Gümüşhane pestil and Kome, Master Thesis, KTU Graduate School of Natural and Applied Sciences, Trabzon, Türkiye, 2018.
- [32] M. Zappalà, B. Fallico, E. Arena, A. Verzera, Methods for the determination of HMF in honey: a comparison, Food Control, 16, 2005, 273–277.
- [33] C. Baltacı, H. Ilyasoglu, A. Gundogdu, O. Ucuncu, Investigation of Hydroxymethylfurfural Formation in Herle, Int J Food Prop, 19, 2016, 2761–2768.
- [34] N. Cayot, Sensory quality of traditional foods, Food Chem, 101, 2007, 154–162.
- [35] S. Kopuzlu, A. Önenç, O. Bilgin, N. Esenbuga, Determination of meat quality through principal components analysis, J Anim Plant Sci, 21, 2011, 151–156.



Highly efficient hexavalent chromium removal using *nano*-Fe₃O₄/pomegranate peel biochar/alginate composite as an advanced biosorbent*

Şerife Parlayıcı , Erol Pehlivan** 

Konya Technical University, Faculty of Engineering and Natural Science, Department of Chemical Engineering, 42250, Selçuklu- Konya, Türkiye

Abstract

In this study, a novel composite – *nano*-Fe₃O₄/pomegranate peel biochar/alginate hydrogel beads (*n*Fe₃O₄-PPBC/Alg) – was synthesized as an alternative adsorbent for removing Cr(VI) ions from aqueous solutions. The adsorbent material was characterized using FT-IR analysis and scanning electron microscopy (SEM). Cr(VI) removal efficiencies were calculated using the standard batch adsorption method to determine the optimal pH, adsorbent dose, contact time, and initial concentration. Various adsorption isotherms, such as Freundlich, Langmuir, and Dubinin–Radushkevich, were employed to describe the adsorption behavior at equilibrium. The Langmuir adsorption isotherm was found to be the most suitable to describe the observed adsorption phenomena, and the adsorption capacity of *n*Fe₃O₄-PPBC/Alg for Cr(VI) was determined to be 316.25 mg/g by the Scatchard linearization method. To investigate the adsorption processes on the *n*Fe₃O₄-PPBC/Alg, kinetic models, including pseudo-first order and pseudo-second-order models, were applied. The pseudo-second-order kinetic model provided the best fit to the experimental data. The adsorption capacity of pomegranate peel biochar for removing Cr(VI) ions has not been previously enhanced by encapsulating it in an alginate matrix and simultaneously magnetizing it. In this context, this study makes a significant contribution to the existing literature. This research demonstrated that *n*Fe₃O₄-PPBC/Alg is an effective adsorbent for the removal of Cr(VI) from aqueous solutions.

Keywords: Alginate; biochar; Cr(VI); kinetics; *nano*-Fe₃O₄; pomegranate peel

1. Introduction

Although heavy metals are naturally present in the Earth's crust, their concentrations in the environment can become hazardous due to both natural and human-induced processes. Human activities such as mining, agriculture, urbanization, industrial operations, and improper waste disposal are the primary drivers of environmental contamination. These activities significantly accelerate the release and distribution of heavy metals, leading to elevated levels in water which threaten ecological systems and human health. Key industrial sources for the heavy metals include metal processing in refineries, leather tanning, coal combustion in power plants, petroleum combustion in nuclear power facilities, as well as production in plastics, textiles, and microelectronics manufacturing [1]. Chromium is frequently present in industrial wastewater, especially from industries such as catalyst production, electroplating, dye and pigment manufacturing, leather tanning, ceramics, glass production, wood preservation, cooling tower water treatment, corrosion prevention, and alloy

manufacturing [2]. The extensive industrial application of chromium has a significant downside: environmental pollution [3,4].

Hexavalent chromium, Cr(VI), is a dangerous and cancer-causing contaminant that presents serious threats to human health and the environment. Many natural water bodies have been contaminated with Cr(VI), a compound known to cause teratogenic, mutagenic, carcinogenic effects, and damage to multiple organs upon human exposure. Consequently, developing an effective and holistic approach for the degradation of Cr(VI) has become crucial, as its high solubility in water and environmental persistence make it a significant global concern. Chromium mainly exists in two forms: Cr(III) and Cr(VI), with Cr(VI) being 100 times more toxic than Cr(III) in aqueous environments. Cr(VI) is primarily present as Cr₂O₇²⁻, CrO₄²⁻, HCrO₄⁻ in water [5].

These anions exhibit strong oxidative and migratory properties, posing significant environmental and health risks.

Citation: Ş. Parlayıcı, E. Pehlivan, Highly efficient hexavalent chromium removal using *nano*-Fe₃O₄/pomegranate peel biochar/alginate composite as an advanced biosorbent, Turk J Anal Chem, 7(1), 2025, 22–32.

****Author of correspondence**

Tel: +90 (332) 205 18 45

Received: December 4, 2024

doi <https://doi.org/10.51435/turkjac.1595052>

erolpehlivan@gmail.com

Fax: N/A

Accepted: January 19, 2025

*This paper was presented at the 6th International Environmental Chemistry Congress, EnviroChem 05-08 November 2024, Trabzon Türkiye.

Various methods are available to reduce Cr(VI) concentrations in water bodies, including adsorption [6,7], electrochemical techniques [8], membrane treatments [9], bioremediation [10], chemical precipitation, ion exchange, and reverse osmosis are often expensive, complicated, and ineffective, particularly at low concentrations.

Therefore, there is a pressing need for more cost-effective, eco-friendly, and efficient solutions. Adsorption is favored for its simplicity and broad applicability, making it a competitive technology for addressing heavy metal pollution in water. Various adsorbents, including biopolymer composite [11], activated carbon [12], biochar [13], and modified chitosan [14], have been explored for Cr(VI) removal. Nevertheless, there remains a demand for adsorbents that are more sustainable, environmentally friendly, and cost-effective.

Common adsorbents like biochar, activated carbon, graphene, clays, carbon nanotubes, and organic frameworks are typically nanoscale powders, often modified with metallic or organic materials. However, there remains a need to develop suitable embedding materials to immobilize these nanomaterials within appropriate matrices effectively. Among these materials, activated carbon stands out as the most suitable adsorbent due to its high surface area and excellent adsorption capacity. However, the high cost of commercial activated carbon has driven the search for more affordable alternatives with comparable properties. Among the materials studied, biochar has emerged as one of the most environmentally friendly and functional options. Biochar differs significantly from activated carbon. Its production involves lower temperatures compared to those used for activated carbon. In the case of activated carbon, the biomass undergoes significant carbonization, losing most of its functional groups. To enhance the carbonized surface and increase porosity, it is further treated with steam or chemicals. In contrast, biochar production does not require such treatments. The biomass is carbonized at lower temperatures, preserving its functional groups or even activating them, making biochar a versatile material for various applications.

Biochar has recently gained considerable attention as an effective adsorbent due to its large specific surface area (SSA), abundance of functional groups (FGs), and complex pore structures [15]. Biochar, a carbon-rich material created through the pyrolysis of biomass, has emerged as an affordable, environmentally friendly solution for wastewater contaminant removal [11]. Its appeal lies in its high surface area, rich functional groups, and sustainable production process. However, its slow adsorption kinetics and limited adsorption

capacity underscore the need for composite materials with enhanced properties. HCrO_4^- ions can be adsorbed onto the COOH , and OH surface groups of biochar, where they form hydrogen bonds and undergo redox reactions with phenolic compounds. This process facilitates the reduction of Cr(VI) to Cr(III), which is then immobilized in situ on the adsorbent surface.

Numerous studies have previously focused on modifying biochar with nanomaterials or metal nano-oxides [16]. Among these, nano-zero valent iron ($n\text{ZVI}$) stands out for its advantageous properties, including low cost, high specific surface area, excellent reducibility, strong reactivity, and nano-scale particle size. Consequently, there is a growing body of research employing $n\text{ZVI}$ -modified biochar for the remediation of heavy metals and organic pollutants in the environment. This research involves a novel and effective strategy that combines alginate and Fe_3O_4 nanoparticles with biochar derived from pomegranate peel. The $n\text{Fe}_3\text{O}_4$ -PPBC/Alg is a new composite that combines the biocompatibility of alginate, the adsorption capabilities of biochar made from pomegranate peel, and the magnetic properties of Fe_3O_4 nanoparticles. This composite efficiently adsorbs and removes Cr(VI), addressing environmental issues including water pollution. Its cost-effectiveness is increased by its magnetic qualities, which make recovery and reuse simple.

Alginate (Alg) is an inexpensive and easily produced biomaterial rich in carboxyl groups. Alg is a commonly used natural linear anionic polysaccharide, mainly composed of β -1,4-glycosidic linkages between α -L-mannuronic acid and β -D-guluronic acid. It is highly biocompatible, biodegradable, and capable of forming gels of various sizes and shapes through cross-linking with divalent or trivalent metal ions [17]. Alg, a natural polysaccharide extracted from brown algae, is highly regarded for its exceptional gel-forming properties and strong metal ion-binding capabilities. Its biocompatibility, biodegradability, and versatile gel-forming characteristics have made it a popular choice in numerous applications [15]. Because alg has both hydrophilic and hydrophobic groups, it can hold onto a large amount of bound water while being prepared, creating free diffusion routes for molecules that are soluble in water. Alg is a useful substance for treating heavy metal ions because of this characteristic, which permits contaminants to enter the gel's interior. When incorporated into biochar composites, Alg improves adsorption capacity by offering additional binding sites on the composite [18,19].

Expanding on these ideas, Alg and biochar were thoroughly mixed and introduced into a $n\text{Fe}_3\text{O}_4$ solution, forming a $n\text{Fe}_3\text{O}_4$ -PPBC/Alg composite gel. $n\text{Fe}_3\text{O}_4$ is highly prone to oxidation and loss, making it

challenging to directly use nano-iron/carbon composite materials [20]. Anaerobic or protective nano-iron can be applied to solve this issue, such as in groundwater environments, beneath an FeS layer, or incorporated into polymers like alginate, chitosan, or polyaniline. Alg, known for its excellent stability and high mechanical strength, is a well-established coating material [21].

This study introduces $n\text{Fe}_3\text{O}_4\text{-PPBC/Alg}$, a highly effective composite material for enhancing the adsorption of Cr(VI) from aqueous solutions. Using biomass waste as a raw material to produce biochar adsorbents is crucial for reducing the cost of adsorbents. Biochar is favored for its high specific surface area and porosity, which provide abundant adsorption sites. However, most biochars are in powder form, which presents challenges in usage, particularly with complex recovery processes. Magnetic metal oxides such as Fe_3O_4 have become increasingly popular in recent years. When nano Fe_3O_4 is incorporated into the adsorbent structure, the composite can be easily separated from the solution medium using an external magnetic field. On the other hand, nano Fe_3O_4 particles often require combinations with other materials to mitigate issues related to their limited adsorption capacity, powder accumulation, and to enhance their adsorption properties. In light of these factors, $n\text{Fe}_3\text{O}_4\text{-PPBC/Alg}$ was synthesized.

By leveraging the binding properties of Alg, the porous structure of pomegranate peel biochar, and the synergistic effects of Fe_3O_4 nanoparticles, the composite demonstrates significant potential for adsorption of Cr(VI) in prepared aqueous solutions. The research aims to investigate the factors influencing Cr(VI) adsorption onto $n\text{Fe}_3\text{O}_4\text{-PPBC/Alg}$, evaluate its adsorption performance using adsorption models, and uncover the underlying mechanisms through FT-IR, and SEM

analyses. The uniqueness of this study lies in the fact that Cr (VI) adsorption on $n\text{Fe}_3\text{O}_4\text{-PPBC/Alg}$ has not been reported in the literature. The use of pomegranate peels, derived from plant waste, converted into biochar and encapsulated in non-toxic biopolymers like alginate, presents several advantages over other adsorbents by eliminating the need for complex pre-treatment processes. Utilizing pomegranate peel waste as a raw material helps reduce the challenges associated with waste accumulation. Furthermore, the novelty of this study is emphasized by the use of renewable, low-cost materials, the simplicity of preparation and application, and the enhancement of the alginate gel adsorbent's performance without requiring active chemical processes. Additionally, the system simplifies the removal process by converting the adsorbents into a magnetic form, facilitating their separation from the aqueous medium.

The study evaluates adsorption capacity, kinetics, and Cr(VI) removal mechanisms, providing valuable insights into the composite's efficiency. This offers a cost-effective and promising solution for mitigating Cr(VI) pollution in wastewater, supporting environmental remediation and safeguarding aquatic ecosystems.

2. Material and method

2.1. Preparation of adsorbents

Pomegranates were sourced from a local market in Turkey. The peels and edible parts of the fruit were separated. The peels were washed with pure water and dried in an oven for 24 hours. The dried peels were then heated at 600 °C in a Magma THERM MT1210/B2 muffle furnace for 3 hours under low-oxygen conditions to produce biochar [22]. The biochar (PPBC) was cooled in

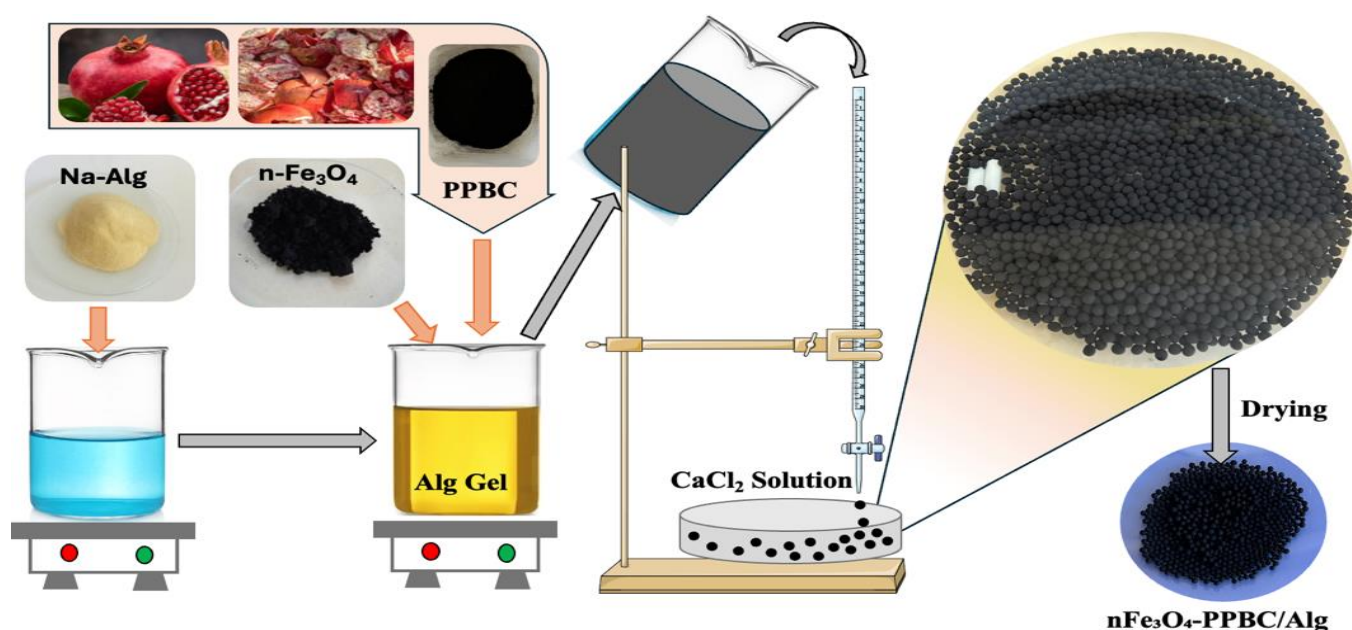


Figure 1. Synthesis scheme of $n\text{Fe}_3\text{O}_4\text{-PPBC/Alg}$ composite

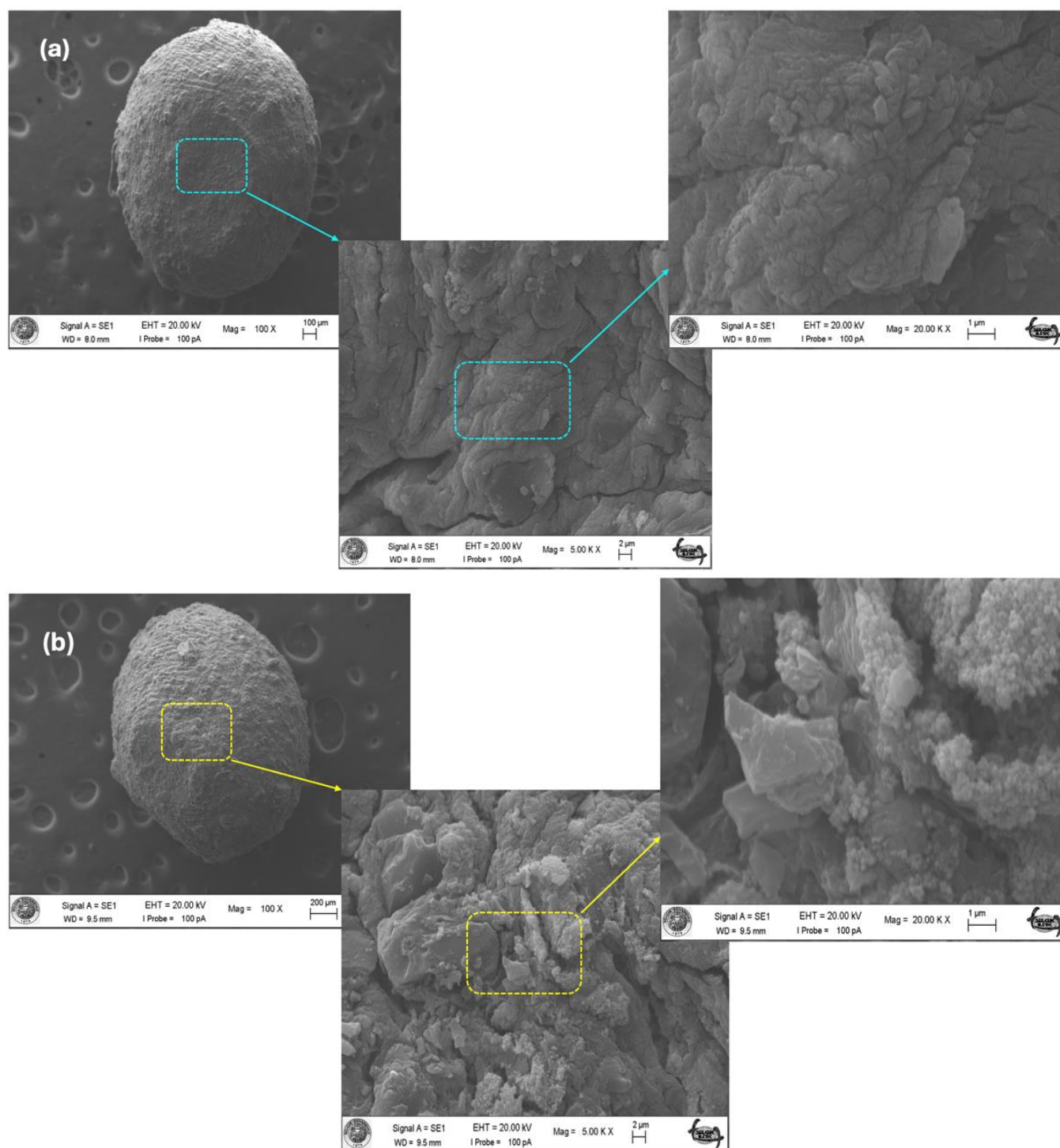


Figure 2. (a) SEM images of $n\text{Fe}_3\text{O}_4\text{-PPBC/Algae}$ composite and (b) after adsorption Cr(VI)

a desiccator, ground into a fine powder, and sieved to obtain particles with a size of 125 μm for use in composite preparation. To prepare $n\text{Fe}_3\text{O}_4\text{-PPBC/Alg}$, sodium alginate was first dissolved in 100 ml of distilled water (5% w/v). The solution was mixed with a magnetic stirrer for about 4 hours to create a homogeneous gel. Separately, two suspensions were prepared: one containing 2.5 g of *nano*- Fe_3O_4 in 20 ml of distilled water and another containing 2.5 g of PPBC in 20 ml of distilled water. Each suspension was stirred at 300 rpm for 2 hours to ensure proper dispersion. These suspensions were then added to the alginate gel and stirred with a

magnetic stirrer for 6 hours to form a uniform solution. The resulting mixture was introduced dropwise into a 0.5 M CaCl_2 solution using a syringe, forming spheres. These spheres (beads) were stirred in the solution at 100 rpm for approximately 3 hours. The beads were left in the solution overnight, then collected by filtration, washed with water until reaching a neutral pH, and dried at 60 $^\circ\text{C}$ for 24 hours (Fig. 1). This description details the step-by-step process of preparing the pomegranate peel biochar composite and its incorporation with alginate and iron oxide nanoparticles.

3. Results and discussion

3.1. Characterization of composite

The composite, $n\text{Fe}_3\text{O}_4\text{-PPBC/Alg}$, was characterized using FT-IR spectroscopy to identify its surface functional groups. Post-adsorption FT-IR analysis was also performed to verify the adsorption of Cr(VI) ions. Surface morphology was studied by capturing scanning electron microscopy (SEM) images of the composite both before and after the adsorption process.

3.2. SEM analysis of composite

Using SEM, the structural differences in $n\text{Fe}_3\text{O}_4\text{-PPBC/Alg}$ before and after Cr(VI) adsorption were observed. The SEM image in Fig. 2a reveals a rough surface before adsorption. In contrast, Fig. 2b shows the Cr(VI) ions forming deposits and accumulating over the surface pores, confirming their successful adsorption onto $n\text{Fe}_3\text{O}_4\text{-PPBC/Alg}$.

3.3. FT-IR spectrum of composite

The functional groups' types were analyzed using FT-IR spectroscopy. Fig. 3 presents the FT-IR spectra of $n\text{Fe}_3\text{O}_4\text{-PPBC/Alg}$ composite both before and after the adsorption process. From the spectrum, a broad peak around 3270 cm^{-1} indicates the stretching vibrations of O-H groups. The peak at 1590 cm^{-1} corresponds to the stretching vibrations of the carboxyl group ($-\text{C}=\text{O}$). A peak at 1420 cm^{-1} is attributed to the stretching vibrations of aromatic $\text{C}=\text{C}$ bonds. The band observed at 1016 cm^{-1} signifies the stretching of ether ($-\text{C}-\text{O}$) and alcohol ($-\text{C}-\text{O}$) groups. Additionally, the absorption band at 535 cm^{-1} , characteristic of Fe_3O_4 nanoparticles, is associated with the Fe-O bond's stretching vibrations.

The surface functional components of $n\text{Fe}_3\text{O}_4\text{-PPBC/Alg}$ after contact with Cr(VI) ions were determined by FT-IR spectrometry. The results are given in Fig. 3. After the removal of Cr(VI) from aqueous media using the $n\text{Fe}_3\text{O}_4\text{-PPBC/Alg}$ composite, the range of absorption peaks in the structure of the produced composite was changed, which could be due to the interaction of present functional groups in the structure of the composite with Cr(VI) ions.

3.4. Effect of solution pH on Cr(VI) adsorption

The pH of a solution plays a critical role in regulating the adsorption process. To examine how pH influences the adsorption of Cr(VI) ions by $n\text{Fe}_3\text{O}_4\text{-PPBC/Alg}$, the equilibrium concentrations were analyzed at pH levels ranging from 2 to 8, after a 60-minute equilibrium period. These findings are illustrated in Fig. 4. Generally, as the pH increases, the efficiency of Cr(VI) removal by $n\text{Fe}_3\text{O}_4\text{-PPBC/Alg}$ decreases.

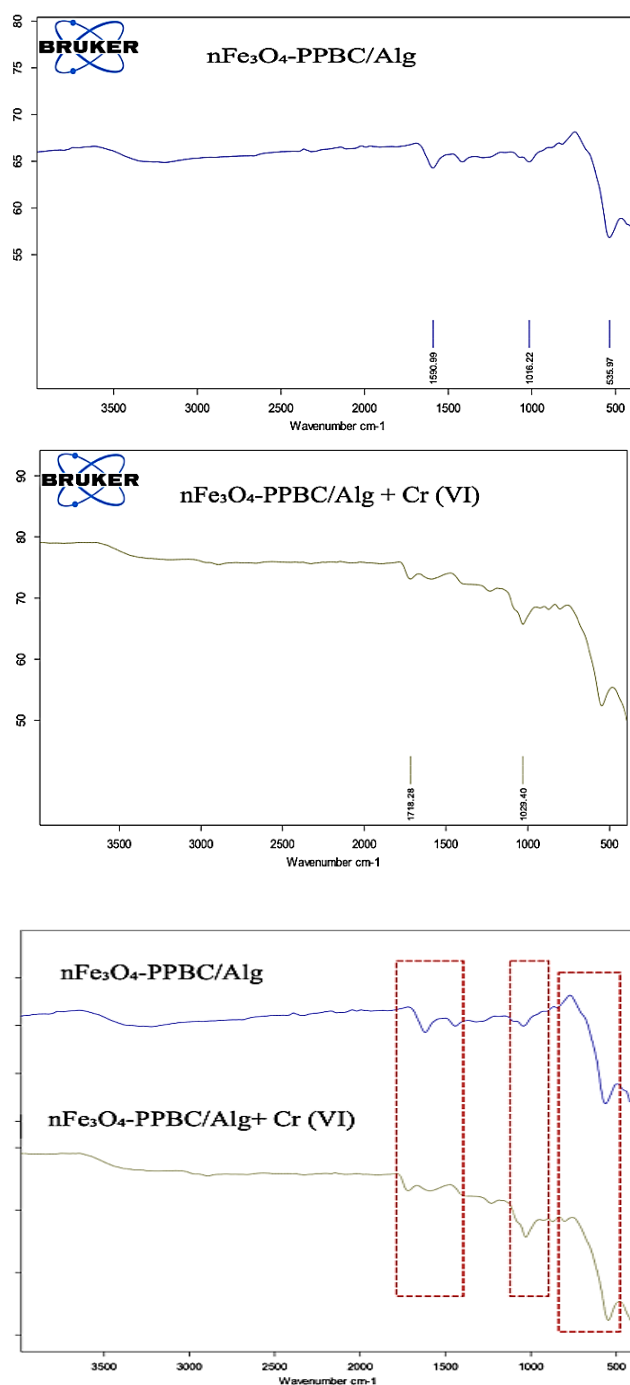


Figure 3. Pre- and post-adsorption FT-IR plot of $n\text{Fe}_3\text{O}_4\text{-PPBC/Alg}$ before and after adsorption

The highest adsorption occurs within the pH range of 2.0 to 3.0. At lower pH levels, the adsorbent surface acquires more positive charges, enhancing the electrostatic attraction for anionic Cr(VI) species [11]. At higher solution pH values, hydroxide ions ($-\text{OH}$) may compete with Cr(VI) for adsorption sites, reducing overall removal efficiency. Venkatrajan et al. reported similar findings, suggesting that the adsorption of Cr(VI) ions is predominantly driven by electrostatic interactions at lower pH levels [5]. The maximum chromium removal efficiency was observed when the adsorbent surface acquired a positive charge through protonation, facilitated by the higher concentration of H^+ ions in the medium.

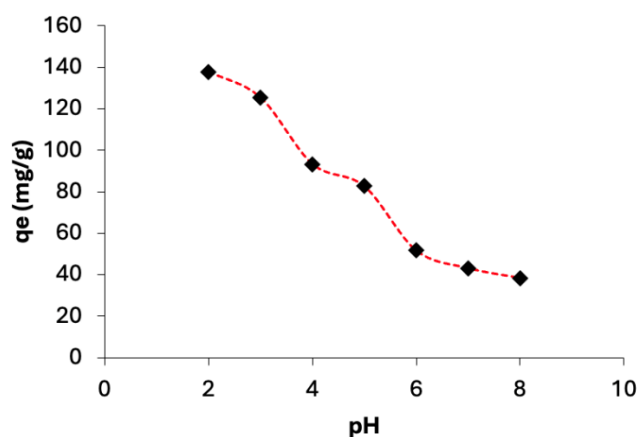


Figure 4. Effect of pH on Cr(VI) adsorption

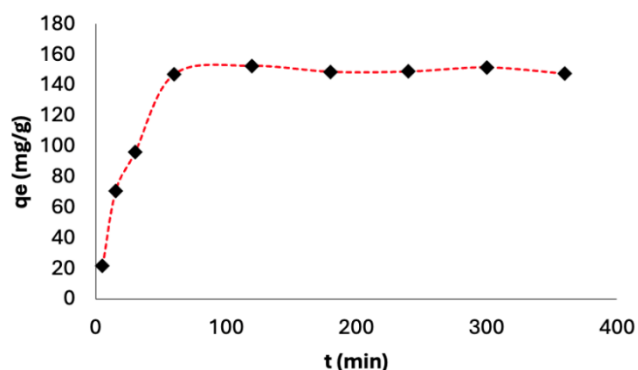


Figure 5. Effect of contact time on Cr(VI) adsorption

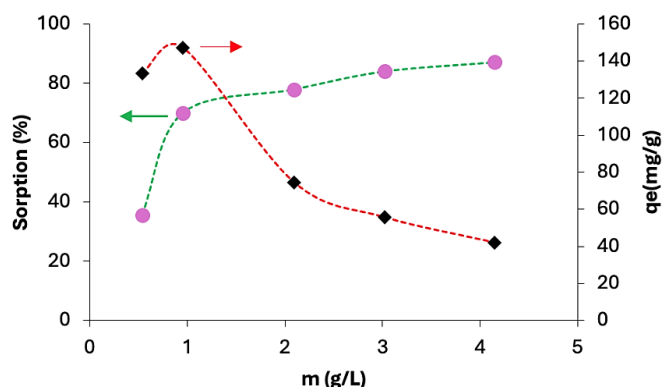


Figure 6. Effect of adsorbent dosage on Cr(VI) adsorption

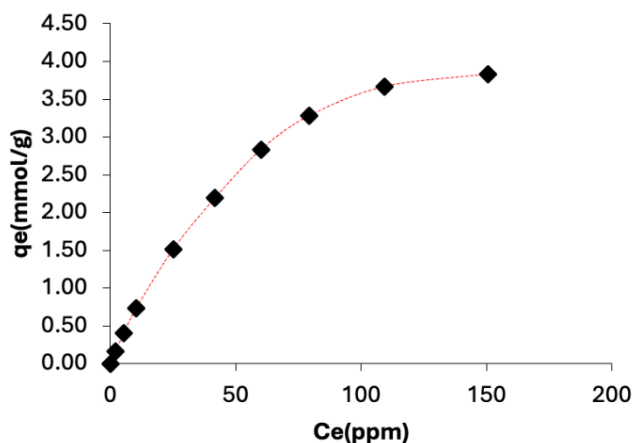


Figure 7. Effect of the initial Cr(VI) concentration on adsorption

3.5. Effect of contact time on adsorption of Cr (VI) ions

Contact time is a key factor in the adsorption process, with fast adsorption being a highly desirable trait. The impact of contact time on Cr(VI) adsorption was studied at intervals of 5, 15, 30, 60, 120, 180, 240, 300, and 360 minutes, using a composite dose of 1 g/L at pH 2 and a temperature of 25 °C. As illustrated in Fig. 5, the adsorption of Cr(VI) ions occurred rapidly as the contact time increased from 5 to 60 minutes, approaching equilibrium within this period. After 60 minutes, the adsorption rate slowed significantly with prolonged contact time. The equilibrium time is influenced by the type of adsorbent and the number of accessible active adsorption sites. The rapid adsorption efficiency of $\eta\text{Fe}_3\text{O}_4\text{-PPBC/Alg}$ makes it cost-effective for use in small-scale reactor systems. Based on these findings, a contact time of 60 minutes was chosen as the optimum for future experiments.

3.6. Effect of adsorbent dose

The influence of adsorbent dosage on Cr(VI) removal was assessed through experiments conducted with various dosages (0.5, 1.0, 2.0, 3.0, and 4.0 g/L). Fig. 6 illustrates the relationship between adsorbent amounts and both adsorption capacity and removal efficiency. In general, the adsorption capacity of Cr(VI) initially increases with higher adsorbent doses but decreases after reaching a peak. Similarly, the percentage of Cr(VI) removal rises with the dose but levels off beyond a certain point. A rapid increase in Cr(VI) adsorption was observed when the $\eta\text{Fe}_3\text{O}_4\text{-PPBC/Alg}$ dose was raised from 0.5 to 1.0 g/L. Beyond the 1 g/L dosage, adsorption reached a steady state, with only minor gains in efficiency. Adsorption capacity was found to increase proportionally with adsorbent dosage up to 1 g/L. Consequently, 1 g/L was identified as the optimal adsorbent dosage for further experiments.

3.7. Effect of the initial Cr(VI) concentration on adsorption

The initial concentration of Cr(VI) ions plays a crucial role as a driving force to counteract mass transfer resistances between the aqueous and solid phases. Higher removal efficiency results from the adsorbent's accessible active sites often capturing the majority of the Cr(VI) ions at lower starting concentrations. The adsorption rate decreases as the concentration rises because the active sites get saturated. Adsorption is stimulated by a larger concentration gradient, which is produced by higher starting concentrations. This may result in faster adsorption at first, but when adsorption sites are occupied, equilibrium is attained sooner. As the Cr(VI) concentration increases, the competition among

Cr(VI) ions for the limited adsorption sites becomes more intense, leading to a decline in the overall adsorption performance. Fig. 7 illustrates how the initial concentration affects adsorption. The adsorption capacity was measured across a range of initial Cr(VI) concentrations (10 to 350 ppm). Results indicated that adsorption capacity increased with higher Cr(VI) concentrations, up to a certain threshold. This enhancement in retention capacity with rising initial concentrations is likely due to the driving forces that help overcome the resistance encountered during the transfer of Cr(VI) ions from the solution to the $n\text{Fe}_3\text{O}_4$ -PPBC/Alg surface [23].

3.8. Adsorption isotherms

Adsorption isotherms illustrate the distribution of Cr(VI) ions between the liquid and solid phases once equilibrium is reached during the adsorption process [24]. Equilibrium data are crucial for analyzing and designing adsorption systems. The adsorption behavior of Cr(VI) on $n\text{Fe}_3\text{O}_4$ -PPBC/Alg was evaluated using widely recognized models, including the Langmuir, Freundlich, and Dubinin-Radushkevich (D-R) linearization methods to assess the composite's suitability. For the Langmuir model, two different linear

methods were used, namely the Hanes-Woof and Scatchard methods [25]. The experimental isotherms for Cr(VI) adsorption onto $n\text{Fe}_3\text{O}_4$ -PPBC/Alg are presented in Fig. 8.

Based on equilibrium data, adsorption isotherms were analyzed, and R^2 values were calculated. The Langmuir model demonstrated the best fit to the data, with a correlation coefficient of 0.990, indicating a monolayer adsorption process. Considering the linear regression values in Table 1, the Langmuir model was found to be more suitable for describing the adsorption of Cr(VI). Accordingly, the Langmuir adsorption capacity was determined as $Q_m=303.03 \text{ mg g}^{-1}$. The Langmuir isotherm model assumes that the adsorbent surfaces are homogeneous and form a single layer, with uniformly distributed and equivalent binding sites for Cr(VI) ions. This suggests that Cr(VI) ions are adsorbed onto $n\text{Fe}_3\text{O}_4$ -PPBC/Alg in a monolayer fashion. The separation factor (R_L) is a dimensionless constant derived from equilibrium parameters. If the R_L value lies between 0 and 1, the adsorption process is considered favorable for dye removal. For $n\text{Fe}_3\text{O}_4$ -PPBC/Alg, the R_L value was calculated to be 0.256, indicating that the adsorption of Cr(VI) ions onto this adsorbent is effective and suitable.

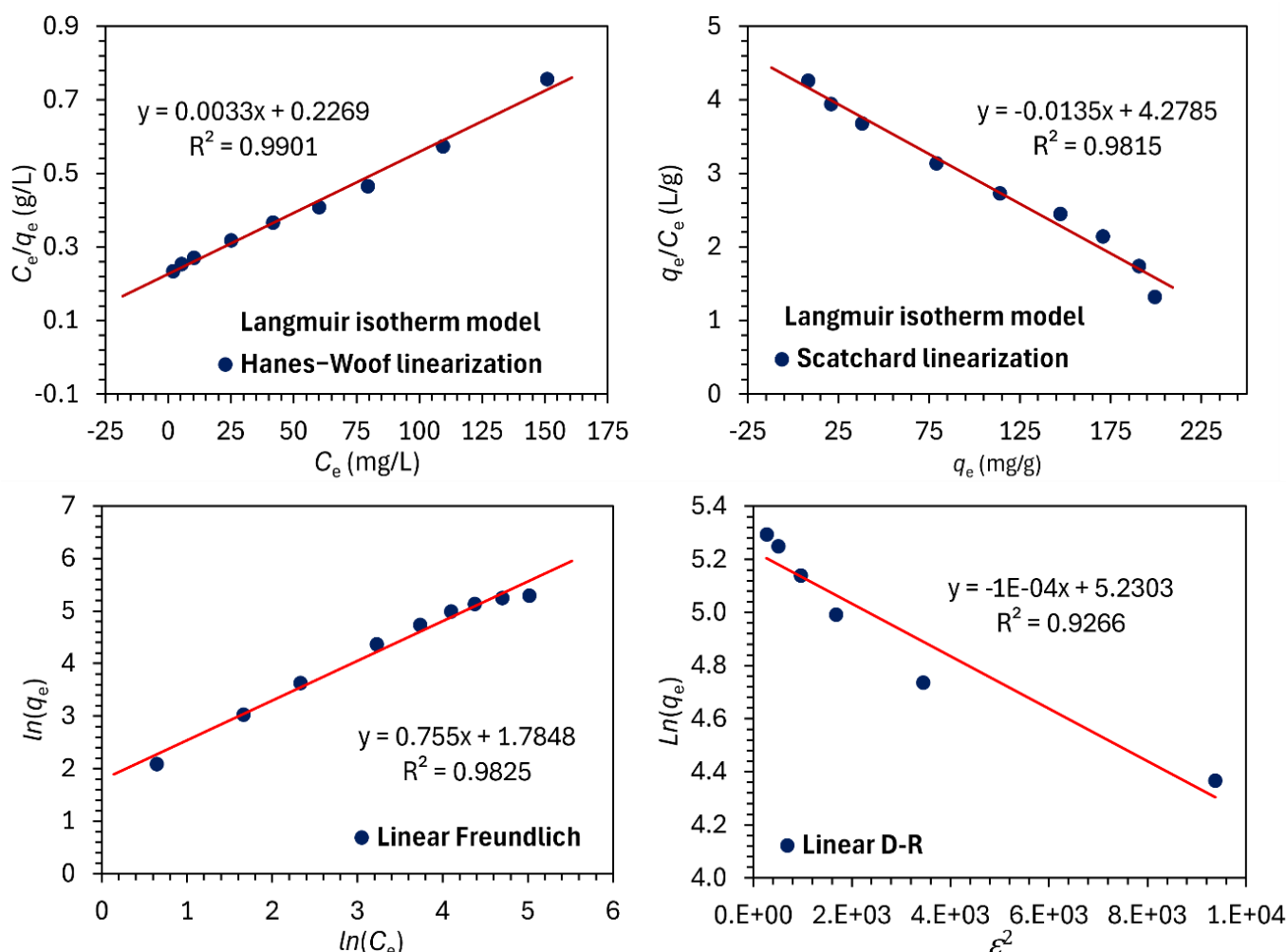


Figure 8. Langmuir (Hanes-Woof linearization), Langmuir (Scatchard linearization) Freundlich, and D-R isotherm graphs for $n\text{Fe}_3\text{O}_4$ -PPBC/Alg

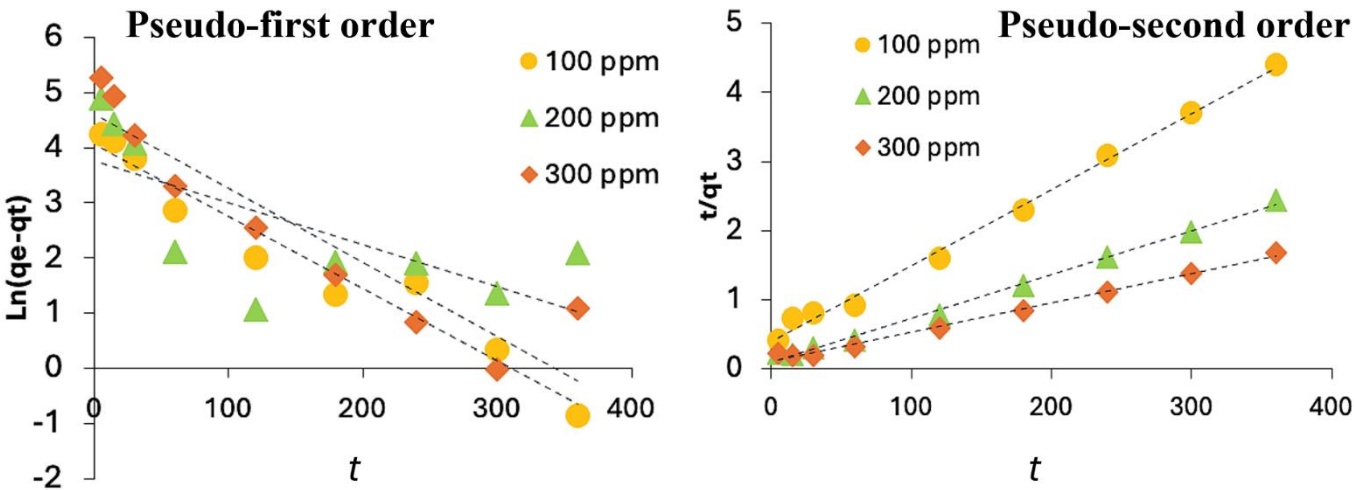


Figure 9. Plots of pseudo-first order and pseudo-second order kinetic models for Cr(VI) adsorption

The graph resulting from the application of the Freundlich equation to the data indicates that the adsorption of Cr(VI) does not follow this isotherm model (Fig. 8). The Freundlich isotherm is typically used for multilayer adsorption and assumes a heterogeneous surface where the heat of adsorption is distributed unevenly among the adsorbed molecules. The fact that the Cr(VI) adsorption by $n\text{Fe}_3\text{O}_4\text{-PPBC/Alg}$ does not align with the Freundlich model for single-layer adsorption further confirms this.

The Dubinin-Radushkevich (D-R) isotherm is widely used for systems where the adsorption curve is influenced by the sorbent's porous surface. This model helps identify whether the adsorption mechanism is physical or chemical. If the E value lies between 8 and 16 kJ/mol, the adsorption mechanism is considered chemical. E was calculated as 1.618 kJ/mol in this study, thus, it can be said that the Cr(VI) adsorption mechanism proceeds physically (Table 1). The Scatchard plot, a linearized representation of the Langmuir isotherm, offers additional confirmation regarding the heterogeneity of binding sites. A linear plot suggests the presence of only one type of binding site, indicating homogeneity, whereas deviation from linearity implies heterogeneity. The R^2 value of 0.9815 demonstrates strong linearity, confirming the homogeneous nature of the surface and supporting the conclusion that the

Langmuir model is the most suitable for describing the adsorption mechanism [25].

Additionally, the values obtained through Scatchard analysis align with the Langmuir isotherm, suggesting that the Langmuir adsorption isotherm is more appropriate for the process.

3.9. Adsorption kinetic modeling

The adsorption kinetics of Cr(VI) ions were analyzed using data fitted to pseudo-first order and pseudo-second order kinetic models (Fig. 9). The pseudo-second order model provided an excellent fit to the experimental data. A comparison between the experimental adsorption capacities and the theoretical values predicted by the two models is shown in Table 2. The theoretical q_e values from the first-order kinetic model deviated significantly from the experimental values, and the correlation coefficients were lower. This suggests that the first-order kinetic model does not adequately describe the adsorption of Cr(VI) by $n\text{Fe}_3\text{O}_4\text{-PPBC/Alg}$. On the other hand, the correlation coefficients for the linear plots of t/q_t versus t in the second-order model were very close to 1. The theoretical q_e values in the second-order model were also very close to the experimental values, indicating that the second-order model fits the adsorption of Cr(VI) ions by $n\text{Fe}_3\text{O}_4\text{-PPBC/Alg}$ quite well.

Table 1. Values of isotherm parameters for Cr(VI) adsorption

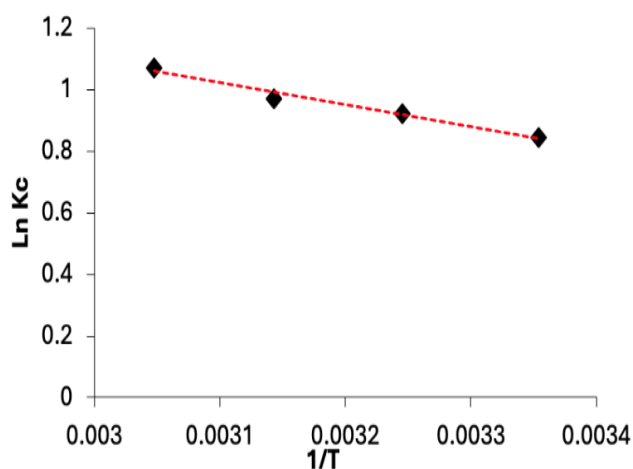
Models	Linear equations	Parameters			
Langmuir	Hanes-Woof linearization	Q_m (mg/g)	K_L (L/mg)	R^2	R_L
	$\frac{C_e}{q_e} = \frac{C_e}{Q_m} + \frac{1}{K_L Q_m}$	301.25	0.0146	0.9901	0.256
Freundlich	Scatchard linearization	Q_m (mg/g)	K_L (L/mg)	R^2	
	$\frac{q_e}{C_e} = Q_m K_L - q_e K_s$	316.25	0.0135	0.9815	
D-R		K_F (L/g)	n	R^2	
	$\ln q_e = \ln K_F + \frac{1}{n} \ln C_e$	5.958	1.325	0.9825	
		Q_m (mg/g)	K_D (mol ² /kJ ²)	E (kJ/mol)	R^2
	$\ln q_e = \ln Q_m - K_D \varepsilon^2$ $\varepsilon = RT \ln \left(1 + \frac{1}{C_e} \right)$ $E = \frac{1}{\sqrt{2K_D}}$	186.85	1.91×10^{-7}	1.618	0.9266

Table 2. Comparison of pseudo-first order and pseudo-second order adsorption rate constants, along with calculated and experimental q_e values, for various initial Cr(VI) concentrations.

C_0 (mg/L)	q_e^{exp} (mg/g)	Pseudo-first order			Pseudo-second order		
		k_1 (min^{-1})	q_e (mg/g)	R^2	k_2 ($\text{g}\cdot\text{mg}^{-1}\cdot\text{min}^{-1}$)	q_e (mg/g)	R^2
100	82.34	0.0131	58.46	0.953	0.0003	90.91	0.996
200	155.57	0.0076	42.71	0.491	0.0004	158.73	0.995
300	217.91	0.0134	100.15	0.863	0.0002	238.10	0.993
Equations		$\ln(q_e - q_i) = \ln q_e - k_1 t$ Linear plot of $\ln(q_e - q_i)$ vs. t			$\frac{t}{q_t} = \frac{1}{k_2 q_e^2} + \frac{1}{q_e} t$ Linear plot of t/q_t vs. t		

3.10. Thermodynamic parameters

The impact of temperature on Cr(VI) adsorption was examined over a range of temperatures (25 °C, 35 °C, 45 °C, and 55 °C) as shown in Fig. 10. At 25 °C, the negative value of the free energy change (ΔG°) indicates that the adsorption process occurs spontaneously, suggesting that $n\text{Fe}_3\text{O}_4$ -PPBC/Alg is effective for Cr(VI) ion adsorption. The positive ΔH° value implies that the adsorption process is endothermic. Meanwhile, the positive ΔS° value indicates an increase in disorder at the adsorbent-Cr(VI) interface during the adsorption of Cr(VI) onto the surface of $n\text{Fe}_3\text{O}_4$ -PPBC/Alg.

**Figure 10.** Plot of $\ln(Kc) - 1/T$

3.11. Comparison of adsorbent capacities

Table 4 compares the adsorption capacities reported in the literature with those observed in our study. From the analysis of these studies, it can be concluded that $n\text{Fe}_3\text{O}_4$ -PPBC/Alg exhibits a high adsorption capacity for Cr(VI) removal.

Table 3. Thermodynamic properties of Cr (VI) adsorption

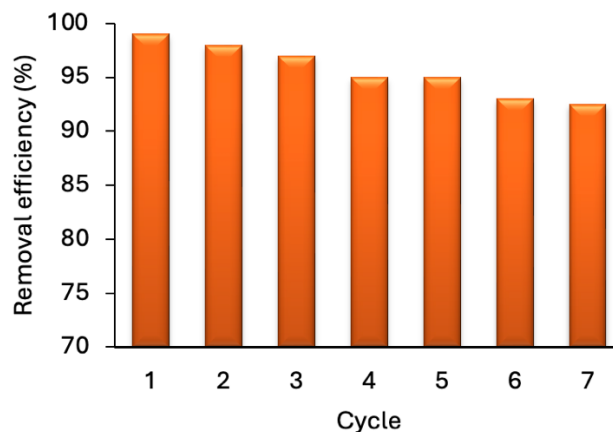
ΔS° ($\text{J K}^{-1}\cdot\text{mol}^{-1}$)	ΔH° (J mol^{-1})	ΔG° (J mol^{-1})				R^2
		$T=298\text{ K}$	$T=308\text{ K}$	$T=318\text{ K}$	$T=328\text{ K}$	
26.935	5 938.21	-2 092.39	-2 361.74	-2 631.08	-2 900.43	0.979

Table 4. Cr(VI) adsorbing capacities of different adsorbents

Adsorbent	q_e (mg/g)	Ref.
Calcium cross-linked Alginate/Chitosan biocomposite	9.8	
Iron cross-linked Alginate/Chitosan biocomposite	10.4	[5]
Zirconium cross-linked Alginate/Chitosan biocomposite	14.8	
Magnetic nano-hydroxyapatite encapsulated alginate beads	29.14	[26]
Magnetic alginate beads	14.29	[27]
Carbonized manganese-crosslinked Sodium alginate	104.50	[28]
Chitosan-humic acid-graphene oxide composite	83.64	[7]
Coffee grounds biochar/sodium alginate	30.66	[11]
Sugarcane bagasse biochar	15.73	
Brinjal stem biochar	71.89	[29]
Citrus peel biochar	16.34	
Cranberry kernel shell	6.81	
Rosehip seed shell	15.17	[24]
Banana peel	10.42	
<i>nano-Fe₃O₄/pomegranate peel biochar/alginate beads</i>	316.25	<i>This study</i>

3.12. Reusability study of $n\text{Fe}_3\text{O}_4$ -PPBC/Alg composite

$n\text{Fe}_3\text{O}_4$ -PPBC/Algae composite for Cr(VI) removal must be regenerated and reused. For this purpose, 0.01M NaOH was employed in the desorption studies [30–32]. Fig. 11 displays the graph showing the data from repeated adsorption/desorption cycles for Cr(VI) ions after 7 cycles. The data from Fig. 11 reveal a slight decrease in the adsorption capacity of $n\text{Fe}_3\text{O}_4$ -PPBC/Alg with each cycle. After 7 regeneration cycles, the Cr(VI) adsorption capacity of $n\text{Fe}_3\text{O}_4$ -PPBC/Alg only decreased by 7.5%. These results suggest that $n\text{Fe}_3\text{O}_4$ -PPBC/Alg can be effectively reused for Cr(VI) ion adsorption.

**Figure 11.** Reusability study of $n\text{Fe}_3\text{O}_4$ -PPBC/Alg

4. Conclusions

In this study, $n\text{Fe}_3\text{O}_4$ -PPBC/Alg was successfully synthesized using a straightforward method. The composite exhibited remarkable adsorption capacity, stability, and reusability, positioning it as a promising candidate for mitigating Cr(VI) pollution. The optimal reaction conditions were found to be an initial concentration of 2 mg/L, a pH of 2.0, an adsorbent dose of 1 g/L, and a reaction time of 60 minutes. The Langmuir

adsorption isotherm was found to be the most suitable for describing the observed adsorption phenomena, with the adsorption capacity of $n\text{Fe}_3\text{O}_4\text{-PPBC/Alg}$ determined to be 316.25 mg/g for Cr(VI). The $n\text{Fe}_3\text{O}_4\text{-PPBC/Alg}$ composite proves to be a highly effective for the removal of Cr (VI) from the aqueous medium. The combined effects of *nano*- Fe_3O_4 , pomegranate peel biochar, and alginate enhance the adsorption process through various mechanisms such as electrostatic interactions, surface binding, and the availability of functional groups. Additionally, the use of $n\text{Fe}_3\text{O}_4\text{-PPBC/Alg}$ adds a sustainable, cost-effective, and renewable component to the adsorbents. This research underscores the potential of such composite materials for treating industrial wastewater and highlights the significance of developing efficient, environmentally friendly adsorbent for sustainable environmental cleanup.

References

- [1] S. Dutta, R.K. Sharma, Sustainable magnetically retrievable nanoadsorbents for selective removal of heavy metal ions from different charged wastewaters, *Sep Sci Technol*, 11, 2019, 371–416.
- [2] J. Niu, P. Ding, X. Jia, G. Hu, Z. Li, Study of the properties and mechanism of deep reduction and efficient adsorption of Cr (VI) by low-cost Fe_3O_4 -modified ceramsite, *Sci Total Environ*, 688, 2019, 994–1004.
- [3] K. Staszak, I. Kruszelnicka, D. Ginter-Kramarczyk, W. Góra, M. Baraniak, G. Lota, M. Regel-Rosocka, Advances in the removal of Cr (III) from spent industrial effluents—A review, *Materials*, 16(1), 2022, 378.
- [4] D. Lohan, R. Jain, A. Srivastava, S. Dutta, D. Mohan, R.K. Sharma, Surface engineering approaches for the design of magnetic biochar-composites for removal of heavy metals: a comprehensive review, *J Environm Chem Eng*, 2023, 111448.
- [5] G. Venkatrajan, J. Venkatesan, N. Madankumar, S. Pushparaju, Effective chromium removal of metal anchored alginate-chitosan binary bio-composites. *Int J Biol Macromol*, 264, 2024, 130408.
- [6] J. Bajpai, R. Shrivastava, A.K. Bajpai, Dynamic and equilibrium studies on adsorption of Cr (VI) ions onto binary bio-polymeric beads of cross linked alginate and gelatin, *Colloids Surf A: Physicochem Eng Asp*, 236(1-3), 2004, 81–90.
- [7] Ş. Parlayıcı, A. Avcı, E. Pehlivan, Fabrication of novel chitosan-humic acid-graphene oxide composite to improve adsorption properties for Cr (VI), *Arab J Geosci*, 12, 2019, 1–13.
- [8] P. Chen, R. Cheng, G. Meng, Z. Ren, J. Xu, P. Song, H. Wang, L. Zhang, Performance of the graphite felt flow-through electrode in hexavalent chromium reduction using a single-pass mode, *J Hazard Mater*, 416, 2021, 125768.
- [9] Y. Liu, X. Ke, X. Wu, C. Ke, R. Chen, X. Chen, X. Zheng, Y. Jin, B. Van der Bruggen, Simultaneous removal of trivalent chromium and hexavalent chromium from soil using a modified bipolar membrane electrodialysis system, *Environ Sci Technol*, 54(20), 2020, 13304–13313.
- [10] A. Kuanar, S.K. Kabi, M. Rath, N.K. Dhal, R. Bhuyan, S. Das, D. Kar, A comparative review on bioremediation of chromium by bacterial, fungal, algal and microbial consortia, *Geomicrobiol J*, 39(6), 2022, 515–530.
- [11] Y. Tian, X. Sun, N. Chen, X. Cui, H. Yu, Y. Feng, D. Xi, W. He, Efficient removal of hexavalent chromium from wastewater using a novel sodium alginate-biochar composite adsorbent, *J Water Process Eng*, 64, 2024, 105655.
- [12] B. Devi, M. Goswami, A. Devi, Entrapment behaviours of trivalent and hexavalent chromium from aqueous medium using edible alkali-derived activated carbon of *Eichhornia crassipes* (water hyacinth), *Environ Sci Pollut Res*, 31(4), 2024, 6025–6039.
- [13] Ş. Parlayıcı, E. Pehlivan, An ecologically sustainable specific method using new magnetic alginate-biochar from acorn cups (*Quercus coccifera* L.) for decolorization of dyes, *Polymer Bull*, 80(10), 2023, 11167–11191.
- [14] L. Li, Q. Liao, B. Hou, C. He, J. Liu, B. Li, M. Yu, Y. Liu, B. Lai, B. Yang, Synchronous reduction and removal of hexavalent chromium from wastewater by modified magnetic chitosan beads, *Sep Purif Technol*, 304, 2023, 122363.
- [15] Q. Feng, B. Wang, M. Chen, P. Wu, X. Lee, Y. Xing, Invasive plants as potential sustainable feedstocks for biochar production and multiple applications: a review, *Resour Conserv Recycl*, 164, 2021, 105204.
- [16] C. Zhao, B. Wang, B.K.G. Theng, P. Wu, F. Liu, S. Wang, X. Lee, M. Chen, L. Li, X. Zhang, Formation and mechanisms of nano-metal oxide-biochar composites for pollutants removal: a review, *Sci Total Environ*, 767, 2021, 145305.
- [17] S. Fan, J. Zhou, Y. Zhang, Z. Feng, H. Hu, Z. Huang, Y. Qin, Preparation of sugarcane bagasse succinate/alginate porous gel beads via a self-assembly strategy: Improving the structural stability and adsorption efficiency for heavy metal ions, *Bioresour Technol*, 306, 2020, 123128.
- [18] Y. He, J. Chen, J. Lv, Y. Huang, S. Zhou, W. Li, Y. Li, F. Chang, H. Zhang, T. Wagberg, G. Hu, Separable amino-functionalized biochar/alginate beads for efficient removal of Cr (VI) from original electroplating wastewater at room temperature, *J Clean Product*, 373, 2022, 133790.
- [19] R. Sun, S. Gao, K. Zhang, W. T. Cheng, G. Hu, Recent advances in alginate-based composite gel spheres for removal of heavy metals, *Int J Biol Macromol*, 2024, 131853.
- [20] R. Wen, B. Tu, X. Guo, X. Hao, X. Wu, H. Tao, An ion release controlled Cr (VI) treatment agent: Nano zero-valent iron/carbon/alginate composite gel, *Int J Biol Macromol*, 146, 2020, 692–704.
- [21] A. F. Hassan, A. M. Abdel-Mohsen, H. Elhadidy, Adsorption of arsenic by activated carbon, calcium alginate and their composite beads, *Int J Biol Macromol*, 68, 2014, 125–130.
- [22] F. Amalina, A.S. Abd Razak, S. Krishnan, A.W. Zularisam, M. Nasrullah, A comprehensive assessment of the method for producing biochar, its characterization, stability, and potential applications in regenerative economic sustainability—a review, *Clean Mater*, 3, 2022, 100045.
- [23] B.H. Hameed, A.A. Ahmad, Batch adsorption of methylene blue from aqueous solution by garlic peel, an agricultural waste biomass, *J Hazard Mater*, 164(2-3), 2009, 870–875.
- [24] Ş. Parlayıcı, E. Pehlivan, Comparative study of Cr (VI) removal by bio-waste adsorbents: equilibrium, kinetics, and thermodynamics, *J Anal Sci Technol*, 10(1), 2019, 1–8.
- [25] A.P. Mikolajczyk, D.L.B. Fortela, J.C. Berry, W.M. Chirdon, R.A. Hernandez, D.D. Gang, M.E. Zappi, Evaluating the suitability of linear and nonlinear regression approaches for the Langmuir adsorption model as applied toward biomass-based adsorbents: Testing residuals and assessing model validity, *Langmuir* 2024, 40(39), 20428–20442.
- [26] S. Periyasamy, V. Gopalakannan, N. Viswanathan, Hydrothermal assisted magnetic nano-hydroxyapatite encapsulated alginate beads for efficient Cr (VI) uptake from water, *J Environ Chem Eng*, 6(1), 2018, 1443–1454.
- [27] V. Gopalakannan, N. Viswanathan, Synthesis of magnetic alginate hybrid beads for efficient chromium (VI) removal, *Int J Biol Macromol*, 72, 2015, 862–867.
- [28] W. Mao, L. Zhang, Y. Zhang, Y. Wang, N. Wen, Y. Guan, Adsorption and photocatalysis removal of arsenite, arsenate, and hexavalent chromium in water by the carbonized composite of

- manganese-crosslinked sodium alginate, *Chemosphere*, 292, 2022, 133391.
- [29] H. Chaudhary, K. S. Rao, Impact of biochar produced at different pyrolysis conditions on heavy metal contaminated soil, *Environ Geochem Health*, 46(9), 2024, 307.
- [30] Y. Cao, J. Huang, X. Peng, D. Cao, A. Galaska, S. Qiu, J. Liu, M.A. Khan, D. Young, J.E. Ryu, H. Feng, N. Yerra, Z. Guo, Poly (vinylidene fluoride) derived fluorine-doped magnetic carbon nanoadsorbents for enhanced chromium removal, *Carbon*, 115, 2017, 503–514.
- [31] J. Wang, K. Pan, Q. He, B. Cao, Polyacrylonitrile/polypyrrole core/shell nanofiber mat for the removal of hexavalent chromium from aqueous solution, *J Hazard Mater*, 244, 2013, 121–129.
- [32] C. Luo, Z. Tian, B. Yang, L. Zhang, S. Yan, Manganese dioxide/iron oxide/acid oxidized multi-walled carbon nanotube magnetic nanocomposite for enhanced hexavalent chromium removal, *Chem Eng J*, 234, 2013, 256–265.



Catalytic co-pyrolysis of PET/PP plastics and olive pomace biomass with marble sludge catalyst*

Esra Yel**¹ , Merve Kalem¹ , Gamze Goktepelı¹ , Afra Kurt² , Gulnare Ahmetli³ , Vildan Onen⁴ 

¹ Konya Technical University, Faculty of Engineering and Natural Science, Department of Environmental Engineering, 42250, Selçuklu-Konya, Türkiye

² Konya Technical University, Graduate Education Institute, Graduate Education Institute MSc Program, 42250, Selçuklu-Konya, Türkiye

³ Konya Technical University, Faculty of Engineering and Natural Science, Department of Chemical Engineering, 42075, Selçuklu-Konya, Türkiye

⁴ Konya Technical University, Faculty of Engineering and Natural Science, Department of Mining Engineering, 42075, Selçuklu-Konya, Türkiye

Abstract

Sustainable and efficient waste management requires involvement of symbiotic solutions to various types of wastes, and so to achieve circular economy. Through this motivation, in this study, combined thermochemical conversion (pyrolysis) of plastics, biomass and marble processing effluents physicochemical treatment sludge (K1) were studied. In this combination, plastics were petroleum-based synthetic aromatic (PET) and aliphatic (PP) organics, while olive pomace-OP was natural agricultural residue. K1 was mineral product, which was first introduced in the literature as pyrolysis catalyst by the authors. In the study, co-pyrolysis of polymers and biomass was catalyzed by mineral waste containing CaCO₃. The effect of plastic type and pyrolyzed material mixture ratio on pyrolysis fractions were investigated. Moreover, material recovery potential from pyrolysis fractions was discussed. In catalytic co-pyrolysis, by increasing the plastic ratio in the mixture, the pyrolytic liquid and oligomer fraction increased while the solid (char) and gas fraction decreased. For 70%PP+15%OP+15%K1 mixture, liquid product was dominant, whereas with 60%PET+20%OP+20%K1 much more pyrolytic gas fraction was produced. The thermal degradation of char products did not exceed 2-3% up to 600 °C and this stability continues up to approximately 700 °C reveals the potential of the char to be used in alternative areas as a material with high thermal resistance, for example, as adsorbent, in cathodic electrode production, in compost or in composite. The catalytic co-pyrolysis liquid products contain alkanes, alkenes, acids, phenols, benzene, aldehydes, esters, alcohols and ketones. Benzene, acid and alcohol groups were dominant in liquids, while alkane, alkene and alkyne groups were dominant in gases.

Keywords: Biomass, catalytic co-pyrolysis, industrial symbiosis, marble sludge, plastic wastes

1. Introduction

Sustainable and efficient waste management requires involvement of symbiotic solutions to various types of wastes, and therefore, to achieve circular economy. Among the major contributors to carbon footprint the production assemblies and fuels play an important part. Within the scope of circular economy carbon footprint reduction efforts include the upcycling of wastes [1]. Biomass and plastic wastes are natural and synthetic organics, respectively, and their efficient conversion provides mitigation of the pollution caused by them. Instead of produce-use-dispose approach of linear economy, more sustainable approaches are getting popular in terms of circular economy. In circular economy the concept of upcycling is the conversion of waste materials into materials of higher value/quality,

lower carbon footprint. Making waste management providing better quality products with upcycling as a more creative approach than recycling. It may be feasible to examine the symbiotic recovery approaches for wastes that can be converted to new generation low-carbon products symbiotically. Post-consumer plastic wastes, which are synthetic polymers make up a sizeable portion of solid wastes. The volume of post-consumer plastic waste is rising due to an increase in the use of plastic in disposable consumer materials [2]. It is projected that by 2050, either landfills or the natural environment will receive about 12,000 Mt of plastic waste [3]. In the two-phase olive oil extraction system approximately 80% of the olive mass becomes OP which is composed of olive pulp, skin, crushed pits and

Citation: E. Yel, M. Kalem, G. Goktepelı, A. Kurt, G. Ahmetli, V. Onen, Catalytic Co-pyrolysis of PET/PP Plastics and Olive Pomace Biomass with Marble Sludge Catalyst, Turk J Anal Chem, 7(1), 2025, 33–45.

****Author of correspondence:** eyel@ktun.edu.tr

Tel: +90 (332) 205 16 10

Fax: +90 (332) 241 06 35

Received: December 30, 2024 **Accepted:** January 22, 2025

doi <https://doi.org/10.51435/turkjac.1609960>

*This paper was presented at the 6th International Environmental Chemistry Congress, EnviroChem 05-08 November 2024, Trabzon Türkiye.

residual olive oil as well as a notable moisture content (60–70%) [4]. Marble industry generates inorganic marble particles (mainly in CaCO_3 structure) during processing stages, and these are important pollutants either in the air or in water.

Cycling of a single type of waste may produce new products more valuable than the previous, yet, co-processing of more than one type of waste may result in more valuable upcycled products. Pyrolysis is reported as a carbon negative process; the pyrolytic reactions produce oil, gas and char fractions that are able to meet the circular economy and hydrocarbons closed-loop recycling [5]. Strategies for converting biomass and plastic waste in achieving affordable and clean energy in a sustainable manner, which denotes Sustainable Development Goal 7 (SDG7) [6].

It can be emphasized that the industrial symbiosis approach, which focuses on product and resource recycling to create closed-loop systems that essentially aim to produce less waste and consume fewer natural resources, is very important to encourage advanced recycling approaches. One of these approaches is the pyrolysis process. During thermal decomposition, there are chain-breaks and new molecules of different sizes are formed. Since most of these molecules are radical in character, they can turn into gas, liquid and solid products by giving a series of reactions among themselves. The pyrolysis reaction conditions can be inert, oxidative or reductive, catalytic or non-catalytic.

The synergistic effects of co-pyrolysis (pyrolyzing polymers and biomass mixtures together) can improve products quality to valuable hydrocarbons [7–9]. Co-pyrolysis offers an attractive pathway with high potential for mixed wastes by minimizing the requirements on waste separation [10,11]. The use of synthetic polymers with biomass in the co-pyrolysis process can balance the elemental content in the feedstock, improving the properties of degradation products [12]. In their study, Özsin and Pütün [13] co-pyrolyzed walnut shells (WS) and peach stones (PST) were selected as biomass species. They reported that positive or negative synergy depends on the type and contact of components, pyrolysis duration, temperature and heating rate, removal or equilibrium of volatiles formed, and addition of solvents, catalysts, and hydrogen-donors. Among these factors, the types of blending feedstock are the major factor that can significantly influence the synergistic effects [9].

Compared to synthetic polymers, biomass has lower thermal stability and this promotes the degradation of synthetic macromolecules [14]. Biomass is the green source of renewable carbon, but its bio-oil contains a mixture of complex oxygenated compounds such as carboxylic acids, aldehydes, furans, anhydrosugars,

ketones, esters, ethers and phenols which gives the bio-oil undesirable properties making its use as a direct substituent for fossil fuel difficult. Plastic wastes contain high H/C ratio and relatively low O/C ratio while its vice versa for biomass and this results in increased quality and uniformity of the products [15]. During co-pyrolysis, plastics serve as hydrogen donors. Hydrogen is transferred to the biomass-derived radicals, which can improve the oil quality and increase its quantity [4,16–19]. Co-pyrolysis of plastics and OP biomass was reported as innovative solution for sustainable results [1]. By taking advantage of the unique chemical composition of OP biomass and its synergistic interactions with plastics, co-pyrolysis serves the development of new functional materials and additives with improved performance and sustainability credentials [1].

Catalytic pyrolysis processes are widely used for converting polymers into fuel or raw material hydrocarbon mixtures. Catalysts have significant effects on the yield and composition of thermal decomposition products [6,20–22]. Abnisa and Daud [9], Hassan et al. [23] and Zhang et al. [24] reviewed and summarized non-catalytic and catalytic co-pyrolysis and their benefits on biomass and waste plastics co-pyrolysis oil product quality enhancement. Catalytic co-pyrolysis of waste plastic and lignocellulosic biomass can provide superior performance in upgrading pyrolysis oil e.g. produce aromatics along with char reduction [10,23,24]. Catalytic co-pyrolysis of plastic and solid biomass can be developed as in-situ (the catalyst is mixed with the feedstock and placed in the same reactor) or ex-situ (catalyst is separated from the feedstock into a separate downstream reactor) catalysis [25]. The role of plastic to biomass ratio, catalyst, feedstock to catalyst ratio, reaction temperature and co-pyrolysis method are very important in catalytic co-pyrolysis of plastic and solid biomass [10,26]. Mo et al. [26] revealed that future research should focus on the development of efficient catalysts that can effectively convert biomass and plastic waste into useful hydrocarbons. Additionally, research should focus on improving the understanding of the catalytic co-pyrolysis process and the effects of different reaction conditions. Sanchez-Avila et al. [1] inferred that additional research is needed to evaluate the synergistic impact of varying mixing ratios of plastics and OP co-pyrolysis.

Therefore, in this study, as thermochemical conversion, co-pyrolysis of polymers (PET and PP wastes) and lignocellulosic biomass (OP) was catalyzed by mineral waste containing CaCO_3 (marble processing wastewater treatment sludge). By this approach, it was aimed to contribute industrial symbiosis solutions. The effect of plastic type and pyrolyzed material mixture

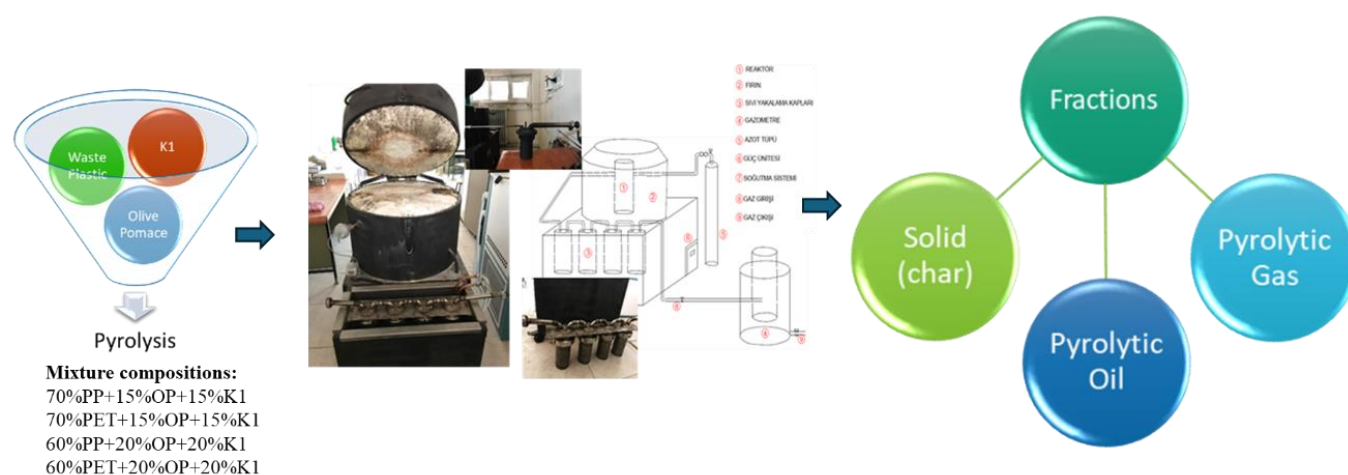


Figure 1. Experimental diagram of in-situ catalytic co-pyrolysis process

ratio on pyrolysis fractions were investigated. Moreover, material recovery potential from pyrolysis fractions was discussed.

2. Materials and method

Co-pyrolysis and catalytic pyrolysis of polymeric material and biomass are among the widely studied applications in the literature. In this study, catalytic co-pyrolysis was applied using three wastes (PET/PP wastes, K1 and OP wastes) and pyrolysis product characterizations were presented. K1 was a mineral product obtained from marble processing industry effluent physicochemical treatment sludge. K1 was first introduced in the literature as pyrolysis catalyst by the authors [27–29]. Co-pyrolysis process was conducted at fixed bed pyrolysis reactor (Fig. 1) at 500 °C pyrolysis temperature with no retention at target temperature. Total mass at each run was arranged as 100 g.

In the previous studies of the authors, it was evaluated that in the catalytic pyrolysis of K1 with plastics, the majority of the reactions were generally completed at the pyrolysis temperature of 500 °C (turning point) in the characterization findings, the most stable pyrolysis products were generally obtained at this temperature, the change in product characteristics was less above 500 °C. Therefore, it was not necessary to work at higher temperatures by spending more energy [27–30]. For this reason, catalytic co-pyrolysis studies were applied as non-retention pyrolysis at the target pyrolysis temperature of 500 °C. In previous studies, it was evaluated that 40% K1 dose in plastic+K1 mixtures provided sufficient maximum fragmentation and that no significant difference was observed in pyrolysis chars at 50% K1 dose, and 40% K1 dose (60% plastic presence in the environment) was recommended for pyrolysis experiments with retention [27–30]. In this study, plastics were selected as the main base material and two different mixing ratios were studied for each plastic

(Fig. 1). The mixing ratios studied were 60% PET or PP waste, and 70% PET or PP waste. In each plastic percentages, OP and K1 ratios were kept equal, to prevent changes due to proportional differences.

Char calorific values were determined by bomb calorimeter. For comparison, theoretical calorific values were calculated by using a simple mass balance calculation, in which the calorific values of the char unit mass were assumed to be linear and multiplied by the ratios of the components in the mixture to calculate the theoretically expected calorific values as; %Plastic in mixture*Plastic's heat value + %OP in mixture*OP's heat value = Theoretical cal/g

TGA analyses were performed for the thermal characteristics of the pyrolysis chars and liquid products. FTIR analyses were conducted to analyze the structural differences in the chars and liquid. SEM images were used for the characterization of surface morphology of the pyrolysis chars. GC-MS/FID were used for analyzing the organic compounds found in both pyrolysis liquid and gas products.

3. Results and discussion

3.1. PET/PP+OP+K1 catalytic co-pyrolysis product yields

The product fractions obtained as a result of catalytic co-pyrolysis of PET and PP plastic waste types with OP and K1 at 500 °C were shown in Fig. 2. In catalytic co-pyrolysis with PET, the char and gas fractions decreased while the liquid and oligomer fractions increased by increasing the PET ratio from 60% to 70% and decreasing the OP and K1 ratios from 20% to 15%. In the mixtures containing PP instead of PET, char and gas decreased and the liquid fraction increased with the increasing PP dose. PP was effective in the formation of liquid product, whereas in the mixtures containing PET, the gas product was dominantly higher (Fig. 2). When the OP ratio in the catalytic co-pyrolysis sample, i.e. the decrement of the

lignocellulosic structure, the phenolic compounds originating from this structure will also decrease. In the first stage of dehydration and demethylation reactions, compounds with high molecular weight and condensation temperature are formed [31]. Accordingly, since more fluid fraction is concentrated in samples containing less OP, the liquid product yield is higher. It can also be said that the reaction rate increases and the amount of gas increases with more degradation in the case of increment in the amount of K1 in the mixture. The amount of higher solid product in samples containing 60% plastic was primarily related to the higher amount of K1 in the mixture. The lower amount of char in PP containing mixtures was interpreted as PP disintegrating more in the presence of OP and the organic structures in the char were less. This situation was examined in characterization studies. In terms of liquid product yield, it can be recommended to perform catalytic co-pyrolysis in a composition of 70%PP+15%OP+15%K1, whereas, 60%PET+20%OP+20%K1 with PET can be recommended in processes where gaseous product is aimed to be obtained (Fig. 2).

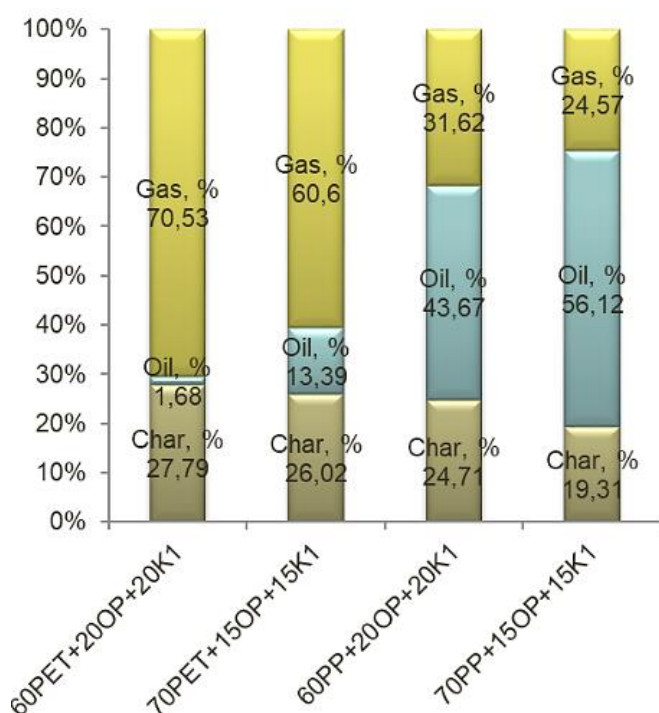


Figure 2. Catalytic co-pyrolysis product yields

The composition of wastes significantly impacts the efficiency and selectivity of catalytic co-pyrolysis. Synergistic effect is the sum of the individual effects or contributions of the co-feeding factors when two or more factors interact. Biomass thermally decomposes through a number of exothermic and endothermic reaction mechanisms. Plastic pyrolysis occurs through radical mechanisms involving initiation, propagation, and

revocation through the use of radicals' disproportionation or recombination [26]. Different types of plastics have different chemical structures and properties, that affect their reaction during pyrolysis. PET is aromatic structure which can produce a high yield of aromatic hydrocarbon feedstocks used in the production of plastics, fuels, and chemicals, whereas, PP is aliphatic structure, these compounds can produce a high yield of liquid fuels [23,26]. In their synergistic interaction, biomass and plastics exchange radicals and elemental particles during the co-pyrolysis process and this interaction affects both the quality and quantity of the products [26]. Catalysts exhibit a minor deoxygenation effect on the products compared to the non-catalytic co-pyrolysis process, changing in the hydrocarbon content [4]. CaO, which is the component of catalyst in this study can effectively convert acidic compounds into stable molecules by acting as an absorbent, a reactant, and a catalyst. It can absorb CO₂ from the gaseous product leading to an apparent increase in the H₂ content while reducing the gaseous products [32] (Fig. 2).

In the literature, there has not been exactly similar study with same waste blends and the same catalysts. Grause et al [33] reported 30–50% oil product yield from catalytic pyrolyses under the catalysis of CaO and Ca(OH)₂ and It was estimated that the effect of Ca forms change with the type of material pyrolysed [34]. Gulab et al, [35] reported 26.6% oil production in which CaCO₃ pyrolysis favors formation of aromatic hydrocarbons. Catalytic co-pyrolysis improve the bio-oil quality by reducing oxygen content through hydro-deoxygenation and liquid yield of 57.0 wt% was reported [36]. High cracking and reforming effects of this low-cost, abundant K1 with its mainly CaCO₃ content was intended to increase pyrolytic fluids (oil+gas) quality and quantity. Tang et al [37] reported 32.8% gas, 46.8% oil and 20.4% solid product yields at the same temperature with CaO catalyst, indicating that the addition of CaO during the pyrolysis of waste biomass and plastics significantly enhances the catalytic thermal cracking reactions of tar compounds. By using K1, in the PET catalytic co-pyrolysis, gas product yield could be increased to above 70%, while the oil product yield was increased to above 56% for PP catalytic co-pyrolysis.

3.2. PET/PP+OP+K1 catalytic co-pyrolysis solid product characteristics

The solid products obtained from PET/PP+OP+K1 catalytic co-pyrolysis are expected to be structurally dominated by carbon and calcium carbonate. According to the findings of the authors' previous studies, the surface acid values of the char products obtained from the mixtures of PET+20%K1, PP+20%K1 and OP+20%K1

at 500 °C pyrolysis temperature were determined as 0.16 mmol/g, 0.10 mmol/g and 0.06 mmol/g, respectively [30]. In PET+OP+K1 catalytic co-pyrolysis studies, the chars obtained with 60PET+20OP+20K1 and 70PET+15OP+15K1 mixtures at the same temperature had higher surface acid values (Table 1). In catalytic co-pyrolysis, it was observed that the decrease in the ratio of K1 in the alkaline structure caused a slight increase in the surface acid value of the char sample. Surface acidity represents the oxygenated components in the structure of the sample and affects its thermal properties. High acidity favors overreaction of reactants and increases repolymerization of molecules leading to the formation of poly-aromatics. In summary, acid sites promote deoxidation, cleavage, oligomerization, alkylation, isomerization, cyclization and aromatization [4].

Table 1. Calorific values and ash contents of catalytic co-pyrolysis char products at 500 °C

Mixture, %			Char			Ash (%)
			Surface Acidity, mmol/g	Theoretical Heat value (cal/g) [†]	Measured Heat value (cal/g)	
60PET	20OP	20K1	0.18	2905	3103.8	37.91
70PET	15OP	15K1	0.24	3183	3669.5	34.04
60PP	20OP	20K1	0.05	640	818.3	72.43
70PP	15OP	15K1	0.06	540	971.7	69.08

[†] 0.6*4015 + 0.20*2480 = 2905 cal/g

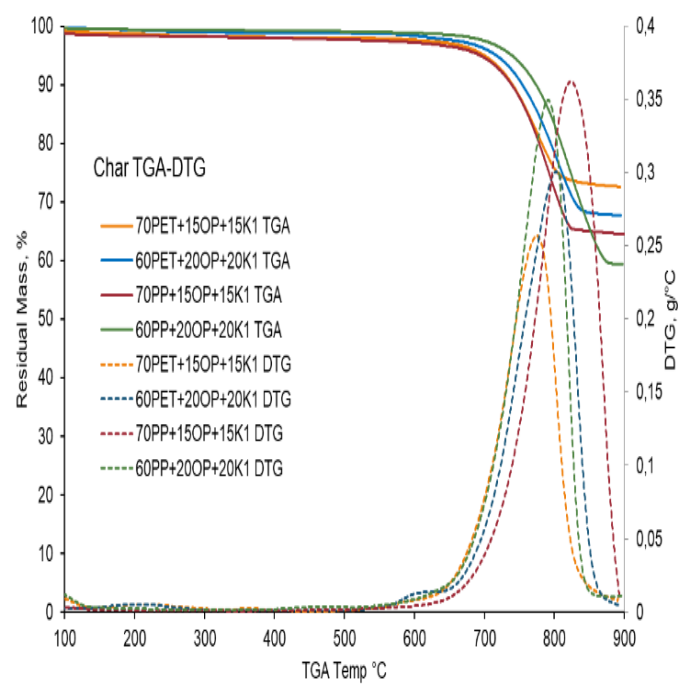
0.7*4015 + 0.15*2480 = 3182.5 cal/g

0.6*239.8 + 0.20*2480 = 640 cal/g

0.7*239.8 + 0.15*2480 = 539.9 cal/g

The calorific values of chars were significantly higher in mixtures containing PET compared to those containing PP (Table 1). In the authors' previous studies, the calorific values of char products obtained at 500 °C pyrolysis temperature of PET+20%K1, PP+20%K1 and OP+20%K1 mixtures were determined as 4015 cal/g, 239.8 cal/g and 2480 cal/g, respectively [30]. The char obtained at 60%PET+20OP+20K1-500 °C pyrolysis condition had a calorific value of 3103.8 cal/g. It was observed that the calorific value of the char product obtained at 70%PET+15OP+15K1-500 °C pyrolysis condition increases slightly by increasing the PET ratio, which provides higher calorific value, and decreasing the OP and K1 ratios. With a simple mass balance calculation, the calorific values of the char unit mass were assumed to be linear and multiplied by the ratios of the components in the mixture to calculate the theoretically expected calorific values (Table 1). The measured calorific values of the char were significantly higher than the calculated values, and in addition, the char calorific value of the sample containing 60% PP was expected to be higher than the one containing 70% PP, but it was lower (Table 1). Compared to the situation in chars obtained in binary combinations of wastes, the fact that the higher calorific value was reached when the OP

in the mixture decreases when the three wastes were pyrolyzed together indicates that the catalytic co-pyrolysis reaction mechanisms operate differently. The calorific value depends on the carbon, hydrogen and oxygen content, as well as the H/C ratio. When plastics were used in the reaction, this ratio increased due to the contribution of the H atoms provided by the plastic and accordingly the O atoms decreased, thus the calorific value increased [38]. Co-pyrolysis of PET with biomass can lead to complete suppression of crystallites in PET and minimize the formation and growth of polycyclic aromatic hydrocarbons (PAHs) at 500 °C. However, at extreme temperatures, the formation and growth of PAHs increases due to the increase in the concentration of radicals. Radical formation on biomass is essential for synergistic improvement of the calorific value of char by affecting other carbon structures during co-pyrolysis [39]. Similarly, the ash contents of char products obtained from PET+%20K1, PP+%20K1 and OP+%20K1 mixtures were 30%, 56.6% and 57%, respectively. Contrary to the calorific values, ash contents were higher in ternary mixtures containing PP compared to those containing PET (Table 1). It was observed that as the OP and K1 ratio in the mixture increases, calorific values decrease, and ash contents increase. A systematic difference can also be mentioned between PET and PP.



Mixture, %			Tonset, °C*	Tend, °C**	T ₅ , °C	T ₁₀ , °C	T ₅₀ , °C	Residue at 900 °C (%)
60PET	20OP	20K1	560	875	700	740	>900	72.5
70PET	15OP	15K1	550	843	717	754	>900	67.7
60PP	20OP	20K1	595	857	694	739	>900	64.4
70PP	15OP	15K1	620	893	739	774	>900	59.3

*Tonset: degradation begins; **Tend: degradation finishes; T₅, 10, 50: temperatures of 5, 10 and 50% degradation

Figure 3. TGA-DTG curves and thermogravimetric findings of catalytic co-pyrolysis chars

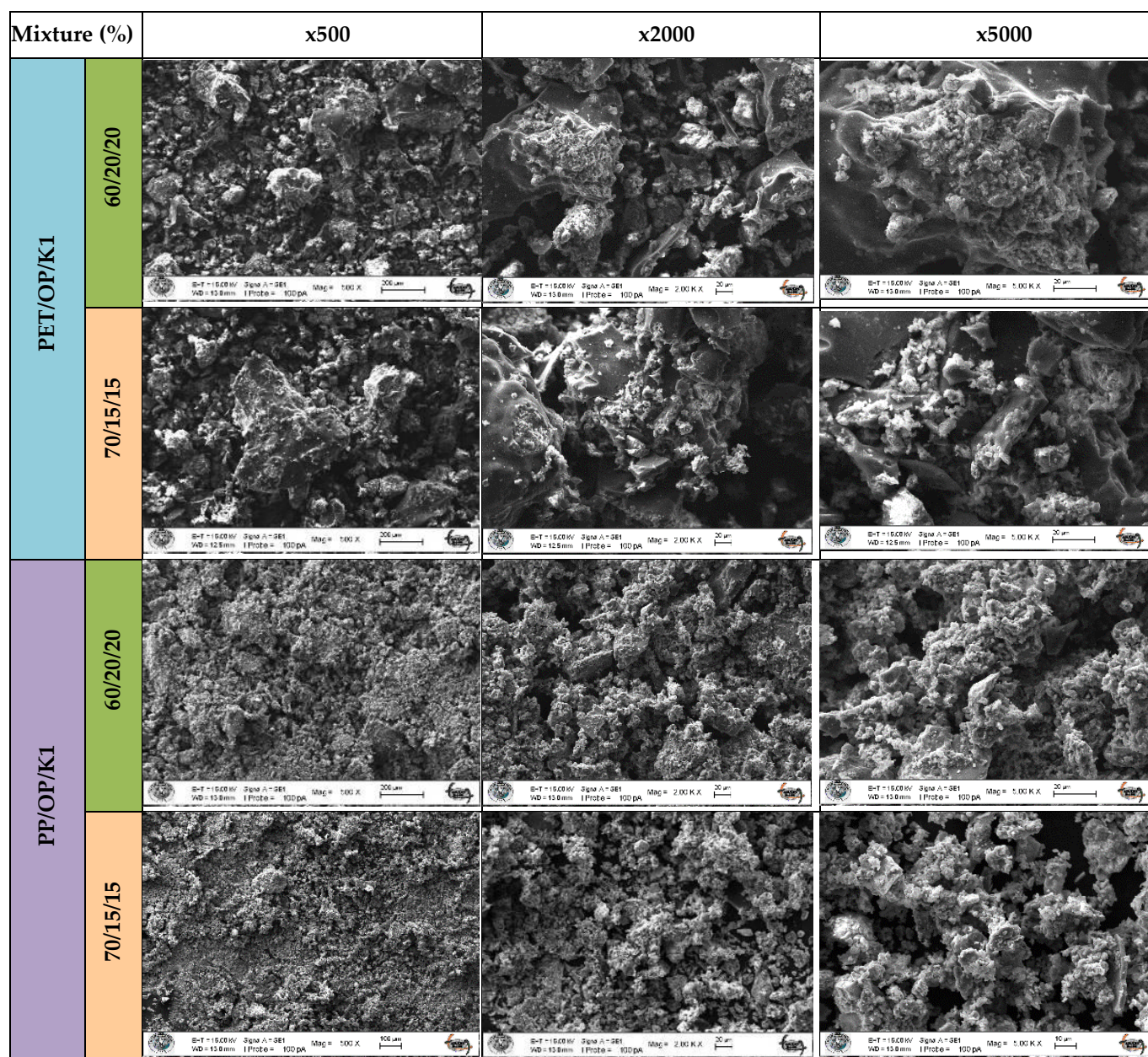


Figure 4. SEM images of char products obtained from the catalytic co-pyrolysis of PET and PP with OP and K1

Thermochemical properties of the solid products were presented in Fig. 3. With the increase in OP and K1 doses in pyrolysis mixtures there was an increase in T_{onset} and T_{end} values for PET and vice versa for PP plastics. In mixtures with higher K1 doses, the char obtained became more thermally resistant. The reason for this situation can be explained as the increase in the amount of mineral structured catalyst in the solid product and the acceleration of the decomposition reaction, making this product inert composition. This situation was also observed in studies where mineral catalysts with a similar structure to K1 were used [40,41]. At the same time, the increase in OP amount plays a role in the increase in thermal resistance for both plastic types. The majority of hemicellulose, cellulose and volatile substances in the OP decompose between 177–380 °C. Hemicellulose decomposes between 157–357 °C under

the influence of volatile substances with low molecular weight. Cellulose in the OP structure also begins to decompose between 240–390 °C [42]. The amount of residue left by all samples at 900 °C is more than 50%. According to this residue value, it was determined that the chars obtained in the catalytic co-pyrolysis carried out with PET type plastic wastes were thermally more resistant than PP. However, this finding in the final residue value showed the opposite throughout the degradation reaction. The thermogram of PP-60, which progresses above all curves in Fig. 3 from 600 °C where the decomposition starts, continued as the most resistant char up to 850 °C, but resulted in the lowest residue at the end of the decomposition. Similarly, the thermogram of PET-60 was the second curve from the top, and it resulted in a lower residue than PET-70 at the end. The fact that the decomposition does not exceed 2–3% up to

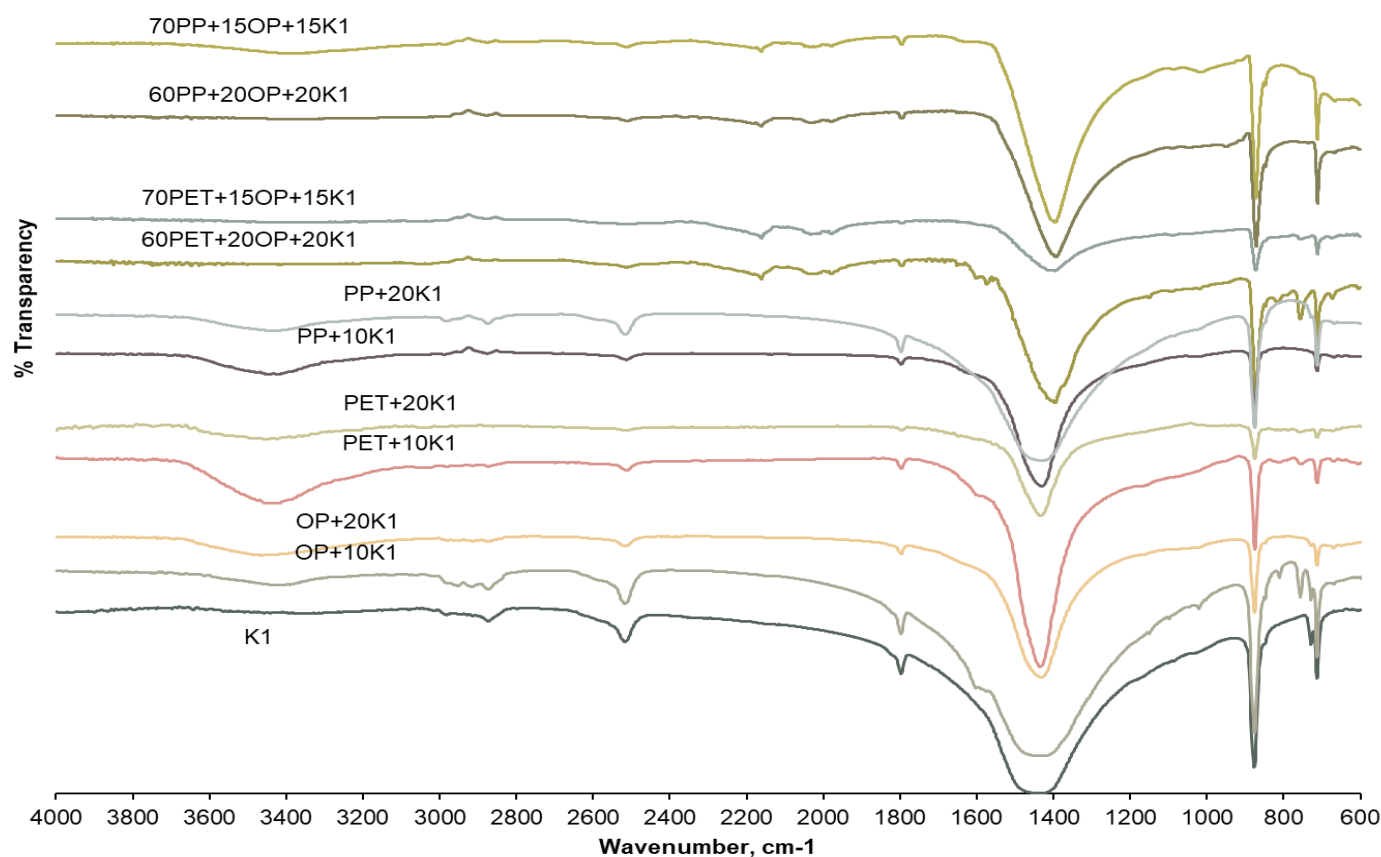


Figure 5. FTIR spectra of PET/PP+OP+K1 catalytic co-pyrolysis chars

600 °C in all thermograms and this stability continues up to approximately 700 °C reveals the potential of the chars obtained with the ternary mixture to be used in alternative areas as a material with high thermal resistance.

SEM images of chars were given in the Fig. 4. In SEM images (Fig. 4), while the agglomeration was more in samples containing PET and the sticky surface image between particles was more apparent. However, in PP chars, more separate and powdery surfaces were noticeable. Char products of PET type plastics at 500 °C for 15% OP and K1 doses, it was observed that the particles were stuck to each other and had a granular structure. It was determined that with the increase in the dose of OP and K1, smaller agglomerations were formed as a result of the non-degradable lignocellulosic structures that caused the adhesion between the particles and the better decomposition of PET fibers (Fig. 4). In the pyrolysis of PP with 15% OP and K1, it was determined that the particle distribution formed by the breakdown of the polymer structure was more homogeneous than PET; the surface roughness and agglomeration of the char increased slightly with the increase of the OP and K1 dose to 20% (Fig. 4). PP is an aliphatic polymer, and the breakdown of PP is almost completed at 500 °C [27–29], but the lignin ratio increases with the increase of the OP ratio in the mixture and not all of the lignin is

broken down at this temperature. The increase in agglomeration and surface roughness can be associated with the increase in the lignin ratio remaining from the breakdown in the char structure.

The structural differences in the chars obtained at 500°C catalytic co-pyrolysis of PET/PP+OP+K1 blends were compared with their FTIR spectra (Fig. 5). The bands belonging to the components in the calcite and travertine structure seen at 712 cm⁻¹, 872 cm⁻¹, 1795 cm⁻¹ and 2509 cm⁻¹ in the FTIR spectra of the chars obtained from the catalytic co-pyrolysis of 60PET+20OP+20K1 and 60PP+20OP+20K1 were an indication that the K1 initially present in the mixture can be completely or partially recovered. Disubstituted benzenes with carbonyl groups at 756 cm⁻¹, C-H bond at 673 cm⁻¹, mono o-substituted benzene at 756 cm⁻¹, trisubstituted double bond at 816 cm⁻¹, mono p-substituted benzene at 847 cm⁻¹, C=C ring stretching of lignin at 1397 cm⁻¹, amine at 1557 cm⁻¹, benzene ring C=C bond at 1574 and 1594 cm⁻¹, aromatic C=C at 1600 cm⁻¹, Si-O and Si-H stretching due to 1979 and 2027 were observed. Most of these bands were also present in the odor spectrum of 70PET+15OP+15K1 catalytic co-pyrolysis, but some band intensities are decreased. The decrease in the band intensity of the C=C ring stretching of lignin at 1397 cm⁻¹ can be interpreted as the decrease in the OP ratio in the mixture; the decrease in the band intensities at 872 cm⁻¹ and 712 cm⁻¹ can be interpreted as the decrease in the K1 ratio in the mixture.

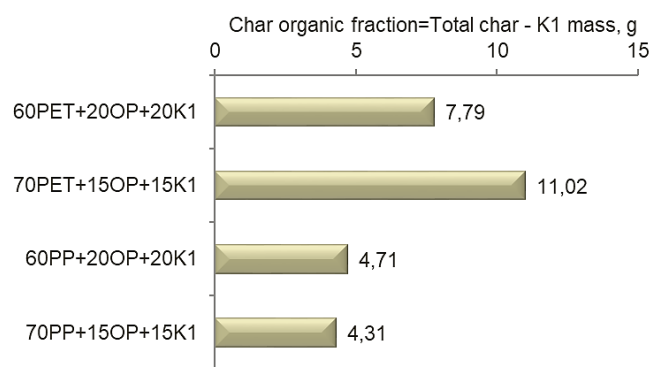


Figure 6. Differences between the initial K1 masses of pyrolysis solid products for PET/PP+OP catalytic co-pyrolysis

The formation of the new bands, the aromatic C-H at 1091 cm^{-1} and the alkyne group at 2161 cm^{-1} , may be due to the higher PET ratio in the mixture (Fig. 5). In the mixture of 60PP+20OP+20K1, mono p-substituted benzene at 848 cm^{-1} , C=C ring stretching of lignin at 1394 cm^{-1} , aromatic C=C at 1600 cm^{-1} , alkyne at 2161 and 2511 cm^{-1} , and aromatic unsaturated compound at 2034 cm^{-1} are observed (Fig. 5). The same bands belonging to the catalytic co-pyrolysis char containing 60%PP were also observed in the catalytic co-pyrolysis spectrum of 70PET+15OP+15K1 and changes were observed in some band intensities.

3.3. Sustainable utilization of pyrolysis solid products

Both carbon structure and K1 were present in pyrolysis chars as mentioned in previous sections. For this reason, in this section, the amounts of K1 initially put into the reactor were deducted from the amounts of solid products and the remaining masses were compared (Fig. 6). The amount and quality of organic components in the solid product affect the usage of the catalyst. Fig. 6 shows how much difference there was in the solid product content after pyrolysis, in addition to the amount of catalyst used at the beginning. The char in the PET+OP+K1 solid product content was higher than the

PP+OP+K1 char. The degradation at high K1 doses was also associated with the pyrolytic reactions of the excess K1.

The presence of K1 in the solid product will ensure the reusability of the catalyst. There are some studies indicating that the catalyst must be separated from the char for reusability [43]. On the other hand, some studies in the literature emphasize that pyrolysis chars themselves can be used as catalysts [44–46]. Moreover, the effectiveness of char and CaO together as a catalyst has also been emphasized in the literature [47]. Another common application for pyrolysis solid product is biochar derived from coprolysis holds promise as soil amendment [1]. In the light of this information, two alternative approaches can be mentioned: the separation of char and K1 structures of solid products; or the use of the solid product as it is.

Some preliminary experiments have been carried out for the separation of K1 and carbon part of pyrolysis solid products. It was put into water, mixed in an ultrasonic bath and left to settle; the particles started to settle in a short time as seen in Fig. 7. During settling, the white K1 particles, which were heavier than the carbon structures, first settled at the bottom and the carbon structures formed a black layer phase on top. Although it is important for this situation to appear as in Fig. 7 in 50 seconds in terms of ease of separation, it is highly likely that the other structure will remain, especially between the particle pores during this separation. For this reason, it was evaluated that a short-term ultrasound pretreatment would be beneficial.

3.4. PET/PP+OP+K1 catalytic co-pyrolysis oil product characteristics

The calorific values of the pyrolytic liquid products obtained under other conditions were presented in Table 2.

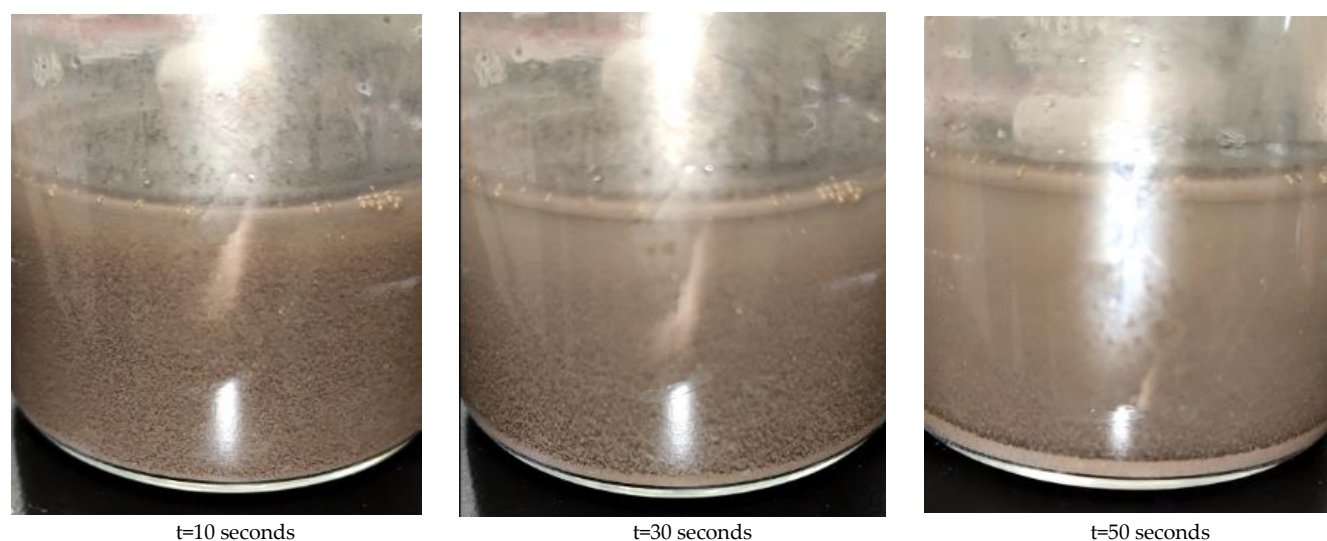


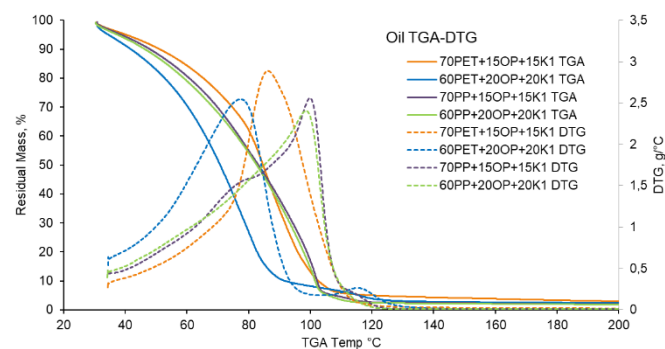
Figure 7. Separation of pyrolysis solid products as they precipitate in water

Table 2. Catalytic co-pyrolysis liquid product calorific values at 500 °C

Mixture, %			Tar/Oil Heat value (cal/g)
60PET	20OP	20K1	N/A (oil not produced)
70PET	15OP	15K1	36.2 (oil) 4448 (oligomer)
60PP	20OP	20K1	9340
70PP	15OP	15K1	10147

Separate measurements were made for the oligomer and oil product obtained under the 70PET+15OP+15K1 condition. The calorific values of the liquid product for PP+20K1 and OP+20K1 pyrolysis at 500 °C were found to be 10147 cal/g and 154.3 cal/g, respectively [29,30]. Approximately 10000 cal/g calorific value was measured in PP+OP+K1 pyrolysis liquid products. It was seen in Fig. 2 that the catalytic co-pyrolysis mixtures provided high amounts of liquid product in the presence of PP. In this case, it was shown that catalytic co-pyrolysis with PP provided higher performance in terms of both quantity and thermal content in the liquid product.

The thermal resistances of the liquid products obtained from PET/PP+OP+K1 catalytic co-pyrolysis were presented in Fig. 8. The curves were quite close to each other. However, the difference in the location of the peak point in the DTG curves shows the difference in the degradation reaction. All liquid products started to decompose at very low temperatures and were exhausted before reaching 200 °C, leaving no residue. The fact that the decomposition started at 30–35 °C can be interpreted as the presence of excessive volatile components in the liquid product. While the IDT and SDT values of the liquid product for PET decrease with the increase in the K1 and OP amounts, the opposite is the case for PP. The reason for this increase in PP can be explained by the fact that the increasing K1 dose creates lower molecular weight groups in PP depolymerization. For both K1 doses, the T_5 , T_{10} and T_{50} values were quite close to each other. The fact that the syringyl rings in the lignin structure of OP were reduced and that it becomes more stable in terms of degradation also supports the increase in thermal resistance seen in the TGA curves of PP chars.



Mixture, %			Tonset, °C *	Tend, °C **	T_5 , °C	T_{10} , °C	T_{50} , °C
60PET	20OP	20K1	36	123	40	51	85
70PET	15OP	15K1	35	105	35	42	71
60PP	20OP	20K1	36	106	39	48	83
70PP	15OP	15K1	39	110	37	46	82

Figure 8. TGA-DTG curves and thermogravimetric findings of catalytic co-pyrolysis liquids of PP/PET blends with OP and K1

Volatile components have an important role in these liquid products with low thermal resistance (Fig. 8). Chemical structures were evaluated via FTIR spectra (Fig. 9). The oil product of 60PET+20OP+20K1 condition was in too low quantity to characterize. In the FTIR spectrum of the catalytic co-pyrolysis liquid of 70PET+15OP+15K1 and 60%PP+20OP+20K1 mixtures, OH group at 3322 cm^{-1} , alkyne group at 2161 cm^{-1} , aryl substituted C=C at 1634 cm^{-1} , $-\text{CH}_3$ group at 1386 cm^{-1} , vinylidene group C-H or aromatic ether aryl-O stretching at 1278 cm^{-1} were observed. These results showed that the liquid product contains mainly olefinic and aromatic hydrocarbons and oxygenated compounds such as paraffinic and alcohol. According to the GC-MS scans performed to detect this, the liquid product formed by the 70%PET+15OP+15K1 catalytic co-pyrolysis contains alkane, alkene, acid, phenol, benzene, aldehyde, ester, alcohol, ketone and other organic compound groups (Fig. 10). Benzene groups with higher carbon numbers were formed as a result of the condensation of alkene groups in the gas product in the liquid product and were richer in terms of the number of compounds compared to other groups. CaO can react with acids and other carboxyl groups to form calcium carboxylates which would decompose at higher temperatures to form linear ketones, CO_2 and H_2O . As a result, the ketones content of pure CaO increased [4]. While Propanoic acid ($\text{C}_3\text{H}_6\text{O}_2$), Oxalic acid ($\text{C}_2\text{H}_2\text{O}_4$) and Benzoic acid ($\text{C}_7\text{H}_6\text{O}_2$) were the acid compounds encountered, the presence of alcohol and its derivatives in the highest number and variety in pyrolysis liquids can be mentioned. Ethanol, 2-chloro-, acetate ($\text{C}_2\text{H}_5\text{OH}$), Mequinol ($\text{C}_7\text{H}_8\text{O}_2$); 1-Heptanol, 2,4-diethyl ($\text{C}_9\text{H}_{20}\text{O}$); 2-Isopropyl-5-methyl-1-heptanol ($\text{C}_{11}\text{H}_{24}\text{O}$); Tridecanol ($\text{C}_{13}\text{H}_{28}\text{O}$) were observed as important alcohol compounds and Benzene (C_6H_6), Dotriacontyl pentafluoropropionate ($\text{C}_{35}\text{H}_{65}\text{F}_5\text{O}_2$), Nonadecyl heptafluorobutyrate ($\text{C}_{23}\text{H}_{39}\text{F}_7\text{O}_2$) were observed as benzene group (Fig. 11). Consistent with the literature, both the plastics, and biomass polymers crack to produce small compounds involving short chain alkenes and furan derivatives from cellulose and hemicellulose which then react together to produce nonoxygenated aromatic compounds [24]. It can be said that the calorific value of these liquids is higher due to the presence of more components in alkane and alkene groups in the liquid product composition obtained from the catalytic co-pyrolysis of PET waste compared to the liquid product obtained from the catalytic co-pyrolysis of PET waste (Table 2).

3.5. PET/PP+OP+K1 catalytic co-pyrolysis gas product compositions

Considering the distribution of pyrolysis products (Fig. 2), the gas product of the catalytic co-pyrolysis condition, which can produce the highest amount of

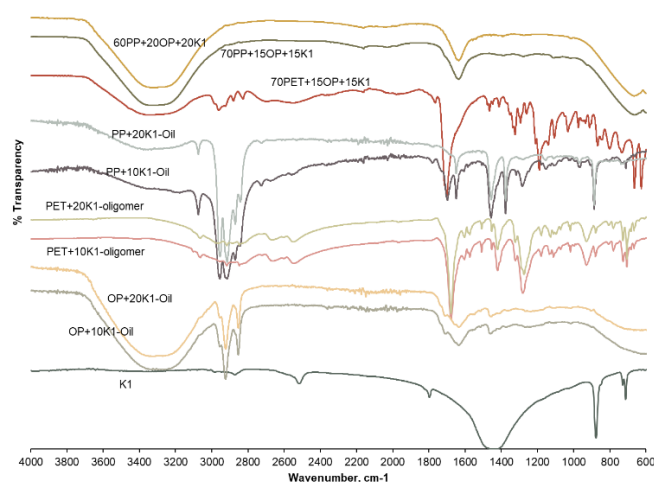


Figure 9. FTIR spectra of PET/PP+OP+K1 no-hold catalytic co-pyrolysis liquids

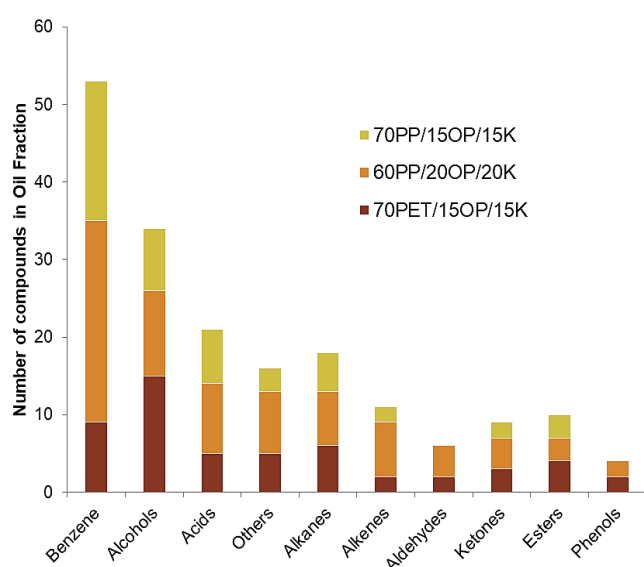


Figure 10. Organic composition of liquid products obtained from catalytic co-pyrolysis of PET/PP waste with OP and K1

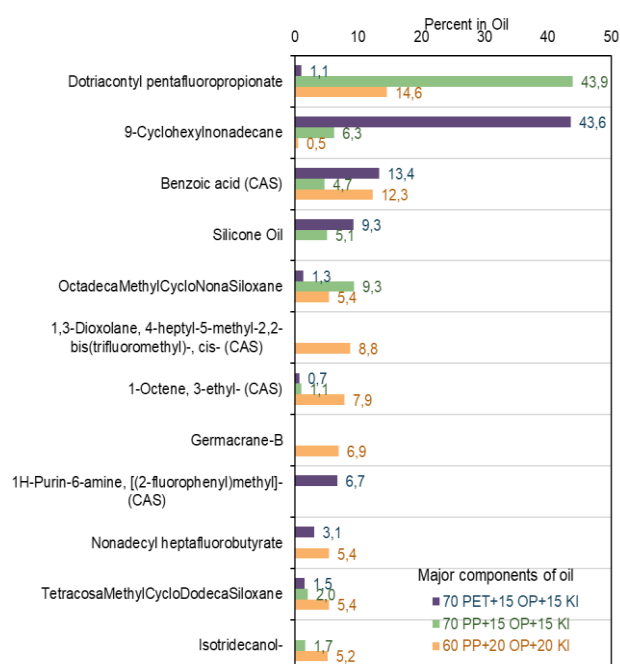


Figure 11. Major components of co-pyrolysis liquids

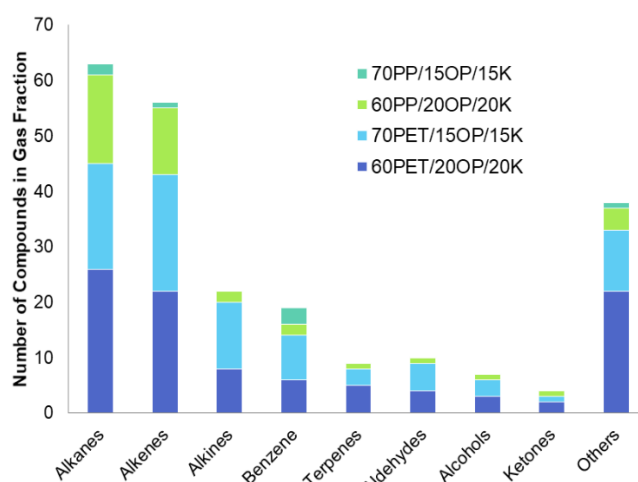


Figure 12. Organic composition of gaseous products obtained from catalytic co-pyrolysis of PET/PP waste with OP and K1

gaseous product, was also the product with the highest component diversity (Fig. 12). In the case of higher OP and K1 doses in PET catalytic co-pyrolysis, an increment in the number of alkane, alkene, terpene and ketone group compounds was also observed. The alkane compounds observed in the majority of the pyrolysis gases obtained with different OP and K1 doses of PET waste were Hexane 2-methyl (C_7H_{16}), Cyclohexane methyl (C_7H_{14}), Cyclopentane ethyl (C_7H_{14}), Cyclobutane (1-methylethylidene) (C_7H_{12}), Heptane 4-methyl (C_8H_{18}), Cyclopentane 1,2,3-trimethyl (C_8H_{16}), Octane (C_8H_{18}), Heptane 3,4,5-trimethyl ($C_{10}H_{22}$), Cyclohexane 1,3,5-trimethyl (C_9H_{18}), Decane ($C_{10}H_{22}$) (Fig. 12 and Fig. 13). In these pyrolysis experiments, the carbon numbers of the gases with a high frequency varied between 7-10 (C_7 - C_{10}), while the carbon numbers of the gases observed rarely were higher (Fig. 12). Again, with the increase in OP and K1 doses for PET, the presence of the same alkene group compounds was detected.

Although the carbon numbers of alkenes in gases generally vary between 5-12 (C_5 - C_{12}), the vast majority have 7 and 8 (C_7 - C_8) carbons. Compared to alkane compounds, the carbon numbers of alkenes in gases were lower. In addition to alkane and alkene compounds, other aliphatic groups found in pyrolysis gas were alkynes. Although alkyne groups do not have a wide range of diversity as much as alkanes and alkenes, the most common compounds in PET/OP/K1 catalytic co-pyrolysis gas are 1,1'-Bicyclohexyl and 1-Cyclohexyl-1-propyne. New alkane, alkene, alkyne, terpene, aldehyde, alcohol and ketone group compounds were observed with the increase of OP and K1 doses in PP catalytic co-pyrolysis (Fig. 12). The carbon numbers of alkene compounds observed in the pyrolysis gases of PP+K1 mixtures are between 2 and 13 (C_2 - C_{13}). When the compositions of the liquid and gas products of catalytic co-pyrolysis are compared with each other, benzene, acid and alcohol groups were predominant in liquids, while alkane, alkene and alkyne groups were dominant in gases.

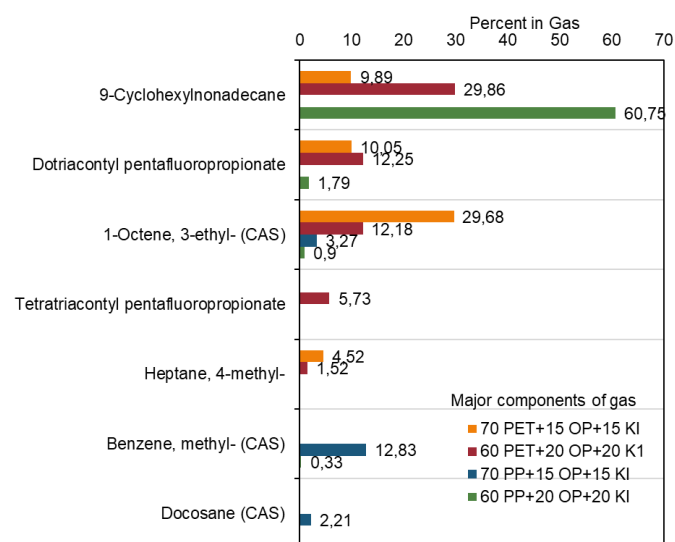


Figure 13. Major components of co-pyrolysis gases

The density of the pyrolysis gas of co-pyrolysis was compared in the Fig. 14. In catalytic co-pyrolysis experiments, as the plastic ratios in both PET+OP+K1 and PP+OP+K1 mixtures increase, the density of the gas product decreases (Fig. 14). The higher density in both in the presence of 60% plastic was related to the fact that the number and variety of compounds in the gas product were higher compared to the mixtures with 70% plastic. In these pyrolysis experiments, the carbon numbers of the gases with a high frequency of observation varied between 7–10 (C7–C10), while the carbon numbers of the rarely observed gases were higher. Compared to the catalytic pyrolysis findings, high carbon numbers and high-density values were decisive in the density of the compound carbon numbers.

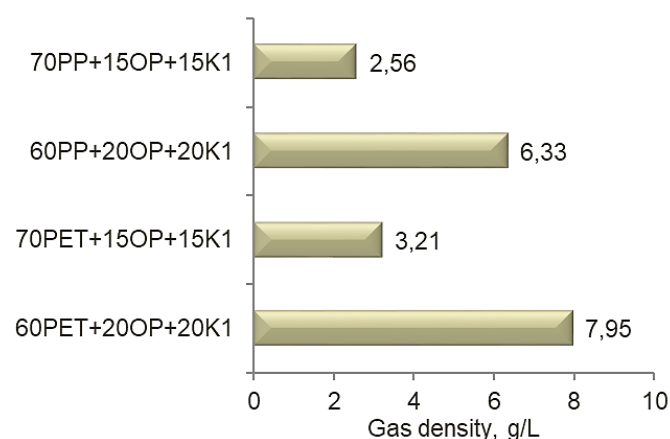


Figure 14. Comparison of the densities of pyrolysis gases obtained by PET/PP+OP catalytic co-pyrolysis

4. Conclusion

In this study, wastes of three different structures were symbiotically recycled via catalytic co-pyrolysis. Two types of polymers (PET and PP) were co-pyrolyzed with lignocellulosic biomass (olive pomace) together with catalytic contribution of marble processing effluent

treatment sludge (K1). The effect of plastic type and pyrolyzed material mixture ratio on pyrolysis fractions were investigated. Waste PET or PP can be thermally degraded together with OP and K1 via catalytic co-pyrolysis. While pyrolytic liquid product was dominant for 70%PP+15%OP+15%K1 mixture, much more pyrolytic gas fraction was produced in the pyrolysis of 60%PET+20%OP+20%K1. The thermal stability of char fractions reveals the potential of the char to be used in alternative areas as a material with high thermal resistance, for example, as adsorbent, cathodic electrode production, in compost or in composite. The studies on the details of the conditions of char evaluation and utilization are recommended as further studies.

The catalytic co-pyrolysis liquid products contained benzene, alcohols, acids dominantly. High number of group components in the liquid product resulted in the higher calorific value, indicating the potential of fuel production. Dotriacontyl pentafluoropropionate, 9-Cyclohexylnonadecane, Benzoic acid, 1-Octene3-Ethyl and Methyl benzene were the chemicals that had the highest recovery potential from catalytic co-pyrolysis fluid fractions. Each of these potentially recoverable chemicals were important feedstock chemicals in diverse number of industries including cosmetics, chemicals etc. The most important output of this study was investigating the potential recovery products via processing of three different types of wastes together. This will help reducing carbon footprint, contribute to achieve circular economy and increasing sustainability. As further studies, the separation and purification technologies for these chemicals need to be studied under the criteria of low energy and material consumption and low cost.

Acknowledgement:

This study was financially supported by the Bilateral Joint Research Project between TUBITAK (Turkey) [CAYDAG-118Y475] and JSPS (Japan) [JPJSBP12019942].

References

- [1] D.T.Sekyere, J. Zhang, Y. Chen, Y. Huang, M. Wang, J. Wang, N. Niwamanya, A. Baridye, Y. Tian, Production of light olefins and aromatics via catalytic co-pyrolysis of biomass and plastic, *Fuel*, 333, 2023, 126339.
- [2] N. Sánchez-Ávila, A. Cardarelli, M. Carmona-Cabello, M.P. Dorado, S. Pinzi, M. Barbanera, Kinetic and thermodynamic behavior of co-pyrolysis of olive pomace and thermoplastic waste via thermogravimetric analysis, *Renew. Energ.* 230, 2024, 120880.
- [3] Z. Murti, D. Dharmawan, S. Siswanto, D. Soedjati, A. Barkah, P. Rahardjo, Review of the circular economy of plastic waste in various countries and potential applications in Indonesia, *IOP Conf. Ser. Earth Environ. Sci.*, 2022,

- [4] R. Aguado, A. Escámez, F. Jurado, D. Vera, Experimental assessment of a pilot-scale gasification plant fueled with olive pomace pellets for combined power, heat and biochar production. *Fuel*, 344, 2023, 128127.
- [5] M.S. Qureshi, A. Oasmaa, H. Pihkola, I. Deviatkin, A. Tenhunen, J. Mannila, H. Minkkinen, M. Pohjakallio, J. Laine-Ylijoki, Pyrolysis of plastic waste: Opportunities and challenges, *J Anal Appl Pyrol*, 152, 2020, 104804.
- [6] A.L.K. Chee, B.L.F. Chin, S.M.X. Goh, Y.H. Chai, A.C.M. Loy, K.W. Cheah, C.L. Yiin, S.S.M. Lock, Thermo-catalytic co-pyrolysis of palm kernel shell and plastic waste mixtures using bifunctional HZSM-5/limestone catalyst: Kinetic and thermodynamic insights, *J Energy Inst*, 107, 2023, 101194.
- [7] J. Choudhary, B. Alawa, S. Chakma, Insight into the kinetics and thermodynamic analyses of co-pyrolysis using advanced isoconversional method and thermogravimetric analysis: a multi-model study of optimization for enhanced fuel properties, *Process Saf Environ* 173, 2023,
- [8] S.Y. Oh, Y.D. Seo, Polymer/biomass-derived biochar for use as a sorbent and electron transfer mediator in environmental applications, *Bioresour Technol*, 218, 2016, 77–83.
- [9] F. Abnisa, W. M. A. W. Daud, A review on co-pyrolysis of biomass: an optional technique to obtain a high-grade pyrolysis oil. *Energy Convers Manage*, 87, 2014, 71–85.
- [10] Z. Wang, K.G. Burra, T. Lei, A.K. Gupta, Co-pyrolysis of waste plastic and solid biomass for synergistic production of biofuels and chemicals-A review, *Prog Energy Combust*, 84, 2021, 100899.
- [11] A.C. Johansson, L. Sandström, O.G. Öhrman, H. Jilvero, Co-pyrolysis of woody biomass and plastic waste in both analytical and pilot scale, *J Anal Appl Pyrol*, 134, 2018, 102–113.
- [12] K. Yang, K. Wu, F. Li, L. Jia, S. Wang, H. Zhang, Investigation on the co-pyrolysis of bamboo sawdust and low-density polyethylene via online photoionization mass spectrometry and machine learning methods, *Fuel Process Technol* 240, 2023,
- [13] G. Özsin, A.E. Pütün, A comparative study on co-pyrolysis of lignocellulosic biomass with polyethylene terephthalate, polystyrene, and polyvinyl chloride: Synergistic effects and product characteristics, *J Clean Prod*, 205, 2018, 1127–1138.
- [14] F.A. Al-Balushi, K.G. Burra, Y. Chai, M. Wang, Co-pyrolysis of waste tyre and pine bark: Study of reaction kinetics and mechanisms. *Biomass Bioenergy*, 16T8, 2023, 106654.
- [15] J. Chattopadhyay, T.S. Pathak, R. Srivastava, A.C. Singh, Catalytic co-pyrolysis of paper biomass and plastic mixtures (HDPE (high density polyethylene), PP (polypropylene) and PET (polyethylene terephthalate)) and product analysis, *Energy*, 103, 2016, 513–521.
- [16] A.C. Dyer, M.A. Nahil, P.T. Williams, Catalytic co-pyrolysis of biomass and waste plastics as a route to upgraded bio-oil, *J Energy Inst*, 97, 2021, 27–36.
- [17] K.G. Burra, A.K. Gupta, Kinetics of synergistic effects in co-pyrolysis of biomass with plastic wastes, *Appl Energy*, 220, 2018, 408–418.
- [18] P. Lu, Q. Huang, A.T. Bourtsalas, Y. Chi, J. Yan, Synergistic effects on char and oil produced by the co-pyrolysis of pine wood, polyethylene and polyvinyl chloride, *Fuel*, 230, 2018, 359–367.
- [19] M.V. Navarro, J.M. L'opez, A. Veses, M.S. Call'en, T. García, Kinetic study for the copyrolysis of lignocellulosic biomass and plastics using the distributed activation energy model, *Energy*, 165, 2018, 731–42.
- [20] J.R. Kim, J.H. Yoon, D.W. Park, Catalytic recycling of the mixture of polypropylene and polystyrene, *Polym Degrad Stab*, 76(1), 2002, 61–67.
- [21] S. Kumagai, I. Hasegawa, G. Grause, T. Kameda, T. Yoshioka, Thermal decomposition of individual and mixed plastics in the presence of CaO or Ca(OH)₂, *J Anal Appl Pyrol*, 113, 2015, 584–590.
- [22] S. Gopinath, P.K. Devan, K. Pitchandi, Production of pyrolytic oil from ULDP plastics using silica-alumina catalyst and used as fuel for DI diesel engine, *RSC Adv*, 10(61), 2020, 37266–37279.
- [23] H. Hassan, J.K. Lim, B.H. Hameed, Recent progress on biomass co-pyrolysis conversion into high-quality bio-oil, *Bioresource Technol*, 221, 2016, 645–655.
- [24] X. Zhang, H. Lei, S. Chen, J. Wu, Catalytic co-pyrolysis of lignocellulosic biomass with polymers: a critical review. *Green Chem*, 18(15), 2016, 4145–4169.
- [25] B. Muneer, M. Zeeshan, S. Qaisar, M. Razzaq, H. Iftikhar, Influence of in-situ and ex-situ HZSM-5 catalyst on co-pyrolysis of corn stalk and polystyrene with a focus on liquid yield and quality, *J Clean Prod*, 237, 2019, 117762.
- [26] F. Mo, H. Ullah, N. Zada, A.A. Shahab, Review on Catalytic Co-Pyrolysis of Biomass and Plastics Waste as a Thermochemical Conversion to Produce Valuable Products, *Energies*, 16, 2023, 5403.
- [27] V. Onen, A. Ozgan, G. Goktepli, M. Kalem, G. Ahmetli, E. Yel, Marble processing effluent treatment sludge in waste PET pyrolysis as catalyst-I: pyrolysis product yields and the char characteristics, *Int J Environ Sci Technol*, 20(4), 2023, 3965–3986.
- [28] G. Ahmetli, A. Ozgan, V. Onen, M. Kalem, G. Goktepli, E. Yel, Marble processing effluent treatment sludge in waste poly (ethylene terephthalate) pyrolysis as catalyst-II: recovery from pyrolytic fluids, *Int J Environ Sci Technol*, 21(7), 2024, 6021–6042.
- [29] G. Goktepli, A. Ozgan, V. Onen, G. Ahmetli, M. Kalem, E. Yel, Alternative green application areas for olive pomace catalytic pyrolysis biochar obtained via marble sludge catalyst. *Biodegradation*, 35, 2024, 907–938.
- [30] E. Yel (Director), Development of upgrade recycle system by environmental-benign functional materials using waste materials (marble sludge and olive oil wastes) in Turkey, Tübitak-JSPS Joint Research Programs, Bilateral JRP Final Report, 2022.
- [31] D. Duan, H. Lei, Y. Wang, R. Ruan, Y. Liu, L. Ding, Y. Zhang, L. Liu, Renewable phenol production from lignin with acid pretreatment and ex-situ catalytic pyrolysis, *J Clean Prod*, 231, 2019, 331–340.
- [32] X. Chen, Y. Chen, H. Yang, W. Chen, X. Wang, H. Chen, Fast pyrolysis of cotton stalk biomass using calcium oxide, *Bioresource Technol*, 233, 2017, 15–20.
- [33] G. Grause, S. Matsumoto, T. Kameda, T. Yoshioka, Pyrolysis of Mixed Plastics in a Fluidized Bed of Hard Burnt Lime, *Ind. Eng. Chem. Res.* 50(9), 2011, 5459–5466.
- [34] S. Kumagai, I. Hasegawa, G. Grause, T. Kameda, T. Yoshioka, Thermal decomposition of individual and mixed plastics in the presence of CaO or Ca(OH)₂, *J Anal Appl Pyrol* 113(2015), 584–590.
- [35] H. Gulab, K. Hussain, S. Malik, Z. Hussain, & Z. Shah. Catalytic co-pyrolysis of E Crassipes biomass and polyethylene using waste Fe and CaCO₃ catalysts. *Int J Energy Res*, 40(7), 2016, 940–951.
- [36] T. A. Vo, H. V. Ly, I. Hwang, H. T. Hwang, J. Kim, & S. S. Kim, Enhancement of biofuel quality via conventional and catalytic co-pyrolysis of bamboo with polystyrene in a bubbling fluidized bed reactor: Coupled experiments and artificial neural network modeling. *Fuel*, 346, 2023, 128403.
- [37] Y. Tang, J. Dong, Y. Zhao, G. Li, Y. Chi, E. Weiss-Hortala, ... & C. Ye, Hydrogen-rich and clean fuel gas production from Co-pyrolysis of biomass and plastic blends with CaO additive. *ACS omega*, 7(41), 2022, 36468–36478.
- [38] A. Alcazar-Ruiz, F. Dorado, L. Sanchez-Silva, Fast pyrolysis of agroindustrial wastes blends: Hydrocarbon production enhancement, *J Anal Appl Pyrol*, 157, 2021, 105242.
- [39] F. Abnisa, P.A. Alaba, Recovery of liquid fuel from fossil-based solid wastes via pyrolysis technique: A review, *J Environ Chemical Eng*, 9(6), 2021, 106593.

- [40] B. Saha, P.K. Reddy, A.C.K. Chowlu, A.K. Ghoshal, Model-free kinetics analysis of nanocrystalline HZSM-5 catalyzed pyrolysis of polypropylene (PP), *Thermochim Acta*, 468(1-2), 2008, 94–100.
- [41] C. Covarrubias, F. Gracia, H. Palza, Catalytic degradation of polyethylene using nanosized ZSM-2 zeolite, *Appl Catal A-Gen*, 384(1-2), 2010, 186–191.
- [42] K. Al bkoor Alrawashdeh, K. Slopicka, A.A. Alshorman, P. Bartocci, F. Fantozzi, Pyrolytic degradation of olive waste residue (OWR) by TGA: thermal decomposition behavior and kinetic study, *J Energ Power Eng*, 11(8). 2017, 497–510.
- [43] J.Shah, M.R. Jan, Z. Hussain, Catalytic pyrolysis of low-density polyethylene with lead sulfide into fuel oil, *Polym Degrad Stab*, 87(2), 2005, 329–333.
- [44] A.S. Al-Rahbi, J.A. Onwudili, P.T. Williams, Thermal decomposition and gasification of biomass pyrolysis gases using a hot bed of waste derived pyrolysis char, *Bioresource Technol*, 204, 2016, 71–79.
- [45] D.Q. Fu, X.H. Li, W.Y. Li, J. Feng, Catalytic upgrading of coal pyrolysis products over bio-char, *Fuel Process Technol*, 176, 2018, 240–248.
- [46] K.Sun, N.J. Themelis, A.T. Bourtsalas, Q. Huang, Selective production of aromatics from waste plastic pyrolysis by using sewage sludge derived char catalyst, *J Clean Prod*, 268, 2020, 122038.
- [47] H.Weldekidan, V. Strezov, T. Kan, R. Kumar, J. He, G. Town, Solar assisted catalytic pyrolysis of chicken-litter waste with in-situ and ex-situ loading of CaO and char, *Fuel*, 2019, 246, 408–416.



Determination of heavy metals and pesticide residue in soil, plant and water using QuEChERS method and design of experiment along Asa-River Tributary

S.W. Olokoba* 

Kwara State University, Department of Chemistry and Industrial Chemistry, Malete, PMB 1530, Ilorin, Kwara State, Nigeria.

Abstract

The QuEChERS sample preparation method, coupled with gas chromatography-mass spectrometry (GC-MS), was optimized and validated for pesticide determination in soil, water, and vegetables. Experimental parameters, such as mass of sample, volume of solvents, extraction time, and sorbents, were optimized using Minitab statistical software. The GC-MS method showed excellent linearity, selectivity, and recovery, with detection limits ranging from $>0.001 \mu\text{g/L}$ and quantification limits from $0.003 \mu\text{g/L}$. The analysis of pesticide samples revealed 17 identified pesticides, with Endosulfan ether showing the highest residue concentration (1.41 mg/L) in soil Sample 2. Similar trends were observed in Vegetable Samples 1 and 2, with residue concentrations ranging from $0.00\text{--}870.0 \mu\text{g/kg}$ and $0.00\text{--}110.00 \mu\text{g/kg}$, respectively. No pesticide residues were detected in soil Sample 1, water Samples 3 and 4. Additionally, heavy metal analysis (Cd, Pb, Zn, Cu, Ni, Co, As, and Fe) was conducted using Atomic Absorption Spectroscopy (AAS) on soil, water, and vegetable samples collected from Asa-river farmland. The results showed variations in metal content across samples, exceeding WHO guidelines, except for cadmium in water and plant samples and nickel in Soil Samples 4 and 6. These methods offer favorable toxicological, environmental, and economic benefits, making them ideal for routine monitoring of pesticides and heavy metals in agricultural farm products.

Keywords: Design of experiment, heavy metals, pesticide residues, pollution, QuEChERS

1. Introduction

The rapid industrialization, urbanization, and intensification of agricultural practices have led to unprecedented environmental pollution with heavy metals and organic pollutants, such as pesticides. Since the 1940s, the migration rate of these pollutants has increased dramatically, posing significant environmental and health risks [1]. Heavy metal pollution, in particular, has become a major concern due to its harmful effects on ecosystems and human health [2]. Agricultural and industrial activities have compromised natural resources, including soil and water, in many countries. Industrial processes have contributed substantially to elevated concentrations of heavy metals in the environment [3]. These pollutants persist in water, plants, soil, and ultimately, food, leading to adverse human health effects, including carcinogenic and non-carcinogenic risks [4]. Furthermore, exposure to contaminated underground water resources poses significant health risks [5]. The persistence and bioaccumulation of heavy metals and organic pollutants in the environment necessitate urgent

attention and effective mitigation strategies to protect human health and ecosystem integrity.

Pesticides are chemical compounds, natural or synthetic, used to control, prevent, or destroy crop pests and vectors of plant diseases. These organic compounds comprise various functional groups and isomeric forms, playing a crucial role in agricultural pest management [6]. The use of pesticides has led to significant increases in food production, improved quality, and reduced incidence of insect-borne diseases. However, the substantial growth in pesticide use has raised concerns about their toxicity [7]. Despite the benefits, occupational and accidental exposure to pesticides has been linked to chronic health effects, including endocrine disorders, blood disorders, and genetic changes. It is essential to address the risks associated with pesticide exposure and explore safer alternatives [4].

The QuEChERS (Quick, Easy, Cheap, Effective, Rugged, and Safe) extraction method is a widely accepted technique for analyzing pesticide residues in food chains, particularly fruits and vegetables [8]. This

Citation: S.W. Olokoba, Determination of heavy metals and pesticide residue in soil, plant and water using QuEChERS method and design of experiment along Asa-River Tributary, Turk J Anal Chem, 7(1), 2025, 46–54.

***Author of correspondence:** sulemanolokoba@gmail.com

Tel: +23488165086181

Fax: N/A

Received: November 11, 2024

Accepted: January 25, 2025

 <https://doi.org/10.51435/turkjac.1583276>

method involves a five-step process: crushing the sample, using acetonitrile for extraction and separation, adding MgSO_4 and other salts to remove water, and utilizing adsorbents to remove impurities by leveraging interactions between adsorbent fillers and matrix impurities. Finally, the supernatant is analyzed using GC-MS and LC-MS. According to [9], QuEChERS is ideal for multi-class and multi-residue analysis of pesticide residues.

Design of Experiment (DOE) is a chemometric approach that optimizes experimental conditions by identifying significant factors, estimating main and interaction effects, and minimizing experimental runs. This efficient approach streamlines experimentation, reducing analysis time and enhancing sample throughput [10]. This study aims to develop a Quick, Easy, Cheap, Effective, Rugged, and Safe (QuEChERS) method for analyzing pesticides and digestion methods for heavy metals in plant, soil, and water samples. Specifically, Placket-Burman Design (PBD) and Central Composite Design (CCD) are employed to determine the critical factors influencing the effective and efficient extraction of multiclass pesticide residues in vegetables, soil, and water.

2. Materials and methods

2.1. Sample collection and preparation

The accurate analysis of heavy metals and pesticides in environmental samples requires a systematic and precise approach to sample collection and preparation (Fig. 1).

Soil: Three (3) soil samples were collected using soil augers or corers at 15 cm depths, ensuring representation across the study area. Multiple samples were collected from each location to account for spatial variability and air dried. The collected soil samples were grinded in a mortar with pestle to fineness and sieved thoroughly. The collected soil samples were grinded in a mortar with pestle to fineness and sieved thoroughly. Then 2.00 g was weigh using weighing balance with sensitivity of (0.001 mg), and the sieved samples was subjected to QuEChERS and wet acid digestion procedures which were done in the laboratory.

Plants: Three (3) plant samples of *Amaranthus hybridus* were carefully collected, considering factors such as growth stage, and potential for bioaccumulation of contaminants. The collected vegetable samples were blended and homogenized, then 2.00 g was weigh using weighing balance with sensitivity of (0.001 mg) and were subjected to QuEChERS and wet acid digestion procedures.

Water: Three (3) water samples were collected from the river used to irrigate the vegetables. The water samples were collected at various depths and sufficient volume was collected for the analysis and it been kept inside a clean container.

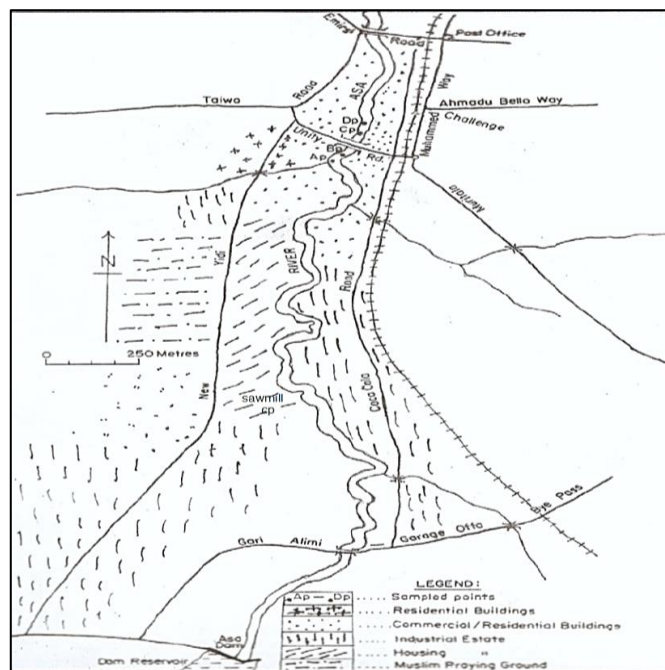


Figure 1. A geographical map of Asa River segment showing study area

2.2. QuEChERS procedure

A sample preparation protocol was employed to extract and clean up the samples. For soil and vegetable samples, 2.00 g of each was transferred to a 20 mL centrifuge tube, while 2.00 mL of water sample was used. Acetonitrile (10 mL) was added to each sample, and the mixture was vortexed for 1 minute. This extraction step was repeated with an additional 10 mL of acetonitrile. Next, a mixture of salts and an internal standard was added to the sample. Specifically, 6 g of MgSO_4 , 1.5 g of sodium chloride, 1 g of sodium citrate, and 100 μL of triphenyl phosphate (20 $\mu\text{g}/\text{mL}$) were added. The mixture was vigorously stirred for 1 minute and then centrifuged at 4000 rpm for 5 minutes. Following centrifugation, 6 mL of the supernatant was transferred to a Supel QuEchSPE kit (55437-U) containing 900 mg of MgSO_4 and 150 mg of primary-secondary amine (PSA). The mixture was then centrifuged again at 4000 rpm for 5 minutes.

Finally, 5 mL of the supernatant was acidified with 50 μL of 5% formic acid (10 $\mu\text{L}/\text{mL}$ of extract) in acetonitrile. The resulting extract was analyzed using GC-MS, adhering to the QuEChERS method and EN 15662-2008 guidelines.

2.3. GC-MS analysis

The analysis was performed using a (Shimadzu QP2010 Series) GC-MS system operated in split/splitless mode at an injection temperature of 270 °C. Separation of target analytes was achieved on a DB-5MS fused capillary column (30 m x 0.25 mm i.d. x 0.25 µm film thickness) composed of 5% diphenyl and 95% dimethylpolysiloxane.

The gas chromatography (GC) instrument conditions were optimized for the analysis. A high-pressure Merlin Microseal septumless injection kit and a salinized narrow bore liner (78.5 mm x 6.5 mm o.d. x 0.75 mm i.d.) were used. Helium served as the carrier gas, maintained at a constant flow rate of 1.3 mL/min and linear velocity of 42 cm/sec. The GC column oven temperature program was carefully designed to ensure optimal separation and detection. The temperature program consisted of an initial hold at 60 °C for 2 minutes, followed by a series of ramps: 30 °C/min to 180 °C, 3 °C/min to 210 °C, and 20 °C/min to 280 °C. The final temperature was held for 5 minutes, resulting in a total runtime of 24.50 minutes. The MS operating conditions included a transfer line temperature of 300 °C, ion source temperature of 200 °C, and electron ionization (EI) of 70 eV. Method optimization was performed in scan mode, while quantitation was done in selected ion monitoring (SIM) mode. A target ion (most abundant ion) and two reference ions were monitored for each target analyte. Pesticide identification was achieved by matching retention times with standards, comparing relative abundance, and matching mass spectra with the NIST library. The NIST library provided a list of best matches based on abundant mass-to-charge ratios, enabling identification of pesticides [11].

2.4. Validations of the methods

The validation was carried out according to EU commission Detection. The method performance was evaluated by the following parameters: matrix effect study, establishment of matrix – matched calibration, limit of detection (LOD).

2.5. Digestion of samples

A modified digestion method was employed for preparing soil, water, and vegetable samples for Atomic Absorption Spectroscopy (AAS) analysis. Soil sample digestion was performed using a combination of heat and acid treatment. Specifically, 1 g of oven-dried soil sample was placed in a 250 mL digestion tube, and 10 mL of concentrated nitric acid (HNO₃) was added. The mixture was initially heated at 90 °C for 45 minutes, followed by an increase in temperature to 150 °C, where it was boiled for 6 hours until a clear solution was obtained. During the digestion process, an additional 5

mL of concentrated HNO₃ was added at least three times to facilitate complete digestion. The process continued until the volume of the solution was reduced to approximately 1 mL. After digestion, the interior walls of the tube were rinsed with distilled water, and the contents were thoroughly mixed to prevent sample loss. Once cooled, 5 mL of 1% HNO₃ was added, and the solution was filtered sequentially through Whatman No. 42 paper and 0.45 µm Millipore membrane filters. The filtered solution was then transferred to a 100 mL volumetric flask and diluted to the mark with distilled water.

For water sample digestion, 5 mL of concentrated HNO₃ was added to 100 mL of the water sample, and the mixture was evaporated on a hot plate to a final volume of 20 mL. After cooling, another 5 mL of concentrated HNO₃ was added, covered with a watch glass, and refluxed for 25 minutes. The mixture was then heated on a hot plate while adding concentrated HNO₃ until it became light in color and clear. The beaker wall and watch glass were rinsed thoroughly with distilled water, and the resulting digest was filtered through Whatman No. 1 filter paper into a 100 mL volumetric flask and made up to the mark with distilled water.

Vegetable sample digestion involved weighing 2 g of sample into a beaker, adding 10 mL of analytical-grade nitric acid, covering with a watch glass, and cold soaking for 30 minutes. The beaker was then heated to 120 °C for 2 hours, cooled to room temperature, and transferred to a 100 mL volumetric flask. The digest was made up to the mark with distilled water. The resulting digests were subjected to AAS analysis.

2.6. AAS measurement

The instrument was calibrated with NIST heavy metal standards. Blank solutions were run with each digestion to check for interference and contamination. Heavy metal concentrations are reported as mg/kg dry weight (soil and food) or mg/L (water). All samples were analyzed in triplicate.

2.7. Statistical analysis

All experiment data was carefully analyzed using MINITAB version 17 statistical software. Microsoft excel was used for the calculation of standard deviation of mean and relative standard deviation. Significant differences between concentrations of the heavy metals following the digestion methods were analyzed by ANOVA using SPSS statistical software (Version 20). Statistical significance was defined as $p < 0.05$.

2.8. Design of the experiment

In analytical chemistry, Design of Experiment (DOE) plays a crucial role in optimizing key factors, ultimately

enhancing the performance of analytical methods, processes, and products. DOE facilitates the understanding of main interaction effects between factors and models the relationships between factors and responses, all while minimizing the number of experiments required. There are two primary DOE approaches: univariate, which optimizes one factor at a time while holding other factors constant, and multivariate, which includes Central Composite Design (CCD) and Plackett-Burman Design (PBD). These multivariate designs, particularly CCD and PBD, are widely used to investigate multiple factors simultaneously, identifying significant factors and interactions, modeling complex relationships, reducing experimental requirements, and enhancing method robustness [12].

3. Results and discussion

3.1. Design of experiment

3.1.1. Plackett-Burman design (P-B design)

A multivariate method was developed for determining pesticide residues in soil, water, and vegetable samples. Plackett-Burman (P-B) design was employed to screen the most critical factors influencing QuEChERS efficiency and recovery [12]. This design enabled the estimation of significant factors impacting efficiency and provided valuable insights into each variable with a minimal number of experimental runs. The factors and level of variable selected for P-B design are shown in Table 1.

Table 1. Levels and factors used in P-B design for QuEChERS

S/N	Factor	Level	
		Low (-)	High (+)
1	Mass of Sample (mg)	1	2
2	Sample/water ratio (mg/mL)	1	2
3	Mass of MgSO ₄ (mg)	1	6
4	Volume of acetonitrile (mL)	5	10
5	Percentage of acetic acid in acetonitrile (%)	0	2
6	Mass of NaCl (mg)	0	2
7	Centrifugation speed (rpm)	2000	4000
8	Centrifugation time (sec)	2	5
9	Mass of sodium citrate (mg)	0	2

The results of the 12 experimental runs of the Plackett-Burman (P-B) design, examining nine factors at two levels each, are visually represented in a Pareto chart (Fig. 2) and a normal plot of standardized effects (Fig. 3). These plots display horizontal bars for the screened factors, with a red vertical line indicating the significance level. Each factor's levels are denoted as + (higher level) and - (lower level) as presented in (Table 2), providing a clear illustration of the significance of each factor [13].

Table 2. Design Table (randomized) for Plackett-Burman Design

Run	Block (Blk)	A	B	C	D	E	F	G	H	J
1	1	-	+	+	-	+	-	-	-	+
2	1	+	-	-	-	+	+	+	-	+
3	1	-	-	-	-	-	-	-	-	-
4	1	+	+	+	-	+	+	-	+	-
5	1	+	-	+	-	-	-	+	+	+
6	1	-	-	+	+	+	-	+	+	-
7	1	-	-	-	+	+	+	-	+	+
8	1	+	+	-	+	-	-	-	+	+
9	1	-	+	-	-	-	+	+	+	-
10	1	+	-	+	+	-	+	-	-	-
11	1	+	+	-	+	+	-	+	-	-
12	1	-	+	+	+	-	+	+	-	+

NB. A=mass of sample, B= sample/water C= mass of MgSO₄, D=volume of acetonitrile, E=mass of NaCl F=% of acetic in acetonitrile, G=centrifugation speed, H=centrifugation time, J=mass of sodium citrate,

The normal plot of standardized effect (Fig. 3) shows that volume of acetonitrile (D) has the most significant effect with about 90 %, followed by mass of NaCl (E) (approx. 80%), centrifugation speed (G) and mass of MgSO₄ (C) were below average effect (30 % and 20 % respectively). volume of acetonitrile (D) has been observed to have dual effect on extraction efficiency. It enhances the transport of analytes and also causes a decrease in distribution coefficient and therefore must be carefully optimized.

3.1.2. Central composite design (CCD)

The Plackett-Burman design screening experiment identified five factors with negligible impact on extraction efficiency: volume of acetonitrile, centrifugation speed, centrifugation time, mass of sodium citrate, and mass of sodium acetate. These factors were subsequently fixed at their optimal values, determined through univariate optimization. In contrast, five significant variables - sample mass, MgSO₄ mass, volume of acetonitrile, acetic acid percentage in acetonitrile, and NaCl mass - were selected for further optimization using a Central Composite Design (CCD) and Response Surface Methodology (RSM), as presented in (Table 3). This optimization significantly enhanced the extraction and cleanup efficiencies of the QuEChERS technique [14]. RSM screening identified significant factors affecting extraction efficiency, visualized in the Pareto chart (Fig. 2 and Fig. 3). Horizontal bars represent screened factors, with the red vertical line indicating the significance threshold. It can be observed from (Fig. 2 and Fig. 3) that the mass of the sample (A), percentage of acetic acid in acetonitrile (F) and centrifuge time (H) did not significantly affect extraction efficiency. Therefore, they were fixed according to the optimal value estimated using the one-factor-at-a-time (OFAT) approach. The volume of acetonitrile (D), sample/water ratio (B), mass

of MgSO_4 (C), mass of NaCl (F) and centrifugation speed (G), which were found to significantly affect extraction efficiency, were further optimized by the second-order central composite design (CCD), utilizing response surface methodology (RSM). These factors (Table 3) increased the extraction and clean-up efficiencies of the QuEChERS technique.

Table 3. The 2-level significant factors of QuEChERS methods

S/N	Factor	Level	
		Low (-)	High (+)
1	Mass of Sample (mg)	1	2
2	Mass of MgSO_4 (mg)	1	6
3	Volume of acetonitrile (mL)	5	10
4	Percentage of acetic acid in acetonitrile (%)	0	2
5	Mass of NaCl (mg)	0	2

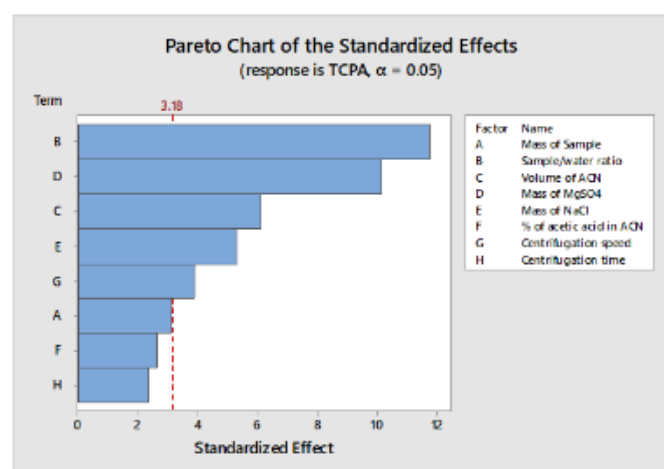


Figure 2. Pareto chart of the standardized effects

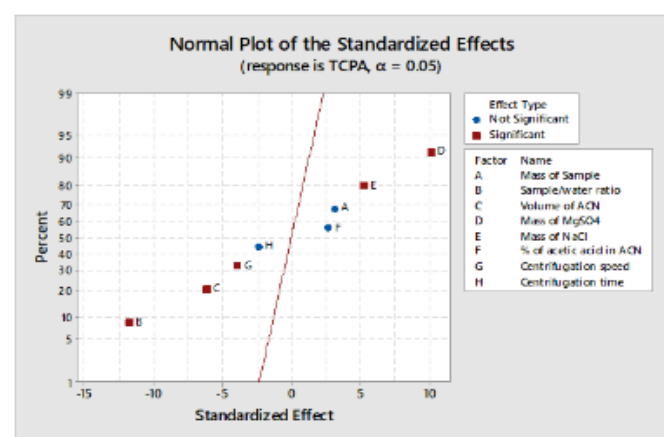


Figure 3. Normal plot of the standardized effects

3.2. Method Validation

The analytical data of the optimized Quencher method was validated for the determination of 17 target pesticides in soil sample (A) and vegetable sample (B) as presented in (Table 4). The limits of quantitation (LOQ) and detection (LOD) were determined experimentally. The LOQ was calculated using a signal-to-noise ratio of 10, while the LOD was calculated using a signal-to-noise ratio of 3. The standard deviation of the y-intercept of the

regression line of the calibration curve was used for these calculations. The calibration curve was constructed using the internal standard method. The peak area ratio of each target analyte to the internal standard was plotted against the concentration of each analyte. The resulting calibration curve exhibited the linearity ranges from 5–500 $\mu\text{g/kg}$, the correlation coefficients (R^2) were around 0.99 for all the tested pesticide residues. The LOD ranges (0.18–6.10 and 0.123–6.10) $\mu\text{g/kg}$ for soil and vegetable samples respectively, while the LOQ ranges from (0.599–20.33 and 0.40–20.313) $\mu\text{g/kg}$ for soil and vegetable samples respectively. Validation procedures were carried out to verify whether the analytical procedure used is suitable. This is essential in ensuring the optimal utilization of analytical resources [15]. The concentration levels of each pesticide residues were analyzed, and the calibration curve was constructed [15]. A set of calibration curves were prepared with concentrations ranging from 5 to 500 $\mu\text{g/kg}$ using an external standard calibration method. The calibration curve was linear over the tested concentration range (Table 4).

Table 4. Linearity ranges ($\mu\text{g/kg}$), LOD and LOQ ($\mu\text{g/kg}$) of the developed QuEChERS method

Residues	R^2	Linear range ($\mu\text{g/kg}$)	LOD ($\mu\text{g/kg}$)		LOQ ($\mu\text{g/kg}$)	
			Sample A	Sample B	Sample A	Sample B
.alpha.-Lindane	1	5–500	0.76	0.23	2.53	0.76
.beta.-Lindane	0.99	5–500	0.983	1.0	3.27	3.33
.gamma.-Lindane	1	5–500	1.12	3.12	3.73	10.38
.delta.-Lindane	0.99	5–500	1.0	1.12	3.33	3.72
Endosulfan ether	1	5–500	1.41	8.71	4.69	29.00
Heptachlor	1	5–500	0.27	3.12	0.89	10.38
Aldrin	0.99	5–500	0.28	1.45	0.93	4.82
Heptachlor epoxide	1	5–500	0.28	0.45	0.93	1.49
DDMU	1	5–500	0.46	0.68	1.53	2.26
alpha.-Endosulfan	0.99	5–500	0.18	0.38	0.59	1.26
p,p'-DDE	1	5–500	0.26	0.46	0.86	1.53
Dieldrin	0.99	5–500	0.36	0.36	1.19	1.19
Endrin	1	5–500	0.43	0.123	1.43	0.409
.beta.-Endosulfan	1	5–500	0.2	1.11	0.66	3.69
m,p'-DDD	0.99	5–500	2.14	2.10	7.13	6.993
p,p'-DDT	1	5–500	5.12	5.2	17.06	17.316
Methoxychlor	0.99	5–500	6.1	6.1	20.33	20.31

The accuracy of the developed method was evaluated by determining the relative recoveries of pesticide standards spiked into different samples (Table 5). The chromatograms of the samples, spiked at 100 $\mu\text{g/kg}$, showed no matrix effect. The relative recoveries for sample A ranged from 95.59% to 115.33%, while those for sample B ranged from 96.40% to 116.13%.

Table 5. Accuracy (relative recoveries) and precisions (relative standard deviation) of the pesticides in samples

Residues	Spiked ($\mu\text{g/kg}$)	Soil sample		Vegetable Sample	
		%Rec	%RSD	%Rec	%RSD
.alpha.-Lindane	100	97.5	1.2	96.7	0.3
.beta.-Lindane	100	98.2	1.6	99.3	1.6
.gamma.-Lindane	100	98.7	1.8	106.3	5.1
.delta.-Lindane	100	98.3	1.6	99.7	1.8
Endosulfan ether	100	99.6	2.3	125.0	14.3
Heptachlor	100	95.8	0.4	106.3	5.1
Aldrin	100	95.9	0.4	100.8	2.3
Heptachlor epoxide	100	95.9	0.4	97.4	0.7
DDMU	100	96.5	0.7	98.2	1.1
alpha.-Endosulfan	100	95.5	0.2	97.2	0.6
p,p'-DDE	100	95.8	0.4	97.5	0.7
Dieldrin	100	96.1	0.5	97.1	0.5
Endrin	100	96.4	0.7	96.4	0.2
.beta.-Endosulfan	100	95.6	0.3	99.6	1.8
m,p'-DDD	100	102.1	3.5	102.9	3.4
p,p'-DDT	100	112.0	8.4	113.3	8.5
Methoxychlor	100	115.3	10.0	116.3	10.0

RSD= relative standard deviation, %Rec = relative recoveries

These results demonstrate the high accuracy and reliability of the developed method. These are all acceptable according to the SANCO guidelines [16], which state that the method performance criteria require that mean recoveries should be within the range of 70–120% with precisions less than or equal to 20%. The average recoveries obtained in this study align with the report of [17] who obtained average recoveries ranging from 83–99%, but as a result of the fact that the design of experiments was employed to optimize factors, the optimized factors gave improved results.

3.3. Analysis of real samples

The analysis of pesticide residues in soil, water, and vegetable samples revealed varying concentrations. Fig. 4 presents the total mean concentration ($\mu\text{g/kg}$) of pesticide residues in the samples. Notably, pesticide

residues were not detected in Soil Sample 1, water samples. In contrast, Soil Sample 2 contained 17 pesticides, with concentrations ranging from 0.00–1.41 mg/L. Endosulfan ether had the highest concentration (141.0 $\mu\text{g/kg}$), followed by Methoxychlor (60.00 $\mu\text{g/kg}$), while beta-Endosulfan had the lowest concentration (<LOQ $\mu\text{g/kg}$). Aldrin and DDMU were not detected, and Heptachlor, Heptachlor epoxide, alpha-Endosulfan, p,p'-DDE, Dieldrin, and Endrin were below the calibration limit.

In vegetable samples (1 & 2), pesticide residues were detected within the range of <LOQ–870.0 $\mu\text{g/kg}$ for Sample 1 and <LOQ–110.00 $\mu\text{g/kg}$ for Sample 2. Endosulfan ether had the highest concentration (870.00 $\mu\text{g/kg}$) in vegetable sample 1, followed by delta-Lindane (110.00 $\mu\text{g/kg}$), while Heptachlor epoxide and Endrin below the LOQ. In Sample 2, delta-Lindane (110.00 $\mu\text{g/kg}$), had the highest concentration, followed by Methoxychlor and p,p'-DDT with concentration of (60.00 and 50.00 $\mu\text{g/kg}$) respectively, while Heptachlor epoxide and Endrin having the lowest concentrations (<LOQ $\mu\text{g/kg}$). Heptachlor was not detected in vegetable sample 2, and several pesticides were below the calibration limit in both vegetable samples.

3.4. Heavy metal concentration

3.4.1. Method validation

For the heavy metals considered in this study, the Limit of Quantification (LOQ) and Limit of Detection Method (LOD) were calculated using standard formulas: $\text{LOQ} = 3 \times \text{SD}$ and $\text{LOD} = 10 \times \text{SD}$. The LOQ and LOD values were specifically confirmed by sample and blank atomic absorption spectrometers. The precision and reliability of the heavy metals considered in this study are displayed in (Table 6). The relative standard deviation (RSD%) of the collected samples were analyzed.

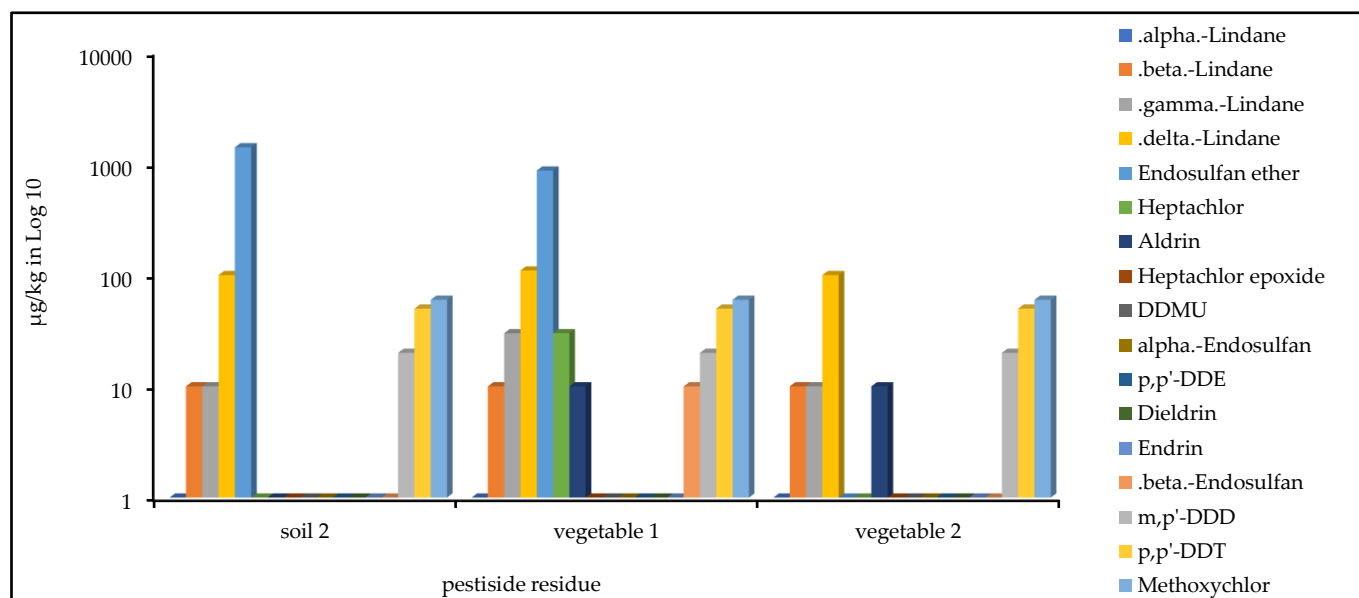
**Figure 4.** Concentration ($\mu\text{g/kg}$ in Log10) of pesticide residues in soil and vegetables

Table 6. Data specification for AAS, LOD, LOQ and % RSD for the heavy metals considered in this study.

METALS	LOD (µg/L)	LOQ (µg/L)	RSD%	R ²
As	2.1	21.2	7.1	0.9385
Cd	0.1	1.0	1.0	0.9385
Cu	10.6	106.1	3.5	0.9385
Co	6.3	63.6	2.1	0.9385
Fe	12.7	127.2	4.2	0.9385
Ni	8.4	84.8	2.8	0.9385
Pb	6.3	63.6	2.1	0.9385
Zn	8.4	84.8	2.8	0.9385

3.4.2. The concentration of heavy metal in water

Heavy metals play a critical role in eco-chemistry and eco-toxicology due to their toxicity at low concentrations and tendency to bioaccumulate in human organs. To mitigate the risks associated with heavy metal exposure, establishing dietary limits for metals in food, vegetables, and soil is essential. The Food and Agriculture Organization/World Health Organization (FAO/WHO) has established permissible limits for metals in soils, waters, and plants.

This study aimed to investigate the mean concentrations of nine heavy metals - cadmium (Cd), lead (Pb), zinc (Zn), copper (Cu), nickel (Ni), cobalt (Co), arsenic (As), and iron (Fe) - in soil, water, and plants within the study area.

Table 7 shows that all the studied heavy metals in water samples exceeded the WHO guidelines for drinking water, except for cadmium (Cd), which was below the limit. The highest concentration was recorded for iron (Fe) at 307±4.00 mg/L, followed by zinc (Zn) at 95.5±0.6 mg/L. Arsenic (As) had the lowest concentration at 3.25±0.07 mg/L.

Water systems, including rivers, streams, and lakes, are vulnerable to contamination through runoff, drainage, and disposal via sediments or wastewater [18]. Groundwater is also impacted through leaching or transport via mobile colloids. The release of heavy metals into water environments poses a significant threat to aquatic ecosystems. Due to their toxic and accumulative properties, heavy metals can alter the diversity of aquatic species and disrupt the delicate balance of ecosystems [18]. This study found elevated levels of copper (Cu) and iron (Fe) in waterholes, likely resulting from copper-containing waste discharge and anthropogenic wastewater effluents, respectively. These findings align with [19], who reported high iron levels in River Omo and Kainji Lake National Park waterholes. Lead (Pb) and nickel (Ni) levels exceeded permissible limits, potentially due to industrial waste discharges and heavy-duty vehicle exhaust [20]. Cadmium (Cd) levels surpassed guidelines, likely caused by fertilizer and sewage sludge runoff from surrounding areas [21]. Statistical analysis revealed a positive correlation

Table 7. Concentration of heavy metals in water sample

METALS (mg/L)	Mean values ± Std. deviation	WHO (2011) Guidelines for water
As	3.25±0.07	0.03
Cd	0.00±0.00	0.03
Cu	63.25±0.60	0.02
Co	22.25±0.02	0.08
Fe	307.00±4.00	0.3
Ni	10.50±0.02	0.1
Pb	58.25±0.20	0.01
Zn	95.50±0.20	5.00

between metals ($p = 0.04$, $p < 0.05$), indicating that changes in one metal's concentration are associated with changes in others.

3.4.3. The concentration of heavy metal in plant

The analysis of heavy metal concentrations in plant samples revealed that, except for iron (Fe) and nickel (Ni), all studied metals were below World Health Organization (WHO) recommended limits. Notably, iron (Fe) and nickel (Ni) exceeded guidelines at concentrations of 298±1.0 mg/kg and 7.25±0.007 mg/kg, respectively as shown in (Table 8). Iron (Fe) had the highest concentration (298±0.1 mg/kg) in plant samples, followed by zinc (Zn) at 112.75±0.2 mg/kg. The levels of iron (Fe) and zinc (Zn) in plants were significantly influenced by their respective soil content and runoff, as previously reported [21]. The presence of these metals in the study area may be attributed to human activities, including combustion of coal, residential wood combustion, iron and steel production, and power plant operations [22]. These findings suggest that anthropogenic factors contribute to heavy metal accumulation in plants, potentially impacting ecosystem health.

Moreover, Cadmium (Cd) exhibited the lowest concentration of 0.75±0.0007 mg/kg, while nickel (Ni) had a concentration of 7.25±0.007 mg/kg in the study area (Table 9). The presence of these metals in plants can be attributed to factors such as the application of fertilizers and pesticides, industrial waste disposal, and atmospheric contaminant deposition. Furthermore, statistical analysis revealed that the correlation between

Table 8. Concentration of heavy metals in plant sample

METALS (mg/kg)	Mean values ± Std. deviation	WHO recommended limits
As	6.50±0.01	0.2
Cd	0.75±0.00	0.2
Cu	56.75±0.04	10
Co	41.00±0.04	0.2
Fe	298.50±0.10	425.5
Ni	7.25±0.00	67.9
Pb	37.25±0.03	2.0
Zn	112.75±0.20	99.4

Table 9. Concentration of heavy metals in soil samples

SAMPLE	METALS (mg/kg)							
	As	Cd	Cu	Co	Fe	Ni	Pb	Zn
Soil 1	4.50±0.0014	1.50±0.001	97.0±0.002	27.0±0.004	266.25±0.9	17.25±0.004	47.25±0.003	106.5±0.002
Soil 4	30.50±0.002	52.25±0.0007	297.0±0.006	81.0±0.004	19452±14.0	27.0±0.002	106.25±0.004	360.5±0.1
Soil 5	22.0±0.002	42.0±0.004	607.0±0.001	96.25±0.002	21390.5±20.0	42.25±0.007	148.0±0.002	547.0±0.004
Soil 6	45.75±0.003	67.75±0.003	638.25±0.01	74.25±0.003	12974.25±19.0	31.25±0.002	91.75±0.003	323.0±0.004
WHO PL	20	0.8	36	0.2	50000	35	85	50

metal concentrations was not statistically significant ($p = 0.87$, $p < 0.05$), indicating a negative correlation. This suggests that an increase in one metal's concentration corresponds to a decrease in another.

3.4.4. The concentration of heavy metal in soil

The analysis of heavy metals in soil samples from areas 1, 4, 5, and 6 revealed varying concentrations. In Soil Sample 1, only iron (Fe), arsenic (As), nickel (Ni), and lead (Pb) were within the World Health Organization's (WHO) maximum allowable limits, with concentrations of 266.25±0.9, 4.50±0.0014, 17.25±0.004, and 47.25±0.003 mg/kg, respectively (Table 9). In contrast, Soil Samples 4 and 6 had only nickel (Ni) within the allowable limits, with concentrations of 27.0±0.002 and 31.25±0.002 mg/kg, respectively. Iron (Fe) had the highest concentration in both samples, with 19,452±14 mg/kg in Sample 4 and 12,974±19.0 mg/kg in Sample 6. Soil Sample 5 exceeded WHO limits for all studied heavy metals, with iron (Fe) having the highest concentration (21,390±20.0 mg/kg) and nickel (Ni) the lowest. These findings are consistent with [23], who noted that soils and sediments serve as primary repositories for metal contaminants in terrestrial and aquatic ecosystems, respectively. Heavy metals in soils pose a significant threat to human and animal health through the consumption of contaminated plants. Analysis of soil samples revealed that mean heavy metal levels exceeded maximum allowable limits. Notably, iron (Fe), copper (Cu), and zinc (Zn) concentrations suggest minimal anthropogenic influence. Zinc, an essential trace element for humans, animals, and plants, plays a crucial role in combating skin issues like acne, boils, and sore throats [24]. Copper enters soil through various means, including contamination from pipes and wires, and algal growth control measures. While copper is vital for organism development, excessive or deficient levels can be harmful [25]. As soil concentrations surpass permissible limits, the risk of heavy metal poisoning through the food chain increases [26]. This highlights the need for monitoring and mitigating heavy metal contamination in soils.

3.5. Pearson correlation analysis of heavy metals

Table 10 revealed the Pearson correlative matrix of heavy metals in all the samples. A positive correlation PC is represented by green color with ($PC \leq 1.00$). The

correlation matrix of all heavy metals (Cd, Pb, Zn, Cu, Ni, Co, As and Fe) in soil, water, and plants in the study areas as seen in Table 10, shows a strong positive correlation between (Cd, Pb, Zn, Cu, Ni, Co, As and Fe) above (>0.500) and below (<1.00). This implies that there is the possibility that heavy metals are emitted from similar sources. The result agrees with the findings of [27], who explained that common source of metals contamination input is possible across different sampling sites in the same study area.

Table 10. Correlation matrix of all studied heavy metals in the farm areas

	As	Cd	Cu	Co	Fe	Ni	Pb	Zn
As	1							
Cd	0.9810	1						
Cu	0.8477	0.8866	1					
Co	0.7685	0.8586	0.8628	1				
Fe	0.7373	0.8512	0.8147	0.9705	1			
Ni	0.6996	0.8032	0.9224	0.8980	0.9075	1		
Pb	0.6039	0.7394	0.8294	0.9131	0.9517	0.9451	1	
Zn	0.6574	0.7775	0.8664	0.9665	0.9644	0.9542	0.9808	1

4. Conclusion

In conclusion, the importance of monitoring pesticide residues in soil and plant-based foods has led to the development of various sample preparation methods. This study employed the QuEChERS-AOAC technique, a rapid and environment-friendly method, for analyzing pesticide residues in soil, water, and vegetable samples along Asa-river farmland using GC-MS. The results showed that pesticide residues were detected in soil and vegetable samples, but not in water samples, with concentrations below the maximum residue level. Notably, Soil Sample 1 and water samples had no detectable pesticide residues. However, heavy metal analysis revealed variations in metal content across samples, exceeding WHO guidelines, except for cadmium (Cd) in soil and plant samples and nickel (Ni) in Soil Samples 4 and 6. The study highlights the importance of regular monitoring of pesticide residues and heavy metals in soil, water, and vegetables to ensure food safety and prevent environmental contamination. Efforts should be made to reduce contamination in the study area, and safe pesticide usage practices should be promoted among farmers. The QuEChERS method has proven to be a fast, accurate, and efficient sample

preparation technique for pesticide residue analysis, offering a simple and effective alternative to traditional solid-phase extraction methods. Continued monitoring and mitigation efforts are necessary to protect human and environmental health.

Acknowledgements

Authors wish to acknowledge the technical support of Kwara State University, Malete. Chemistry Laboratory for the sample's analysis and individuals from samples collection locations.

Funding

No funding was provided

References

- [1] F. Lemessa, B. Simane, A. Seyoum, G. Gebresenbet, Analysis of the concentration of heavy metals in soil, vegetables and water around the bole Lemi industry park, Ethiopia, *Heliyon*, 2022, 8(12), e12429.
- [2] M. A. Hashem, M. S. Nur-A-Tomal, N. R. Mondal, M.A. Rahman, Hair burning and liming in tanneries is a source of pollution by arsenic, lead, zinc, manganese and iron, *Environ Chem Lett*, 2017, 15 (3), 501–506.
- [3] A. A. Mohammadi, A. Zarei, M. Esmailzadeh, M. Taghvi, M. Yousefi, Z. Yousefi, F. Sedighi, S. Javan, Assessment of Heavy Metal Pollution and Human Health Risks Assessment in Soils around an Industrial Zone in Neyshabur, Iran, *Biol Trace Elem Res*, 2020, 195 (1), 343–352.
- [4] D. Sharma, A. Nagpal, Y. B. Pakade, J. K. Katnoria, Analytical methods for estimation of organophosphorus pesticide residues in fruits and vegetables: A review, *Talanta*, 2010, 82(4), 1077–1089.
- [5] N. Jafarzadeh, K. Heidari, A. Meshkinian, H. Kamani, A.A. Mohammadi, G.O. Conti, Non-carcinogenic risk assessment of exposure to heavy metals in underground water resources in Saraven, Iran: spatial distribution, Montecarlo simulation, sensitive analysis, *Environ Res*, 2021, 204, 112002.
- [6] L. B. Abdulra'uf, H. B. Ibrahim, A. R. Lawal, G. H. Tan, Pesticide use: Properties and environmental fate, *Al-Hikmah Journal of Pure and Applied Sciences*, 2016, 3, 22–29.
- [7] D. J. Ecobichon, Pesticide use in developing countries, *Toxicology*, 2001, 160 (1–3), 27–33.
- [8] A. M. Junaid, M. A. Aliu, A. Ibraheem, A. Ishaq, A. Lawal, A.Y Sirhan, G. H. Tan, A.O. Mustapha, H.Y. Kazum, L. B. Abdulauf, Development of QuEChERS / HPLC technique for the determination of veterinary drug residues in beef samples, *Songklanakarin J Sci Technol*, 2023, 45(5), 599–604.
- [9] M. Anastassiades, S. J. Lehotay, D. Štajnbaher, F. J. Schenck, Fast and easy multiresidue method employing acetonitrile extraction/partitioning and “dispersive solid-phase extraction” for the determination of pesticide residues in produce, *J AOAC Int*, 2003, 86, 412–431.
- [10] Abdulra'uf, L. B., Lawal, A., Application of Multivariate Data Analysis to the Determination of Multiclass Pesticide Residues in Fruits and Vegetables using Headspace Solid-Phase Microextraction Gas Chromatography-Mass Spectrometry, *Journal of Chemical Society of Nigeria*, 2020, 45(6).
- [11] C.O. Ogah, H.B. Coker, A.A. Adepoju-Bello, Organophosphate and carbamate pesticide residues in beans from markets in Lagos, Nigeria, *Journal of Innovative Research in Engineering and Science*, 2011, 2(1), 50–61.
- [12] L. B. Abdulra'uf, A.Y. Sirhan, G. H. Tan, Applications of Experimental Design to the Optimization of Microextraction Sample Preparation Parameters for the Analysis of Pesticide Residues in Fruits and Vegetables, *J AOAC Int*, 2015, 98(5), 1171–1185.
- [13] C. Stalikas, Y. Fiamegos, V. Sakkas, T. Albanis, Developments on chemometric approaches to optimize and evaluate microextraction, *J Chromatogr A*, 2009, 1216(2), 175–189.
- [14] G. A. Curbelo, M. Asensio-Ramos, V. A. Herrera-Herrera, J. Hernandez-Borges, Pesticides residue analysis in cereal based baby foods using multi-walled carbon nanotubes dispersive solid-phase extraction, *Anal Bioanal Chem*, 2012, 404 (1), 83–96.
- [15] C. C. Chan, Principles and practices of analytical method validation; validation of analytical methods is time consuming but essential, *Quality Assurance Journal*, 2011, 14, 61–64.
- [16] Sanco. Analytical Quality Control and Method Validation Procedures for Pesticide Residues Analysis in Food and Feed; SANCO/12571/2013, Brussel, Belgium: European Commission, Directorate of General Health and Consumer Protection.
- [17] S.O. Mookantsa, S. Dube, M. M. Nindi, Development and application of a dispersive liquid-liquid microextraction method for the determination of tetracyclines in beef by liquid chromatography mass spectrometry, *Talanta*, 2016, 148, 321–328.
- [18] M. Al-Weher, Levels of heavy metal Cd, Cu and Zn in three fish species collected from the Northern Jordan Valley, *Jordan J Biol Sci*, 2008, 1, 41–46.
- [19] A. O. Omonona, F. Ajani, A.T. Adetuga, O. J. Koledoye, Heavy metals contamination in soil and water samples in Omo Forest Reserve, Nigeria, *Afr J Biomed Res*, 2019, 22, 207–214.
- [20] P.S. Rani, P.M. Reddy, Preliminary studies on metal concentration on Hussain sagar Lake, *Pollut Res*, 2003, 22, 377–380.
- [21] A. Shalini, C. K. Jain, R.S. Lokhande, Review of Heavy Metal Contamination in Soil, *Int J Environ Sci Nat Resour*, 2017, 3(5), 555625.
- [22] S. Yadav, S. S. Khirwar, Inter-relationship of soil micro-nutrient with feed stuffs in Jind district of Haryana, *Indian J Anim Sci*, 2005, 75:531–533.
- [23] M. Calkins, Materials for sustainable sites. A Complete Guide to the Evaluation, Selection, and Use of Sustainable Construction Materials, 2009, Hoboken, New Jersey, John Wiley and Sons, page 451.
- [24] D. L. Sparks, Toxic Metals in the Environment: The Role of Surfaces, Elements, 2005, 1, 193–197.
- [25] N. Jafarzadeh, K. Heidari, A. Meshkinian, H. Kamani, A.A. Mohammadi, G.O. Conti, Non-carcinogenic risk assessment of exposure to heavy metals in underground water resources in Saraven, Iran: spatial distribution, monte-carlo simulation, sensitive analysis, *Environ Res*, 2021, 204, 112002.
- [26] D.R. Baldwin, W.J. Marshall, Heavy metal poisoning and its laboratory investigation, *Ann Clin Biochem*, 1999, 36 (3), 267–300.
- [27] A.A. Adesuyi, K. I. Njoku, M.O. Akinola, Assessment of heavy metals pollution in soils and vegetation around selected industries in Lagos State, Nigeria, *Journal of Geoscience and Environment Protection*, 2015, 3, 11–19.



Characterisation of a new mesoporous active nanocarbon obtained by hazelnut shell charcoal

Hakan Akgün^{1*} , Birsen Şengül Oksal¹ , Adile Bektaş² , Hakan Bektaş¹ 

¹Giresun University, Faculty of Arts and Sciences, Department of Chemistry, 28200, Giresun, Türkiye

²Giresun Atatürk Vocational and Technical Anatolian High School, 28200, Giresun, Türkiye

Abstract

In this study, fine granulated commercial hazelnut shell charcoal was mixed together with SBA-15 consist of family of mesoporous silica nanoparticle (MSN) as a template, and then half of it carbonised again together in furnace at 900 °C in nitrogen atmosphere (FC). Other half of it is used without carbonisation (F). Obtained ordered porous carbon material (FC) and obtained other carbon material (F) from hazelnut shell charcoal were characterised by thermal gravimetry (TG/DTA), N₂ adsorption-desorption isotherm, X-ray powder diffraction, and SEM (scanning electron microscopy).

As a result, SBA-15 showed very good template properties to obtain ordered mesoporous carbon material. Surface area ordered pore diameter, and pore volume of FC were found to 9005.732 m²/g, 3220.2 nm and 1.003 cm³/g, respectively. Obtained ordered mesoporous carbon material (FC) should be suitable to use as activated nanocarbon material.

Keywords: Hazelnut shell charcoal, carbonisation, ordered porous carbon material, activated carbon, SBA-15, template

1. Introduction

Active carbon has quite a big surface area, is an excellent amorphous adsorbent. It is produced by using natural sources that contain carbon (root, stem, fruit, seed, shell of plants, etc.), burning fossil fuels (soot), and coal. In this purpose, any carbon source should be carbonised first, then activated with chemically.

Generally, the production of activated carbon is carried out in two stages: activation and carbonization. The activation process is divided into two types: physical activation and chemical activation. In physical activation, activated carbon with a lower surface area, typically used in large-scale industrial applications, is produced at a lower cost. In the chemical activation method, activated carbon with a high surface area, which finds more specific application areas, is obtained [1,2]. In recent years, ordered porous carbon materials (OPCM) have critical applications in many important fields because of their porous structure and huge specific surface area. Some specific properties of ordered porous carbon materials like low density, chemical stability, strong mechanical strength, and very good electrical conductivity provide for using them in specific and advanced technological fields. They get extensive usage

in areas especially, as an electrode in electrochemistry, hydrogen storage, heterogeneous catalysis, gas adsorption and as an adsorbent in separation processing. Ordered porous materials are classified based on pore radius (a) microporous (pore size <2 nm), mesoporous (pore size >2 nm<50 nm) and macroporous (pore size > 50 nm).

One of the important agricultural products of our country is hazelnut. After hazelnuts are harvested and cracked of the inner shell, the remaining hazelnut shells cannot be utilized for any significant purpose. Various studies have been conducted to produce activated carbon from hazelnut shells; however, even if the desired surface area is achieved, the required hardness has not been attained [3]. In Turkey, in spite of there are considerable scientific articles about producing commercial activated carbon [4,5], there is no scientific article about ordered porous activated carbon.

In 1992, researchers at the Mobil Group discovered a family of large, regularly mesoporous silica/aluminosilicate molecular sieves (M41S) and began producing them in their laboratories [6,7]. This discovery led to mesoporous materials becoming a focal

Citation: H. Akgün, B.Ş. Oksal, A. Bektaş, H. Bektaş, Characterisation of a new mesoporous active nanocarbon obtained by hazelnut shell charcoal, Turk J Anal Chem, 7(1), 2025, 55–60.

*** Author of correspondence:** hakan_akgun28@hotmail.com

Tel: +90 (454) 310 14 00

Fax: +90 (454) 310 14 77

Received: December 25, 2024

Accepted: January 24, 2025

 <https://doi.org/10.51435/turkjac.1606566>

point of interest in the scientific community[8–11]. In 1998, SBA-15 (Santa Barbara Mesopore No. 15) with pore sizes ranging from 4.6 nm to 30 nm was produced. SBA-15 mesoporous material not only possessed larger pore sizes but also demonstrated thermal, mechanical, and chemical stability, making it a preferred option for use as a catalyst. Uniformly porous, order hexagonal SBA-15 with pore sizes up to 30 nm has been synthesized using amphiphilic triblock copolymers in a strongly acidic environment [12–14].

SBA-15 was synthesized according to the literature [15], and its surface properties were elucidated. Fig. 1 shows the porous structure of SBA-15.

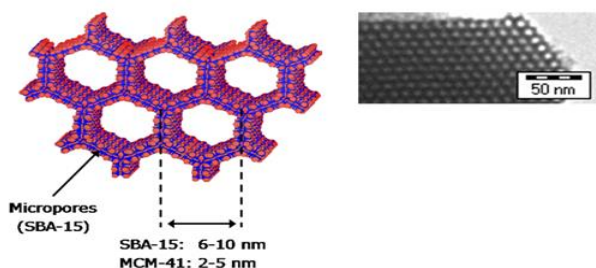


Figure 1. Representation of the pore shape and structure of MCM-41 and SBA-15 (Anonymous, 2018).

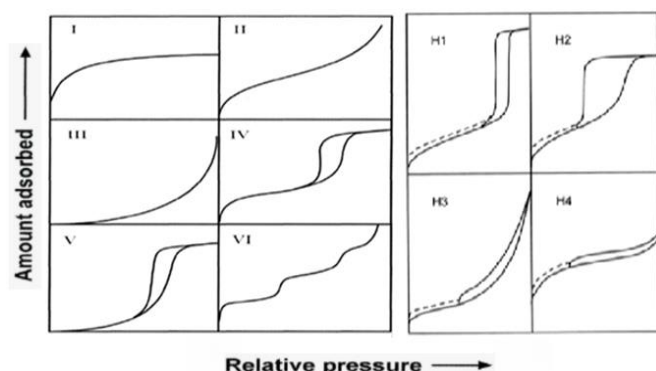


Figure 2. According to the IUPAC classification, there are six types of isotherms [16]

These six types of isotherms are shown in Fig. 2. Here, Type I corresponds to microporous, Type II, III, and VI correspond to non-porous or macroporous, and Type IV and V correspond to mesoporous materials [17].

Adsorption-desorption isotherms are also related to the pore structures of the materials. N₂ adsorption-desorption isotherm belongs to SBA-15 is given in Fig. 3. According to this isotherm, SBA-15 shows type IV isotherm curve so, it has mesoporous. Besides, porous structure of SBA-15 is relevant to type H1. Type H1 shows cylindrical or spherical porous shapes in porous materials.

In a review published by Lee and colleagues [18], they examined the scientific papers published over the past decade on the synthesis of porous carbon materials up until 2006.

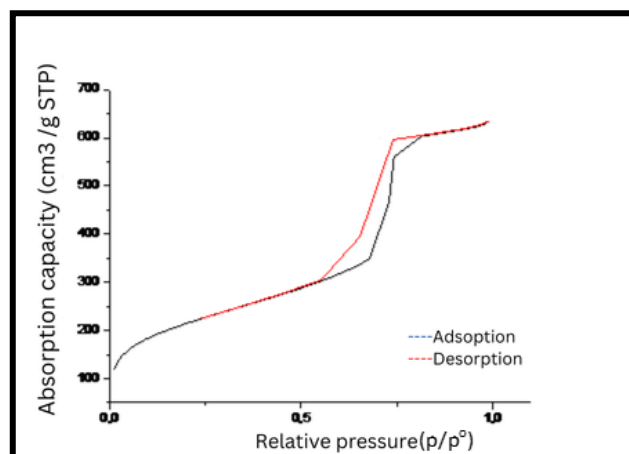


Figure 3. N₂ adsorption-desorption isotherm of SBA-15.

In this review, it is reported that, porous carbon materials have been synthesized using several different experimental methods, with various pore sizes and pore structures. For example, microporous activated carbons were synthesized via direct activation processes, while regular microporous activated carbon materials were synthesized using a zeolite template. Irregular mesoporous carbon materials have been synthesized using several different methods [15]. These include catalytic activation with various metals, carbonization of polymer/polymer mixtures, carbonization of organic aerogels, and template synthesis using silica nanoparticles. Regular mesoporous carbon materials with various pore sizes have been synthesized using mesoporous silica materials such as MCM-48, HMS, SBA-15, MCF, and MSU-X as templates. Hierarchically ordered mesoporous carbon materials have been synthesized using silica templates prepared in various pore sizes. It has been demonstrated that these mesoporous carbon materials can be successfully used as adsorbents for the adsorption of large (bulky) pollutants, as electrodes for supercapacitors and fuel cells, as hosts for enzyme immobilization, and for hydrogen storage [19].

Eftekhari and Fan (2017), reported methods for obtaining regular mesoporous carbon and their uses, particularly in various electrochemical power sources such as ultracapacitors, supercapacitors, battery systems, fuel cells, and electrochemical hydrogen storage systems in a review [20].

In this study, SBA-15 was used as a template to obtain ordered mesoporous carbon material with higher-surface area from hazelnut shell charcoal. SBA-15 forms a template that imparts its porous structure to the carbon material. So, fine granulated hazelnut shell coal was mixed with SBA-15, and then half of it was carbonised together in furnace at 900 °C in nitrogen atmosphere (FC). Other half of it is used without carbonisation (F). Obtained ordered porous carbon materials (FC and F) from hazelnut shell coal were characterised by thermal

gravimetry (TG/DTA), N₂ adsorption-desorption isotherm, X-ray powder diffraction, and SEM (scanning electron microscopy).

2. Materials and methods

2.1. Materials

The hazelnut shell charcoal was obtained from Nuts Carbon company. SBA-15 (Santa Barbara Amorphous-15) was synthesized according to the literature [15]. 48% HF (hydrofluoric acid) was obtained from Alfa-easier and used without further purification. The following instruments were used for the experiments and analyses: Precision Balance (OHAUS PA 214C, with a sensitivity of 0.0001 g), Oven (WiseVen Fuzzy Control System), Carbonization Furnace (Protherm furnace), XRD (Europe XRD 600), Nitrogen Adsorption-Desorption Device (MicroActive for TriStar II Plus Version 2.02), and TG/DTA Device (SII EXSTAR6000 TG/DTA6200). SEM images (JEOL6610).

2.2. Methods

The hazelnut shell charcoal was ground in a blender and sieved through a 35-mesh sieve. 10.00 g of the charcoal passing through the sieve was weighed and gradually added to a mixture of 5.00 g SBA-15 and 50 mL of water, which was stirred at a speed of 250 rpm. The final mixture was stirred with a magnetic stirrer under a reflux condenser in a reaction flask and boiled for approximately 12 hours. The water from this mixture was evaporated, and the residue was transferred to a shallow ceramic crucible and dried in an oven at 250 °C.

The obtained solid (carbon-silica mixture) was weighed (10.32 g) and divided into two portions. 5.00 g was weighed from the first portion of the carbon-silica mixture (CSM1). CSM1 was subjected to carbonization in a furnace under N₂ atmosphere, with temperature control (initial temperature: 20.0 °C), ramp rate: 30.0 °C/hour, and final temperature: 900.0 °C for 20 minutes. The carbonized CSM1 was weighed on a precision balance (4.8 g) and then treated with 48% HF, stirred at room temperature for 24 hours to dissolve the silica template (SBA-15). The mixture was filtered to remove all dissolved silica using a plastic funnel and blue band filter paper. The solid remaining on the filter paper was washed five times with deionized water at ambient temperature. The obtained solid carbon material was dried in an oven at 110 °C for 24 hours and then weighed (3.2 g). This solid carbon material was labeled as CF.

The second portion of the carbon-silica mixture (CSM2) was directly treated with 48% HF without undergoing carbonization, resulting in the removal of the silica template (SBA-15). This portion was labeled as

F. The physicochemical and surface properties of CF and F were compared in this paper.

SEM analyses, N₂ adsorption-desorption isotherms, XRD analysis, and TG/DTA analyses were performed on the non-carbonized (F) and 900 °C carbonized (CF) carbon materials. The synthesis of SBA-15 was carried out according to the literature [15], Structure and surface properties of FC and F were examined, and the results are presented in Table 1.

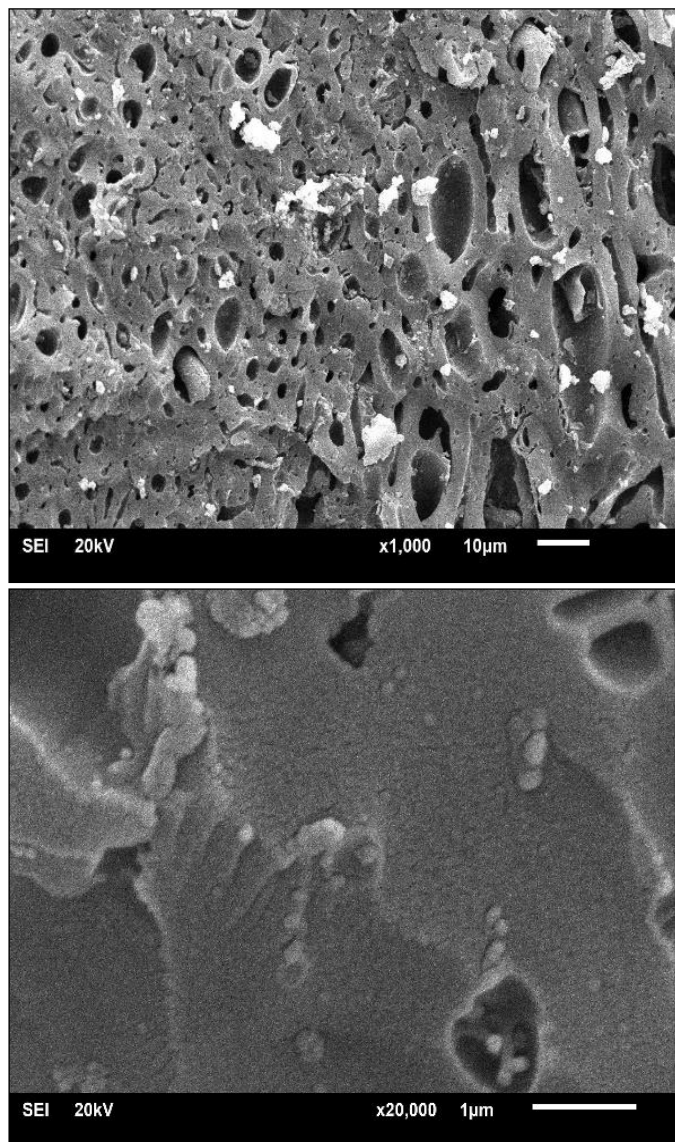


Figure 4. SEM image of FC

3. Results and discussion

The final yield of FC was calculated 96% after carbonisation at 900 °C and removal of the silica template (SBA-15) by using HF. The physical and surface properties of the obtained ordered mesoporous nanocarbon material (FC) have been elucidated. The reason for carbonisation at 900 °C was to maximize template properties of SBA-15 and to integrate well with hazelnut shell charcoal. Physical and surface properties

of FC were compared with the carbon material (F) that was obtained without carbonization.

3.1. SEM (Scanning Electron Microscope) analyses

Fig. 4 shows the SEM image of the ordered mesoporous carbon material (FC) obtained from hazelnut shell charcoal carbonized at 900 °C in the presence of the silica template (SBA-15). In the SEM image of FC, ordered micropores and mesopores are clearly visible.

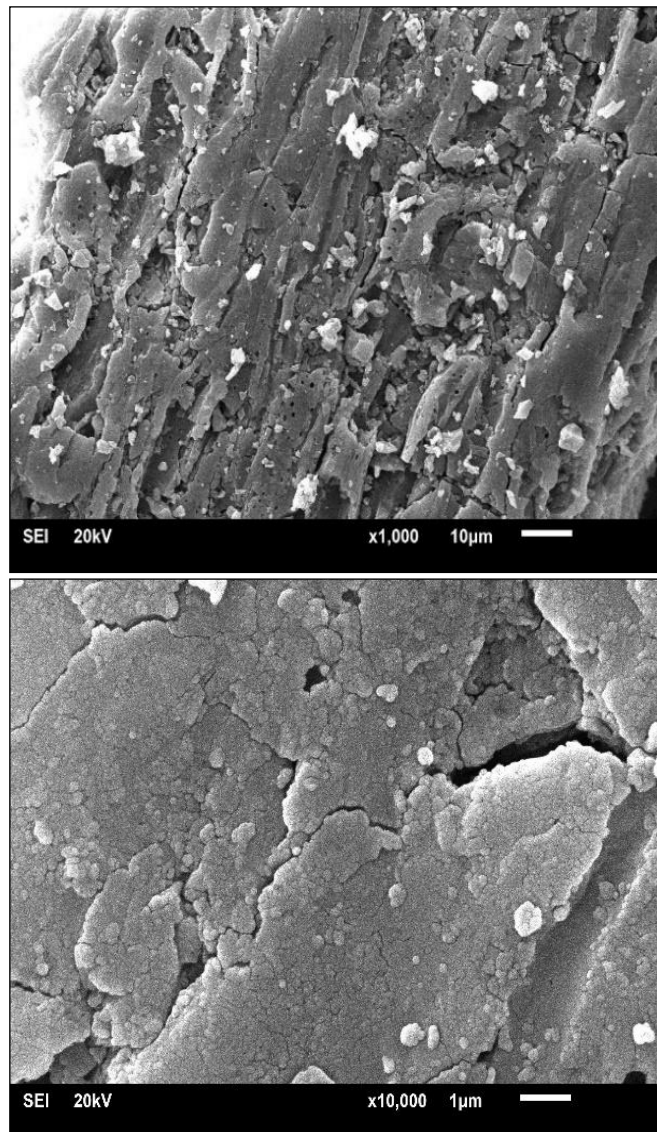


Figure 5. SEM image of F

Fig. 5 shows the SEM image of the carbon material (F) obtained from the non-carbonized hazelnut shell charcoal treated with the silica template. In these images, some porosity can be observed, although the pores are not as ordered or abundant as in FC.

In both SEM images, silica that has not been sufficiently removed from the carbon material with HF that visible as white. But at the same time, mesopore structure of FC was seen in SEM image that the most important goal of this paper was to obtain ordered mesoporous carbon material.

3.2. XRD analysis

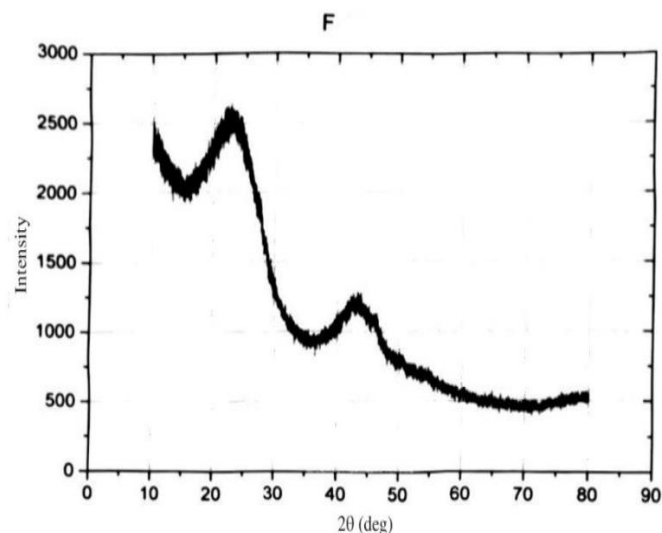


Figure 6. XRD pattern of the non-carbonized carbon material (F)

Fig. 6 shows the XRD pattern of the carbon material obtained from hazelnut shell charcoal, which was mixed with the silica template but not carbonized.

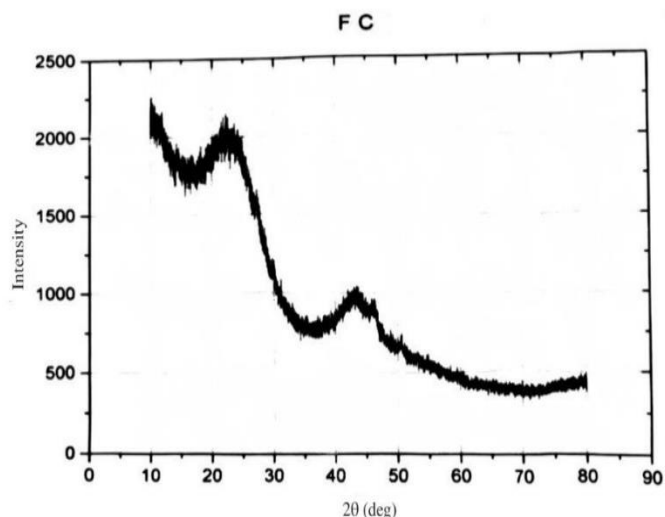


Figure 7. XRD pattern of the carbon material carbonized at 900 °C (FC)

Fig. 7 shows the XRD pattern of the ordered mesoporous carbon material (FC) obtained from hazelnut shell charcoal carbonized at 900 °C in the presence of the silica template.

The presence of broad peaks in the XRD patterns indicates that the carbon material is ordered and mesoporous. The 2θ angle shows the (002) plane at approximately 25° and the (004) plane at approximately 45°. According to the literature, these peaks are the ones corresponding to pure carbon (graphite) [19]. When comparing both XRD graphs, it can be observed that the carbon material obtained by carbonization with SBA-15 at 900 °C exhibits a lower density. This indicates that the carbon material exhibits a denser and more homogeneous porosity.

3.3. N₂ adsorption-desorption (BET) isotherms

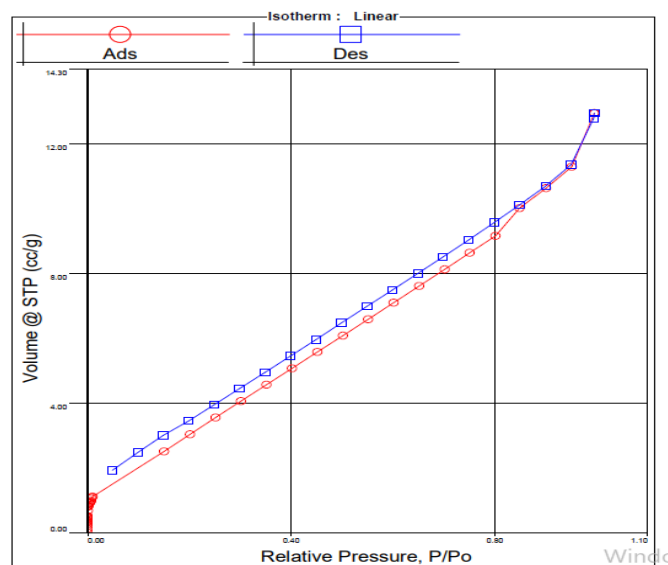


Figure 8. N₂ adsorption-desorption isotherm of the non-carbonized carbon material (F)

The N₂ adsorption-desorption isotherms of the non-carbonized carbon material (F) are shown in Fig. 8. According to these results, the surface area is 9.828 m²/g, the total pore volume is 0.02 cm³/g, the pore diameter is smaller than 2050.9 Å (P/P₀: 0.99531), and the average pore volume is 40.7404 Å. Surface area, pore volume, and pore diameter of FC and F were given in Table 1.

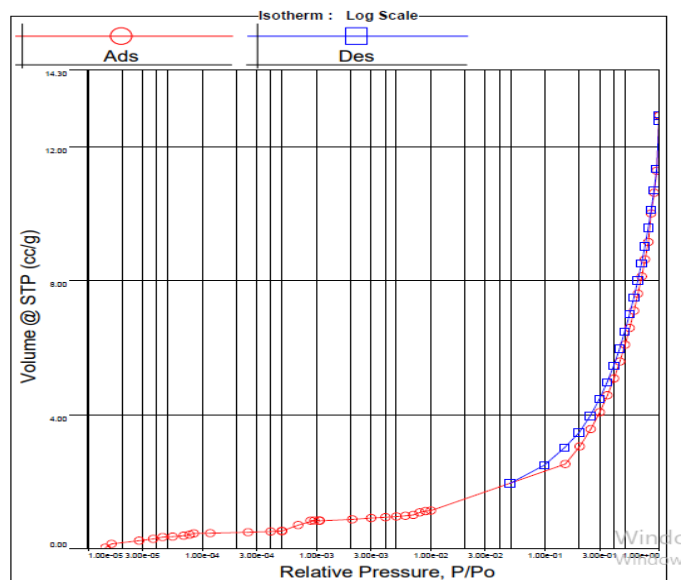


Figure 9. N₂ adsorption-desorption isotherm of the carbonized carbon material (FC).

The N₂ adsorption-desorption isotherms of the carbonized carbon material (F) are shown in Fig. 9. According to these results, the surface area is 9005.732 m²/g, the total pore volume is 1.003 cm³/g, the pore diameter is smaller than 3220.2 Å.

It was seen that the surface area of ordered mesoporus FC (9005.732 m²/g) is bigger than even commercial amorphous activated carbon (937 m²/g) [22].

Table 1: BET Analysis Results of SBA-15 [21]

Sample	Surface Area (m ² /g)	Pore Diameter (nm)	Pore Volume (cm ³ /g)
SBA-15	786,8381	5,0763	0,9614
F	9.828	2050,9	0.0200
FC	9005,732	3220,2	1,003

3.4. TG/DTA analysis

TG analysis of F and FC were performed by atmospheric pressure and rising temperature as 10 °C/min. between 30 °C–900 °C.

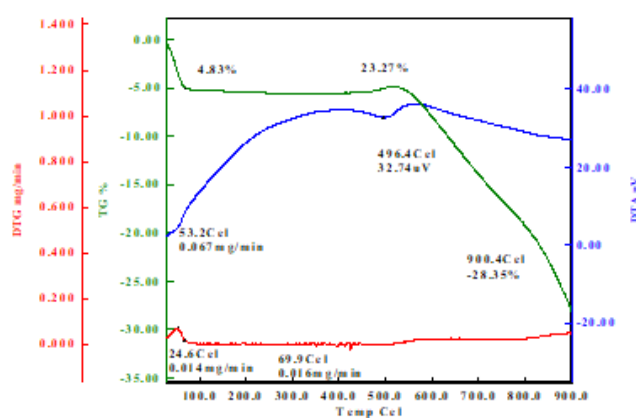


Figure 10. TG-DTA graph of FC (the carbonized carbon material at 900 °C)

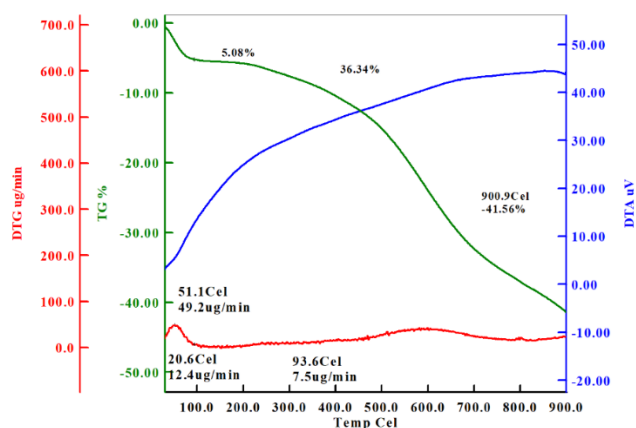


Figure 11. TG-DTA graph of F (the non-carbonized carbon material).

Upon examining the TG-DTA curves of the carbon material carbonized at 900 °C (FC) and the non-carbonized carbon material (F), it is evident that both exhibit the characteristic thermal behavior associated with porous carbon materials [23]. Total mass loss was observed as 28.35 % for FC, and 41.46 % for F, so total mass loss with increasing temperature is lower for FC than F. It can be said that, F still has some non-carbonous purities. Most probably, FC has a little silicious purities that couldn't be removed by HF treatment.

4. Conclusions

In this study, ordered mesoporous carbon material was obtained from hazelnut shell charcoal.

The ground raw hazelnut shell charcoal was treated with SBA-15 at 250 °C in an air atmosphere (F) and at 900 °C in a nitrogen atmosphere (FC), separately. Their physicochemical and surface properties were investigated. The yield of FC was found 96 % after all experimental treatment. The surface area and nature of porosity of F and FC was clarified. Structure of FC was shown very good ordered mesoporous carbon material properties.

Declaration of ethical code

The authors of this article declare that the materials and methods used in this study do not require ethics committee approval or legal special permission.

Conflicts of interest


The authors declare that they have no conflict of interest.

References

- [1] G. Newcombe, D. Dixon, Interface Science in Drinking Water Treatment (1. baskı), 2006, NSW Australia: Elsevier.
- [2] K. Sezer, Investigation of the Usability of Activated Carbon Produced from Sugar Beet Pulp for the Adsorption Of 2,4-D and Metribuzin Pesticides in Wastewaters, Yüksek Lisans Tezi, Hacettepe Üniversitesi, Fen Bilimleri Enstitüsü, 2010.
- [3] M. Yalçın, A.I. Arol, Production of Activated Carbon from Domestic Sources for Gold Metallurgy (özet), Türkiye XIII Madencilik Kongresi, 1993, Türkiye, 413-426.
- [4] E.Y. Küçükgül, Determination of Commercial Activated Carbon Production and Properties, J Eng Fac Dokuz Eylul Univ, 6, 2004, 41-56.
- [5] Z. Sayın, C. Kumaş, B. Ergül, Activated Carbon Production From Hazelnut Shells, Afyon Kocatepe Univ J Sci Eng, 16, 2016, 025805(409-419).
- [6] J.S. Beck, D.C. Calabro, S.B. McCullen, B.P. Pelrine, K.D. Schmitt, J.C. Vartuli, Method for Functionalizing Synthetic Mesoporous Crystalline Material, 2018, U.S. Patent 2.069.722.
- [7] J. Chen, N. Xia, T. Zhou, S. Tan, F. Jiang, D. Yuan, Mesoporous carbon spheres: Synthesis, characterization and supercapacitance, Int J Electrochem Sci, 4, 2009, 1063-1073.
- [8] C.T. Kresge, M.E. Leonowicz, W.J. Roth, J.C. Vartuli, J.S. Beck, Ordered mesoporous molecular sieves synthesized by a liquid-crystal template mechanism, Nature, 359, 1992, 710-712.
- [9] A. Monnier, E. Schüth, Q. Huo, D. Kumar, D. Margolese, R.S. Maxwell, G.D. Stucky, M. Krishnamurty, P. Petroff, A. Firoouzi, M. Janicke, B.F. Chmelka, Cooperative formation of inorganic-organic interfaces in the synthesis of silicate mesostructures, Science, 261, 1993, 1299-1303.
- [10] M.A. Karakassides, A. Bourlinos, D. Petridis, L. Coche-Guerente, P. Labbe, Synthesis and characterization of copper containing mesoporous silicas, J Mater Chem, 10, 2000, 403-408.
- [11] J.S. Beck, J.C. Vartuli, W.J. Roth, M.E. Leonowicz, C.T. Kresge, K.D. Schmitt, C.T.W. Chu, D.H. Olson, E.W. Sheppard, S.B. McCullen, J.B. Higgins, J.L. Schlenkert, A new family of mesoporous molecular sieves prepared with liquid crystal templates, J Am Chem Soc, 114, 1992, 10834-10843.
- [12] D.J. Zhao, Q.L. Sun, G.D. Stucky, Morphological control of highly ordered mesoporous silica SBA-15, Chem Mater, 12, 2000, 275-279.
- [13] M. Colilla, E. Balas, M. Manzano, M. Vallet-Regí, Novel method to enlarge the surface area of SBA-15, Chem Mater, 19, 2007, 3099-3101.
- [14] J. Puputti, H. Jin, J. Rosenholm, H. Jiang, M. Lindén, The use of an impure inorganic precursor for the synthesis of highly siliceous mesoporous materials under acidic conditions, Microporous Mesoporous Mater, 126, 2009, 272-275.
- [15] D. Zhao, Q. Huo, J. Feng, B.F. Chmelka, G.D. Stucky, Nonionic triblock and star diblock copolymer and oligomeric surfactant syntheses of highly ordered, hydrothermally stable, mesoporous silica structures, J Am Chem Soc, 120, 1998, 6024-6036.
- [16] K.S. Sing, Reporting physisorption data for gas/solid systems with special reference to the determination of surface area and porosity (Recommendations 1984), Pure Appl Chem, 57, 1985, 603-619.
- [17] Z.A. AlOthman, A Review: Fundamental Aspects of Silicate Mesoporous Materials, Materials, 5, 2012, 2874-2902.
- [18] J. Lee, J. Kim, T. Hyeon, Recent progress in the synthesis of porous carbon materials, Adv Mater, 18, 2006, 2073-2094.
- [19] R.K. Dash, G. Yushin, Y. Gogotsi, Synthesis, structure and porosity analysis of microporous and mesoporous carbon derived from zirconium carbide, Microporous Mesoporous Mater, 86, 2005, 50-57.
- [20] A. Eftekhari, Z. Fan, Ordered mesoporous carbon and its applications for electrochemical energy storage and conversion, Mater Chem Front, 1, 2017, 1001-1027.
- [21] Y. Şentürk, Synthesis of Mesoporous Nano Particule, Investigation of Adsorption of Glyphosate Derivative Herbicides on This Materials, Yüksek Lisans Tezi, Giresun Üniversitesi, Fen Bilimleri Enstitüsü, 2017.
- [22] Z. Hu, M.P. Srinivasan, Mesoporous high-surface area activated carbon, Microporous Mesoporous Mater, 43, 2001, 267-275.
- [23] S. Kubo, R.S. White, N. Yoshizawa, M. Antonietti, M-M. Titirici, Ordered Carbohydrate-Derived Porous Carbons, Chem Mater, 23, 2011, 4882-4885.



Theoretical and applied potential of artificial intelligence and machine learning in analysing molecular data

Fatih Mehmet Avcu 

Inonu University, Department of Informatics, 44280, Malatya, Turkey

Abstract

This manuscript serves as a comprehensive review paper examining the theoretical potential and practical applications of artificial intelligence (AI) and machine learning (ML) in molecular analysis. The purpose of this study is to synthesize existing knowledge, highlight advancements in AI/ML algorithms for molecular structure prediction, and identify future directions in the field. The significance of this review lies in its focus on bridging molecular data with AI/ML methodologies, aiming to accelerate chemical and biological research processes with enhanced accuracy. This article examines how AI and ML techniques allow accelerating and improving the accuracy of chemical and biological processes. In particular, these methods are used to predict the chemical structure, biological activity, and protein structure of molecules. Various data types such as molecular dynamics simulations, spectroscopy, and cheminformatics data are discussed in relation to AI and ML algorithms. Additionally, the revolutionary contributions of deep learning algorithms in areas such as molecular representations, drug design, and protein structure prediction are highlighted. The effectiveness of reinforcement learning and graph-based models in the prediction and optimization of chemical reactions is also discussed. In conclusion, the use of AI and ML in molecular analyses is expected to expand into broader areas of scientific and industrial research in the future.

Keywords: Artificial intelligence, molecular analysis, machine learning, molecular analysis, deep learning, chemical reactions

1. Introduction

1.1. Definition of artificial intelligence and machine learning

Definition of Artificial Intelligence and Machine Learning Artificial intelligence (AI) and machine learning (ML) have become the focus of scientific research in recent years and have brought about significant changes in complex and data-intensive processes such as molecular analysis. AI is defined as the imitation of complex tasks based on human intelligence by computer systems, while machine learning refers to the ability of these systems to improve themselves by learning from data [1]. ML, as a sub-branch of AI, enables computers to learn patterns and relationships from data sets, thus enabling them to continuously improve their performance on specific tasks. In particular, supervised and unsupervised learning methods are widely used in molecular analysis [2].

1.2. The power of machine learning algorithms

One of the advantages of ML algorithms is the ability to work effectively on large data sets. While traditional data analysis methods are usually successful with limited sample sizes, ML algorithms go beyond these limitations and can process huge data pools [3]. Especially in molecular analysis, this means that algorithms can analyze the chemical and physical properties of thousands or even millions of molecules. In addition, these algorithms play an active role in predicting the potential behavior and reactions of molecules [4].

However, ML algorithms continuously improve the learning processes of artificial intelligence systems. For example, deep learning techniques provide more accurate results by better understanding structural details in molecular image analysis [5]. This allows molecular analysis to be more predictable, fast and efficient.

Citation: F.M. Avcu, Theoretical and applied potential of artificial intelligence and machine learning in analysing molecular data, Turk J Anal Chem, 7(1), 2025, 61–70.

***Author of correspondence:** fatihavcu@gmail.com

Tel: N/A

Fax: N/A

Received: December 25, 2024

Accepted: January 23, 2025

 <https://doi.org/10.51435/turkjac.1607205>

2. Historical development of artificial intelligence and machine learning

2.1. Early studies

The concepts of artificial intelligence and machine learning were born in the mid-20th century at the intersection of mathematics, computer science, and neurology. First, Alan Turing's "Turing Test" and John von Neumann's theories of automatic computation introduced the idea that computers could exhibit human-like intelligence [6]. Simple algorithms developed in the 1950s and 1960s worked with limited data sets to perform specific tasks. Artificial intelligence studies at the time focused more on symbolic logic and rule-based systems [1].

Machine learning began to take shape in the late 1950s. Arthur Samuel first used the term "machine learning" in 1959 while working at IBM to explain that computers could learn from experience and improve [7]. Samuel's checkers-playing program embodied the basic principles of ML in that it learned from its own mistakes and improved its performance over time. This is considered the first example of the ability to "learn" which is the basis of today's machine learning algorithms [8].

2.2. Current practices

Today's artificial intelligence and machine learning technologies are quite different from the rule-based systems of the early days. In particular, new generation techniques such as deep learning and artificial neural networks have made great strides thanks to their capacity to handle large data sets. After the 2010s, deep learning has achieved significant success in areas such as image and voice recognition. In 2012, a deep learning model called AlexNet revolutionized the field by achieving great success in image recognition in the ImageNet competition [9].

Machine learning algorithms have become widely used, especially in bioinformatics and molecular analysis. Methods such as artificial neural networks, support vector machines, and random forest algorithms have made great advances in areas such as the prediction of properties of chemical compounds, protein structure prediction, and drug discovery [10,11]. At the beginning of the 21st century, the increase in computing power and the availability of large datasets enabled the rapid development of artificial intelligence and machine learning technologies [12].

3. Data types used in molecular analysis

3.1. Spectroscopy data

Spectroscopy is one of the most widely used techniques in molecular analysis, and spectral data is used to analyze the physical and chemical properties of molecules. These data contain important information to understand the molecule's energy, electron distribution, and bond structures [13]. Traditionally, analyzing this data can be time-consuming and error-prone. However, when artificial intelligence and machine learning algorithms have been used to process this data, the results have become much faster and more accurate [14].

For example, Raman spectroscopy data can be analyzed with machine learning algorithms and used for molecular structure prediction. Such algorithms save both time and cost by extracting meaningful patterns from complex data [15]. In addition, the capacity of ML algorithms to detect anomalies while analyzing spectral data is an important factor that increases the accuracy of molecular analysis.

3.2. Molecular dynamics data

Molecular dynamics is another important field that studies the motion of molecules over time. The data obtained in this field are of large size and complexity. Molecular dynamics simulations are often used to analyze the interactions of thousands of molecules, and these analyses are computationally intensive [16]. Machine learning algorithms stand out as an excellent tool for analyzing these complex data structures [17].

In particular, deep learning methods have been effective in processing molecular dynamics data and have provided important insights into new molecular structures and dynamic behaviors [18]. By processing this data, ML allows the prediction of molecular behaviors and the prediction of the properties of new molecules.

3.3. Cheminformatics data

Cheminformatics involves the use of computer technologies to store, process, and analyze chemical information for molecular analysis [19]. The data types in this field are usually based on the structural properties of molecules. Data representations such as ECFP (Extended-Connectivity FingerPrint) and Morgan FingerPrint are used to describe different structural features of molecules. These data representations are analyzed by artificial intelligence and machine learning algorithms and used in areas such as classification of molecular structures, drug discovery, and toxicity prediction [20].

ML algorithms are also used to identify similarities and differences between molecules in cheminformatics data. This is particularly important for identifying new drug candidates and predicting chemical reactions. By working with large cheminformatics datasets, AI systems can predict the behavior of new molecules and accelerate drug discovery processes [21].

4. Use of artificial intelligence and machine learning algorithms in molecular analysis

4.1. Support Vector Machines (SVM)

Support Vector Machines (SVM) is a powerful machine learning algorithm widely used for classification and regression tasks. In molecular analysis, SVM algorithms have been used with particular success in tasks such as classifying molecular structures and predicting molecular properties. Briefly, the algorithm draws a line to separate points on the training data placed on a plane, and this line is planned to be the maximum distance for the points of the two classes to be separated (Fig. 1). SVM works by creating a hyperplane to separate the data into two classes and can model complex relationships between molecules. It is a method frequently used in molecular biology, especially in areas such as prediction of protein-protein interactions and classification of drug candidates [22].

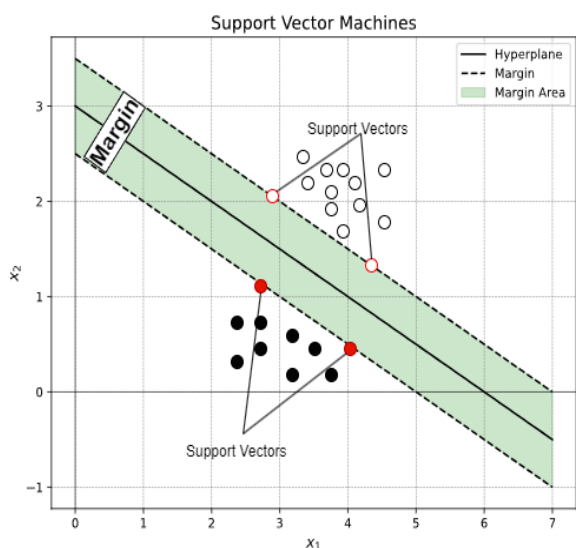


Figure 1. Support Vector Machine Algorithm

One of the biggest advantages of SVM in molecular analysis is that it can work effectively even with small data sets. While molecular analyses usually involve large datasets, in some rare cases there may be a limited number of data samples. In such cases, SVM minimizes the risk of overfitting and produces more accurate results [23]. Especially in drug discovery studies with small data sets, SVM stands out as an effective classification method [24].

4.2. Decision trees and random forests

Decision trees are an algorithm that extracts decision rules by partitioning data sets and thus performing classification or regression (Fig. 2). It is used in molecular analysis, especially in areas such as classification of compounds, toxicity prediction, and characterization of biomolecules [1]. Decision trees make distinctions between molecules based on each feature of the data set and thus classify the results.

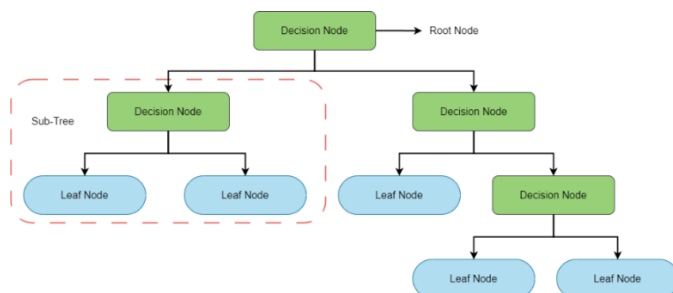


Figure 2. Decision Tree Algorithm

Random forests are a machine learning algorithm in which multiple decision trees work together to make more accurate predictions (Fig. 3). The random forest algorithm is widely used in molecular analysis, often applied in toxicity prediction, predicting the activity of new molecules and analyzing the dynamics of chemical reactions [25]. The random forest algorithm shows high performance on large datasets by analyzing a large number of molecules simultaneously. Since the data density in molecular analysis is quite high, the random forest algorithm stands out as an important tool that can work effectively with big data [26].

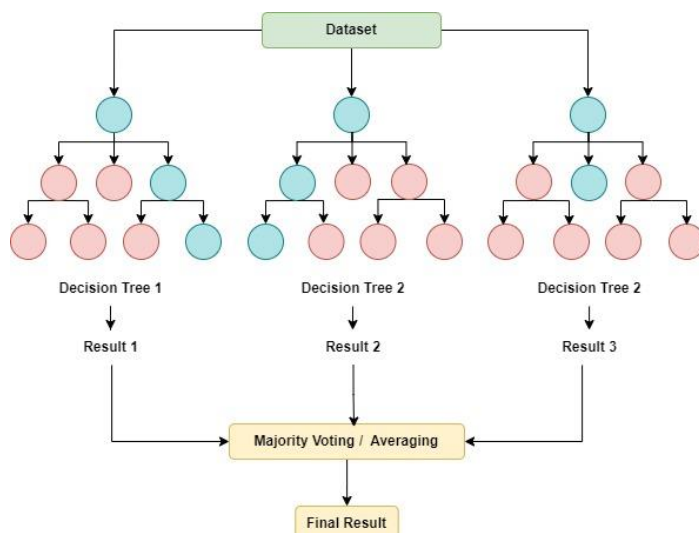


Figure 3. Random Forest Algorithm

4.3. Artificial neural networks (ANN)

Artificial neural networks are an algorithm based on data learning and classification that mimics the working principles of nerve cells in the human brain (Fig. 4). Artificial neural networks, which form the basis of deep learning methods, have become a powerful tool in

molecular analysis. In particular, multilayer perceptrons (MLP) and deep learning methods are used for modeling molecular structures and predicting complex relationships [5].

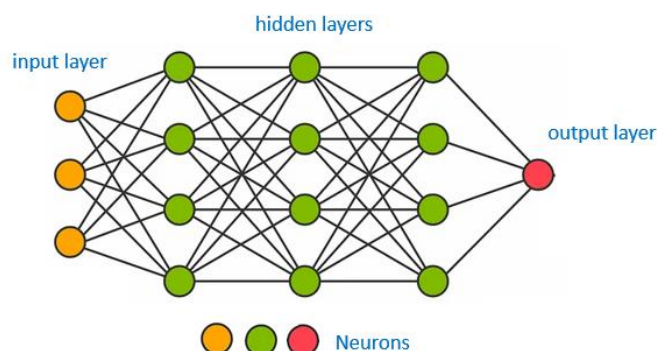


Figure 4. Artificial Neural Networks (ANN)

MLP and deep neural networks can learn patterns in molecular data through a large number of hidden layers. Therefore, they are effectively used to analyze chemical structures, protein interactions, and relationships between biomolecules. For example, neural networks are highly successful in modeling chemical reaction dynamics, drug discovery and predicting the behavior of biomolecules [27]. Moreover, the performance of deep neural networks in analyzing complex structures makes these algorithms indispensable for the future of molecular analysis [28].

4.4. Deep learning and convolutional neural networks (CNN)

Deep learning has achieved great success, especially in analyzing large data sets. Convolutional Neural Networks (CNN) are particularly effective deep learning algorithm for processing image data and are also used in molecular analysis (Fig. 5). CNN gives successful results in visualization of molecular structures, modeling of protein structures, and biomolecular image analysis [29].

CNN algorithms are widely used for 3D structure recognition and image analysis of biomolecules. In particular, CNN plays an important role in analyzing the

folding process of proteins, molecular dynamics simulations, and studying the interactions of drug molecules with biomolecules [30]. Effective processing and analysis of such big data in molecular analysis has become possible with deep learning algorithms.

4.5. Reinforcement learning

Reinforcement learning is a machine learning methodology based on interactions between an agent (computer program) and its environment (Fig. 6). It is used in molecular analysis, especially in areas such as optimization of chemical reactions and design of new molecules [31]. Reinforcement learning algorithms can make better predictions about molecular structures and chemical reactions by working on a reward and punishment system. It is an effective method for finding optimal solutions, especially in chemistry and biomolecular processes.

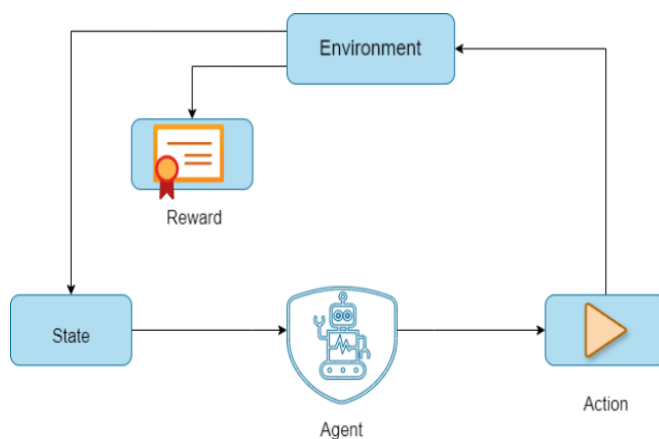


Figure 6. Reinforcement Learning

For example, during the discovery of new drug molecules, reinforcement learning algorithms can help identify the most efficient chemical structures by optimizing molecular interactions. They can also be used in molecular dynamics simulations to find the most efficient paths of molecules during a given reaction [32]. The flexible nature and learning capabilities of these algorithms can be widely applied in different areas of molecular analysis.

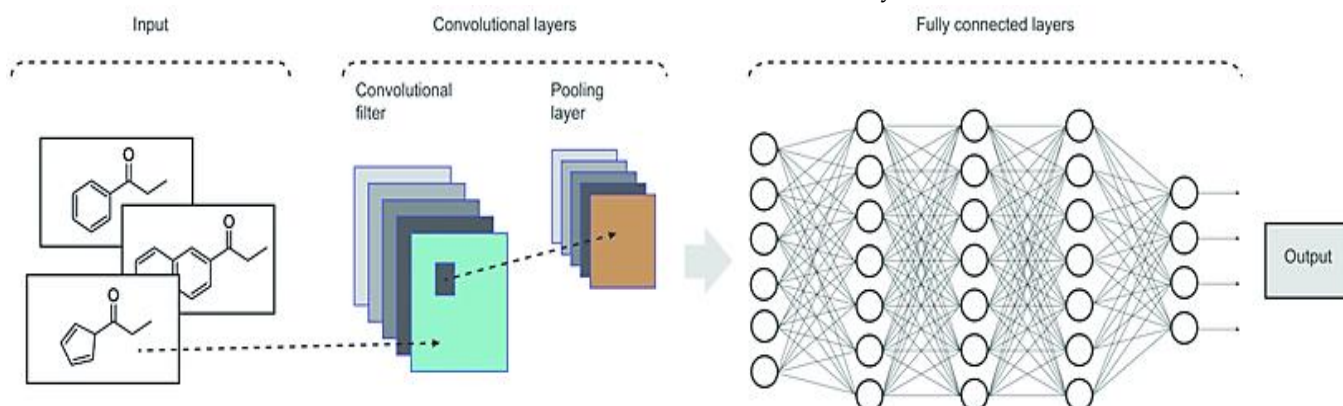


Figure 5. Convolutional Neural Networks

5. The role of artificial intelligence and machine learning in predicting molecular structures

5.1. Chemical structure prediction

Artificial intelligence and machine learning have an increasing importance in the prediction of chemical structures. In particular, the determination of molecular structures and the association of these structures with certain properties can be done more precisely and quickly thanks to artificial intelligence algorithms. For example, the high cost of calculations using quantum chemistry methods can be greatly reduced by artificial intelligence and machine learning algorithms.

In particular, graph-based machine learning algorithms are widely used to predict structural properties of molecules using graph representations of chemical compounds. By analyzing molecular graph representations by artificial intelligence models, the structure and properties of new molecules can be predicted. This offers great potential in areas such as drug discovery and materials science [33].

5.2. Protein structure prediction

Protein structure prediction is one of the common uses of artificial intelligence and machine learning algorithms in biomolecular research. Especially the folding processes of proteins and the prediction of 3D structures pose great challenges in this field. However, deep learning-based AI algorithms such as AlphaFold have revolutionized protein structure prediction [30]. AlphaFold has contributed to the advancement of biomolecular research by predicting the 3D structures of proteins with high accuracy.

Protein structure prediction plays a critical role, especially in drug discovery and understanding biological processes. By analyzing protein-protein interactions, artificial intelligence algorithms allow the discovery of new biomolecules and a better understanding of biological processes [30].

6. Applications of artificial intelligence and machine learning in molecular dynamics simulations

Accurate prediction and optimization of molecular properties is critical in drug discovery, materials science, and biomolecular processes. Artificial intelligence (AI) and machine learning (ML) techniques are used to predict the chemical and biological properties of molecules, providing effective results in these processes. Especially in the fields of molecular dynamics, quantum chemistry, and molecular design, AI and ML offer

significant advantages in terms of speed and accuracy compared to conventional methods [17,33].

6.1. Molecular activity prediction

Prediction of molecular activity plays a major role, especially in drug discovery processes. Prediction of the effects of molecules in biological systems can be time-consuming and costly with traditional experimental methods. To overcome these challenges, AI and ML algorithms have been used to predict molecular properties and biological activities [27].

One of the common methods used in molecular activity prediction is to determine the electronic structures of the molecule by quantum mechanics-based calculations and analyze how these structures can be related to biological activity. Artificial neural networks and support vector machines (SVM) are powerful tools for understanding the complex relationships between molecular properties and biological activities [34]. For example, QSPR (Quantitative Structure-Activity Relationship) models are widely used to determine the relationships of molecular structures with biological activities [35].

6.2. Molecule design and optimization

The design and optimization of new molecules is of vital importance in fields such as drug discovery and materials science. ML algorithms enable the analysis of chemical properties and the generation of optimized chemical structures that can be used in the design of new molecules. Reinforcement learning and genetic algorithms are some of the most popular methods used in this field [32].

Reinforcement learning is used to optimize the properties of molecules and design more effective structures using a reward and punishment system. This method can be effective in predicting the effects of new molecules on biological systems. Reinforcement learning algorithms are frequently used to create new chemical structures and ensure that these structures exhibit specific biological activities [36].

Especially in molecule design processes, artificial intelligence and machine learning algorithms provide a better understanding and optimization of chemical and biological processes. Deep learning algorithms make important contributions to the discovery of new biomolecules by analyzing molecular structures [37].

6.3. Quantum chemistry and artificial intelligence

Quantum chemistry is a fundamental tool used to determine the electronic properties of molecular structures and to understand chemical reactions. However, since such calculations often require high computational power, AI and ML algorithms are used to

speed up quantum chemistry calculations and analyze larger datasets [17].

In particular, deep learning methods are an effective tool for optimizing quantum chemistry calculations of molecular structures. Deep learning algorithms can be used to predict molecular energy levels, orbital structures, and other electronic properties. Such algorithms reduce computational costs in quantum chemistry, allowing for faster and more precise predictions [18].

6.4. Molecular dynamics simulations

Molecular dynamics simulations are a technique used to understand the motions and interactions of biomolecules. These simulations play a major role in analyzing biomolecular processes. However, such simulations are often very time-consuming and require high computational power. AI and ML algorithms have been used to accelerate molecular dynamics simulations and analyze more complex biomolecular systems [38].

AI-based methods reduce simulation times by predicting the motion of biomolecules. Deep learning algorithms can predict the evolution of molecular structures over time by learning the dynamics of biomolecular processes [39]. Especially the simulation of protein-protein interactions and drug-protein interactions can be done faster and more precisely with such algorithms.

6.5. Optimization of chemical reactions

Optimization of chemical reactions is an important challenge in chemistry and materials science. Artificial intelligence and machine learning algorithms are used to make chemical reactions more efficient and optimize them. For example, ML algorithms can be used to predict the probability and conditions under which a given reaction will occur. Such algorithms optimize reaction rates, making chemical processes more efficient [40].

ML algorithms are used to discover and optimize new pathways, especially in chemical synthesis. In the analysis of chemical reactions, deep learning methods allow a better understanding of reaction mechanisms and can be used to discover new reaction pathways [41].

7. The role of artificial intelligence and machine learning in predicting chemical reactions

Accurate prediction of chemical reactions is of great importance in the fields of chemistry and biochemistry. AI and ML are increasingly being used in these prediction processes, offering new ways to better

understand the kinetics, thermodynamics, and mechanisms of reactions.

7.1. Chemical reaction kinetics and thermodynamics

Chemical reaction kinetics studies the rate of a reaction and what factors influence this rate. While traditional methods need experimental data to predict reaction rates, artificial intelligence and machine learning can predict these processes without the need for experimental data. For example, deep learning models are used to predict rate constants and energy barriers of chemical reactions [40]. This greatly accelerates experimental processes and provides a great advantage for the discovery of new chemical reactions.

Thermodynamic properties of chemical reactions can also be predicted with machine learning algorithms. Free energy calculations and thermodynamic equilibria can be calculated faster and more accurately with ML models [42]. Thermodynamic equilibrium determines which products chemical reactions lead to and how stable these products are. Such calculations can be much less costly and time efficient than traditional methods.

7.2. Analysis of mechanisms of chemical reactions

The mechanisms of chemical reactions are processes that explain how bonds between molecules are broken and how new bonds are formed. Accurate modeling of these mechanisms is of great importance, especially in areas such as drug design and the discovery of new materials. Artificial intelligence and machine learning algorithms offer powerful tools for modeling and predicting the mechanisms of chemical reactions. Graph-based models and natural language processing (NLP) techniques can contribute to a better understanding of chemical reaction mechanisms [43].

By analyzing the steps of chemical reactions, graph-based machine learning algorithms can accurately predict which molecules will turn into which products. These algorithms have accelerated the understanding of organic reactions and the discovery of new chemical pathways. This provides a significant advantage in the discovery of new drugs and materials. At the same time, NLP techniques automatically analyze the mechanisms of chemical reactions found in the scientific literature, making the understanding of these processes faster and more efficient.

7.3. Optimization of chemical reactions

Optimization of chemical reactions involves determining the conditions necessary to make a given reaction more efficient. This includes optimizing temperature, pressure, catalyst usage, and other reaction conditions. Artificial intelligence and machine learning algorithms are becoming increasingly common in these

optimization processes. In particular, reinforcement learning algorithms are used to determine the optimal conditions for chemical reactions [44].

Reinforcement learning helps to identify the optimal conditions to increase the efficiency of a reaction using a reward-punishment mechanism. For example, it is possible to determine which catalyst performs best for a chemical reaction to occur with maximum efficiency and at what temperature the reaction proceeds fastest. These optimization processes can lead to huge economic gains by increasing efficiency, especially in areas such as industrial chemistry and pharmaceutical production.

8. Contributions of deep learning to molecular modeling

In recent years, deep learning (DL) algorithms have made great progress in the fields of artificial intelligence and machine learning and have revolutionized many scientific fields. Molecular modeling is one of these fields. Deep learning offers significant advantages in modeling, prediction, and simulation of complex molecular structures. In this chapter, the contributions of deep learning methods in molecular modeling and biomolecular processes will be discussed.

8.1. Use of deep learning in molecule representation

Accurately representing the structural properties of molecules is a critical step for the success of artificial intelligence and machine learning models. While traditional molecular representation methods deal with molecules in data formats such as simple line structures or atomic coordinates, deep learning algorithms can produce more complex and meaningful representations. In particular, graph-based deep learning methods represent the atomic and bond structure of molecules as graph nodes and edges [33].

Such graph-based representations allow for more accurate prediction of chemical reactions and biological activities of molecules. Methods such as Message Passing Neural Networks (MPNNs) can perform learning based on graph representations of molecules and model the properties of chemical structures. This is recognized as an important innovation in molecular simulations [18].

8.2. Prediction of molecular properties with deep learning

Deep learning algorithms achieve successful results in predicting the electronic and chemical properties of molecules. Especially in quantum chemistry calculations, deep learning methods can predict the energy levels, polarizations, and orbital structures of

molecules. Such predictions are faster and less costly compared to traditional computational methods[12].

For example, predicting molecular energy levels using deep neural networks (DNNs) and convolutional neural networks (CNNs) replaces quantum chemistry calculations and accelerates the simulation of chemical reactions. Such prediction models allow to more accurately model the probability of chemical reactions and their outcomes [18].

8.3. Drug design with deep learning

Drug design processes rely on accurate analysis of chemical and biological interactions. Deep learning algorithms play an important role in the design of new drug molecules and the prediction of their interactions with biological targets. Especially in de novo drug design processes, deep learning methods accelerate and optimize the discovery of new biologically active molecules [32].

The genetic algorithms used in these processes can be integrated with deep learning models to predict how new molecules will function in biological systems. In particular, generative models are used to create new molecular structures suitable for biological targets. This has ushered in a new era in the design of biomolecules [37].

8.4. Protein structure prediction and deep learning

Protein structure prediction is an important field for understanding biomolecular processes. The three-dimensional structures of proteins determine their biological activity and function. Deep learning algorithms have made great advances in the field of protein structure prediction. In particular, deep learning models such as AlphaFold have the capacity to accurately predict the three-dimensional structure of proteins [30].

AlphaFold has revolutionized the field of protein structure prediction, achieving significant success in solving the protein folding problem. This model uses deep neural networks to predict the final three-dimensional structure of proteins by analyzing protein sequences. This has ushered in a new era in protein design and understanding of biomolecular interactions [30].

8.5. Accelerating molecular dynamics with deep learning

Molecular dynamics simulations are a powerful technique used to model the evolution of biological and chemical processes over time. However, these simulations often have high computational costs. Deep learning algorithms offer effective tools to speed up these simulations [39].

In particular, deep learning methods such as convolutional neural networks and message passing neural networks can predict the dynamic motions of biomolecules and allow molecular dynamics simulations to be made more efficient. This enables faster and more accurate analysis of biomolecular processes [18]. Deep learning also plays an important role in predicting biomolecular interactions and modeling chemical reactions more accurately [39].

9. Performance comparison of algorithms

Machine learning algorithms exhibit superior performances in molecular analysis for different data types and application areas. The advantages of each algorithm, the parameters used, and their success rates are evaluated in a wide range of applications from molecular dynamics simulations to protein structure prediction.

Table 1 summarizes the effectiveness of different algorithms in various applications and provides an opportunity to compare performance. For example, SVM work effectively on small data sets, while RF can achieve high accuracy rates on large data sets and minimize the risk of overlearning. Deep learning methods, on the other hand, stand out with high success rates, especially in the analysis of complex biomolecular structures.

This benchmark aims to guide researchers in algorithm selection and facilitate the identification of the most appropriate methods for molecular analysis. Table 1 summarizes the performance of the algorithms mentioned throughout the paper, providing the reader with an application-oriented perspective.

This table compares the performance of different machine learning algorithms in molecular analysis. It contains information about the application areas of the algorithms, the parameters used, and their success rates. Researchers can use this table to select the most appropriate algorithm for their own studies.

10. Conclusion

This article addresses the theoretical potential and current applications of AI and ML in molecular analysis. The examples reviewed show that AI and ML have enabled a significant transformation in predicting the chemical structures, biological activities, and protein structures of molecules. In particular, these technologies are characterized by increased speed and accuracy in experimental processes. The success of deep learning, reinforcement learning, and graph-based models in modeling the kinetics, thermodynamics, and mechanisms of chemical reactions indicates that these areas will become even more important in the future.

In the future, the impact of AI and ML in molecular analyses will deepen even further. The integration of quantum computing and AI models will offer a significant improvement, especially in the simulation of chemical processes. This integration will allow more complex molecules and reactions to be simulated with high accuracy, opening up new areas of discovery for researchers. The proliferation of quantum artificial intelligence algorithms could have groundbreaking consequences in the fields of chemistry and biochemistry.

Furthermore, improvements in data diversity and quality will increase the accuracy and generalizability of AI and ML algorithms. Diversification of data sets used in molecular analyses and the creation of larger data pools will strengthen the performance and adaptability of models. Especially in fields such as cheminformatics and bioinformatics, the creation of large open-access data sets will increase the wide applicability of AI.

In addition, advances in the modeling of biological systems will lead to significant innovations in areas such as drug design and personalized therapy. AI and ML algorithms will enable deeper analysis of the dynamic processes of biomolecules, and accelerating these processes will create significant opportunities in biotechnology.

Ethical aspects of the application of artificial intelligence and machine learning in molecular analyses are of great importance to ensure the responsible use of these technologies. Particularly in an era where molecular and biological data are increasingly digitised and shared, care should be taken to protect data confidentiality. Algorithmic bias during data preparation or model training can lead to systematic errors that may undermine the validity of research results. Furthermore, explainability, which refers to the understandability of the decision-making processes of AI models, is a critical element to increase the transparency of these technologies and build trust. Addressing these ethical challenges is essential for the sustainable development of AI and machine learning applications and their widespread acceptance in scientific research.

In conclusion, the role of AI and machine learning in molecular analysis will expand even further in the future, enabling new discoveries in chemistry and biochemistry. Areas such as quantum artificial intelligence, improving data quality, and more in-depth modeling of biological processes will be key factors that will determine the future development of these technologies.

Table 1. Performance Comparison of Machine Learning Algorithms

Ref.	Implemented Algorithm	Parameters Used	Metric Used	Success Rate
[4]	Molecular Docking	Ligand flexibility	RMSD	85% (binding accuracy)
[5]	Deep Learning	Deep neural networks	Accuracy	91% (Different data set tests)
[7]	Reinforcement Learning	Self-play algorithm	Win Rate	90% (in Checker game)
[8]	Decision Tree, Neural Networks	Different dataset	Accuracy	82% (Overall forecast rate)
[9]	Convolutional Neural Network (CNN)	Depth, dropout, learning rate	Top-1 Accuracy	84% (ImageNet dataset)
[10]	Support Vector Machine (SVM)	Kernel type (RBF), C value	Accuracy	97% (RBF Kernel)
[11]	Random Forest	Number of trees	F1-Score	90% (Complex data classification)
[12]	Ensemble Methods	Bagging and Boosting	Precision, Recall	88% (Trend analysis)
[15]	Raman Spectroscopy	Spectrum analysis	Sensitivity, Specificity	92% (Preliminary disease detection)
[16]	Particle Mesh Ewald	Ewald sums	Energy Deviation	85% (Energy calculations)
[17]	Kernel Ridge Regression (KRR)	Atomic properties	MAE	95.3% (MAE < 1 kcal/mol)
[18]	Deep Tensor Neural Networks (DTNN)	Atomic coordinates, bond energies	RMSE	98% (Quantum-chemical insights)
[19]	Chemoinformatics	Ligand basic parameters	R2	87% (QSAR estimate)
[20]	Extended-Connectivity Fingerprints	Molecular fingerprinting algorithms	Accuracy	89% (Chemical classification)
[21]	Virtual Screening	Molecular docking	Docking Score	82% (Chemical screening)
[22]	Support Vector Machine (SVM)	Subcellular localization	Accuracy	88% (Protein localization)
[23]	Support Vector Machine (SVM)	Kernel selection	Accuracy	87% (Classification accuracy)
[24]	Support Vector Machine (SVM)	Kernel selection	Accuracy	85% (Bioinformatics analysis)
[25]	Random Forest	Number of trees, maximum depth	MAE	93% (QSAR modeling)
[26]	Ensemble Learning	Boosting	Accuracy	91% (Prediction model)
[27]	Generative Models	SMILES-based learning	Validity	88% (De novo design)
[28]	Genetic Algorithm + DNN	Population size, number of layers	Accuracy	92% (Chemical classification)
[29]	U-Net	Segmentation parameters	Dice Coefficient	95% (Biomedical imaging)
[30]	Deep Learning (AlphaFold)	Protein sequence length	GDT_TS	92% (Protein structure prediction)
[31]	Reinforcement Learning	State and action space	Reward Function	90% (Learning optimization)
[32]	Deep Reinforcement Learning	Latent space size	Docking Score	86% (Molecular design)
[33]	Message Passing Neural Networks (MPNN)	Atomic and bond properties	MAE	96% (Quantum chemistry)
[34]	Quantum Machine Learning	Electronic structure	R2	89% (Molecular activity)
[35]	Neural Networks	QSAR	Accuracy	94% (Target identification)
[36]	Deep Learning	DDR1 inhibitor detection	Accuracy	94% (Target identification)
[37]	Generative Adversarial Networks (GANs)	Latent space size, learning rate	Validity	88% (Molecular design)
[38]	Neural Networks	High-dimensional energy surfaces	RMSE	95% (Quantum potential)
[39]	Machine Learning	Molecular simulation parameters	MAE	90% (Physical chemistry model)
[40]	Deep Neural Networks	Chemical synthesis planning	Success Rate	92% (Accurate synthesis prediction)
[41]	Random Forest	Chemical reaction outputs	Accuracy	89% (Organic reaction)
[42]	Quantum-based ML	Electronic features	R2	94% (Chemical compound space)
[43]	Random Forest	Reaction parameters	F1-Score	90% (Organic synthesis model)
[44]	Virtual Screening + Experimental	OLED design optimization	Yield	90% (Organic synthesis model)

References

- [1] S. Russell, P. Norvig, *Artificial Intelligence: A Modern Approach* (4th ed.), 2021, USA, Pearson.
- [2] I. Goodfellow, Y. Bengio, A. Courville, *Deep Learning*, 2016, USA, MIT Press.
- [3] K.P. Murphy, *Machine Learning: A Probabilistic Perspective*, 2012, USA, MIT Press.
- [4] D. Ramírez, Computational methods applied to rational drug design, *Open Med Chem J*, 10, 2016, 7–20.
- [5] Y. LeCun, Y. Bengio, G. Hinton, Deep learning, *Nature*, 521(7553), 2015, 436–444.
- [6] A.M. Turing, Computing machinery and intelligence, *Mind*, 59(236), 1950, 433–460.
- [7] A.L. Samuel, Some studies in machine learning using the game of checkers, *IBM J Res Dev*, 3(3), 1959, 210–229.
- [8] T.M. Mitchell, *Machine Learning*, 1997, USA, McGraw-Hill.
- [9] A. Krizhevsky, I. Sutskever, G.E. Hinton, ImageNet classification with deep convolutional neural networks, *Adv Neural Inf Process Syst*, 25, 2012, 1097–1105.
- [10] C. Cortes, V. Vapnik, Support-vector networks, *Mach Learn*, 20(3), 1995, 273–297.
- [11] L. Breiman, Random forests, *Mach Learn*, 45(1), 2001, 5–32.
- [12] M.I. Jordan, T.M. Mitchell, Machine learning: Trends, perspectives, and prospects, *Science*, 349(6245), 2015, 255–260.
- [13] D.A. Skoog, D.M. West, F.J. Holler, S.R. Crouch, *Fundamentals of Analytical Chemistry* (9th ed.), 2013, USA, Cengage Learning.
- [14] H.A. Duran-Limon, A. Chavoya, M. Hernández-Ochoa, The role of machine learning in big data analytics: Current practices and challenges, *Development Methodologies for Big Data Analytics Systems*, Editors: M. Mora, F. Wang, J. Marx Gomez, H. Duran-Limon, 2024, USA, Springer, 15–28.
- [15] Y. Oshima, T. Haruki, K. Koizumi, S. Yonezawa, A. Taketani, M. Kadowaki, S. Saito, Practices, potential, and perspectives for detecting predisease using Raman spectroscopy, *Int J Mol Sci*, 24(15), 2023, 12170.
- [16] T. Darden, D. York, L. Pedersen, Particle mesh Ewald: An N-log(N) method for Ewald sums in large systems, *J Chem Phys*, 98(12), 1993, 10089–10092.
- [17] M. Rupp, A. Tkatchenko, K.R. Müller, O.A. von Lilienfeld, Fast and accurate modeling of molecular atomization energies with machine learning, *Phys Rev Lett*, 108(5), 2012, 058301.
- [18] K. Schütt, F. Arbabzadah, S. Chmiela, et al., Quantum-chemical insights from deep tensor neural networks, *Nat Commun*, 8, 2017, 13890.
- [19] F.K. Brown, Chemoinformatics: What is it and how does it impact drug discovery, *Annu Rep Med Chem*, 33, 1998, 375–384.
- [20] D. Rogers, M. Hahn, Extended-connectivity fingerprints, *J Chem Inf Model*, 50(5), 2010, 742–754.
- [21] G. Schneider, Virtual screening: An endless staircase?, *Nat Rev Drug Discov*, 9(4), 2010, 273–276.
- [22] S. Hua, Z. Sun, Support vector machine approach for protein subcellular localization prediction, *Bioinformatics*, 17(8), 2001, 721–728.
- [23] B. Schölkopf, A.J. Smola, *Learning with Kernels: Support Vector Machines, Regularization, Optimization, and Beyond*, 2002, USA, MIT Press.
- [24] W.S. Noble, What is a support vector machine?, *Nat Biotechnol*, 24(12), 2006, 1565–1567.
- [25] V. Svetnik, A. Liaw, C. Tong, T. Wang, Random forest: A classification and regression tool for compound classification and QSAR modeling, *J Chem Inf Comput Sci*, 43(6), 2003, 1947–1958.
- [26] T. Hastie, R. Tibshirani, J. Friedman, *The Elements of Statistical Learning: Data Mining, Inference, and Prediction* (2nd ed.), 2009, USA, Springer.
- [27] M. Cherti, B. Kégl, A.O. Kazakçi, De novo drug design using deep generative models: An empirical study, *International Conference on Learning Representations*, Toulon, France, 2017.
- [28] M. Karakaplan, F.M. Avcu, Classification of some chemical drugs by genetic algorithm and deep neural network hybrid method, *Concurr Comput Pract Exp*, 33, 2021, e6242.
- [29] O. Ronneberger, P. Fischer, T. Brox, U-Net: Convolutional networks for biomedical image segmentation, *International Conference on Medical Image Computing and Computer-Assisted Intervention*, 2015, 234–241.
- [30] A.W. Senior, R. Evans, J. Jumper, et al., Improved protein structure prediction using potentials from deep learning, *Nature*, 577(7792), 2020, 706–710.
- [31] R.S. Sutton, A.G. Barto, *Reinforcement Learning: An Introduction*, 2018, USA, MIT Press.
- [32] M. Popova, O. Isayev, A. Tropsha, Deep reinforcement learning for de novo drug design, *Sci Adv*, 4(7), 2018, eaap7885.
- [33] J. Gilmer, S.S. Schoenholz, P.F. Riley, O. Vinyals, G.E. Dahl, Neural message passing for quantum chemistry, *Proc Int Conf Mach Learn*, 34, 2017, 1263–1272.
- [34] R. Xia, S. Kais, Quantum machine learning for electronic structure calculations, *Nat Commun*, 9, 2018, 4195.
- [35] F. Ghasemi, A. Mehridehnavi, A. Pérez-Garrido, H. Pérez-Sánchez, Neural network and deep-learning algorithms used in QSAR studies: Merits and drawbacks, *Drug Discov Today*, 23(10), 2018, 1784–1790.
- [36] A. Zhavoronkov, Y.A. Ivanenkov, A. Aliper, et al., Deep learning enables rapid identification of potent DDR1 kinase inhibitors, *Nat Biotechnol*, 37, 2019, 1038–1040.
- [37] B. Sanchez-Lengeling, A. Aspuru-Guzik, Inverse molecular design using machine learning: Generative models for matter engineering, *Science*, 361(6400), 2018, 360–365.
- [38] J. Behler, M. Parrinello, Generalized neural-network representation of high-dimensional potential-energy surfaces, *Phys Rev Lett*, 98(14), 2007, 146401.
- [39] F. Noé, A. Tkatchenko, K.R. Müller, C. Clementi, Machine learning for molecular simulation, *Annu Rev Phys Chem*, 71, 2020, 361–390.
- [40] M.H. Segler, M. Preuss, M.P. Waller, Planning chemical syntheses with deep neural networks and symbolic AI, *Nature*, 555(7698), 2018, 604–610.
- [41] C.W. Coley, R. Barzilay, T.S. Jaakkola, W.H. Green, K.F. Jensen, Prediction of organic reaction outcomes using machine learning, *ACS Cent Sci*, 3(5), 2017, 434–443.
- [42] O.A. von Lilienfeld, K.R. Müller, A. Tkatchenko, Exploring chemical compound space with quantum-based machine learning, *Nat Rev Chem*, 4, 2020, 347–358.
- [43] R. Gómez-Bombarelli, J. Aguilera-Iparraguirre, T. Hirzel, et al., Design of efficient molecular organic light-emitting diodes by a high-throughput virtual screening and experimental approach, *Nat Mater*, 15, 2016, 1120–1127.
- [44] R. Gómez-Bombarelli, J. Aguilera-Iparraguirre, T. Hirzel, et al., Design of efficient molecular organic light-emitting diodes by a high-throughput virtual screening and experimental approach, *Nat Mater*, 15, 2016, 1120–1127.

